Fabrication of Silicon In-plane and Out-of-plane Microneedle Arrays for Transdermal Biological Fluid Extraction

by

Fahima Tazrin

A thesis

presented to the University of Waterloo

in fulfillment of the

thesis requirement for the degree of

Master of Applied Science

in

Electrical and Computer Engineering - Nanotechnology

Waterloo, Ontario, Canada, 2019

AUTHOR'S DECLARATION

I hereby declare that I am the sole author of this thesis. This is a true copy of the thesis, including any required final revisions, as accepted by my examiners.

I understand that my thesis may be made electronically available to the public.

Abstract

This thesis presents research in the field of microelectromechanical systems and specifically in the area of microneedle-based transdermal skin fluid extraction and drug delivery. The objective of this thesis is to highlight the potential role of microneedles in achieving painless transdermal skin biofluid extraction and drug delivery of macromolecular drugs across the skin barrier. The work represents the design and fabrication of silicon out-of-plane and in-plane microneedles and an innovative double-side Deep Reactive Ion Etching (DRIE) approach was presented for producing hollow silicon microneedle arrays for transdermal biological fluid extraction. The solid silicon out-of-plane microneedles are fabricated from a single side polished wafer whereas the hollow out-of-plane microneedles are fabricated from a double side polished wafer to a shank height of 200-300 μm with 300 μm center-to-center spacing. The single-step Bosch DRIE is performed for "in-plane" silicon microneedles to simultaneously etch the needle shaft (parallel to silicon substrate, etch through the wafer) and the narrow trenches as open capillary fluidic channels (partly etched into the wafer), taking advantage of the aspect-ratio dependent DRIE etching. Furthermore, the double-sided two stage DRIE is performed to etch the open trenches on the backside of wafer and then the needle shaft on the front side. The in-plane needles have the advantages of making long needles up to 2 mm. Moreover, the in vivo testing results are provided as well.

In this thesis, different microfabrication techniques are investigated, developed, optimized, and applied in the fabrication process. The first chapter conveys an overview of nanotechnology, nano-/microfabrication and their role in medicine. The second chapter illustrates an introduction to transdermal drug delivery and extraction. Furthermore, the fundamental background of skin structure and interstitial fluid (ISF) is introduced as well. Device fabrication tools and techniques are shown in chapter three. The fourth chapter presents a detailed literature review of microneedles in terms of its general concepts, structures, materials and integrated fluidic system. Eventually, Chapter 5 introduces the details of our method to fabricate solid and hollow silicon microneedle arrays step by step. SEM images and in vivo testing results confirm that silicon microneedle both out-of-plane and in-plane arrays are not only sharp enough to penetrate the stratum corneum but also robust enough to extract ISF out of skin or to deliver drug.

Acknowledgements

This work was carried out using the nanofabrication facility at Quantum NanoFab, WATLab and Giga-to-Nanoelectronics (G2N) Laboratory at University of Waterloo. Their support is always grateful. The work is partly supported by the NSERC and OCE TalentEdge internship fund. I am greatly acknowledged to ExVivo Labs Inc. for providing me with this precious opportunity.

First, I would like to express my warmest gratitude to my husband and to my loving parents for their continuous encouragement throughout my studies. They always encourage and support me behind the scenes so that I can dedicate myself to the research work.

Furthermore, I would like to thank my supervisor Professor Bo Cui. I am very grateful for getting his kind guidance and invaluable suggestions throughout the entire work.

I am extremely thankful to Professor Michal Bajcsy for his conscientious guidance and encouragement throughout my whole educational journey in Canada.

Finally, I would like to thank to our nanofabrication group at University of Waterloo and R&D team in ExVivo Labs Inc., especially the group mates and co-workers Dr. Y. Li, H. Zhang. Dr. R. Yang, Y. Laffitte, U. Schmill, F. Aydinoglu, Y. Liu, M. Soltani and R. Dey.

Dedicated with all my heart to my best family.

Table of Contents

List of Figures

List of Tables

List of Abbreviations

MN	microneedle
Si	silicon
DRAM	Dynamic random access memory
AFM	atomic force microscopy
SEM	scanning electron microscope
SC	Stratum corneum
ISF	interstitial fluid
DRIE	deep reactive ion etching
MEMS/NEMS	micro/nano-electromechanical system
ARDE	aspect ratio dependant etching
PR	photoresist
NW	nanowire
PDMS	polydimethylsiloxane
HMDS	hexamethyldisilazide
SM	solid microneedle
HM	hollow microneedle
R&D	research and deveopment
PMMA	polymethyl methacrylate
MNS	micro-/nano system
NS	nanostructure

KOH	potassium hydroxide
HF	hydrofluoric acid
Ar	argon
HNO_3	nitric acid
CH_3 COOH	acetic acid
TMAH	tetramethylammonium
NiFe	iron-nickel alloy
Cr	chromium
SF_6	sulfur hexafluoride
O_2	oxygen
SiF_6	silicon tetrafluoride
CHF_3	fluoroform

"I think it's much more interesting to live not knowing than to have answers which might be wrong."

— Richard P. Feynman

Chapter 1

Introduction

This chapter brings an overview of importance of nanotechnology over the years, especially nanotechnology in medicine and MEMS for biomedical applications. Furthermore, the fundamental concept of nano-/microfabrication is introduced as well.

1.1 Introduction to nanotechnology (nano-/microfabrication)

The English physicist and chemist John Dalton initially proposed the logical hypothesis of the atom two hundred years ago. From that point forward we have seen scientific experts come to comprehend the components and their associations, we have seen engineers make and utilize new materials to enhance our lives, we have seen physicists show that even atoms are separable, and we have seen warriors release the intensity of the atomic nuclear. In these two centuries we have amassed a tremendous comprehension of and used an expanding power over the fundamental units of matter.

Today, in the youthful field of nanotechnology, researchers and engineers are taking control of atoms and molecules separately, controlling them and putting them to use with an uncommon level of exactness. Expression of the guarantee of nanotechnology is spreading quickly, and the air is thick with news of nanotech achievements. Governments and organizations are putting billions of dollars in nanotechnology R&D, and political partnerships and fight lines are beginning to frame. Open attention to nanotech is plainly on the ascent, as well, somewhat in light of the fact that references to it are ending up increasingly regular in mainstream culture — with appearances in motion pictures (like The Hulk and The Tuxedo), books (counting a year ago's Michael Crichton success, Prey), computer games (for example, the "Metal

Gear Solid" arrangement), and TV (most strikingly in different manifestations of Star Trek).

"Everything, when miniaturized to the sub-100-nanometer scale, has new properties, regardless of what it is," says Chad Mirkin, professor of chemistry at Northwestern University.

Nanotechnology is the ability to individual atoms and molecules to create nanostructured materials and submicron objects that have applications in reality. Nanotechnology includes the generation and use of physical, chemical and biological frameworks at scales extending from individual atoms or molecules to around 100 nanometers, and additionally the mix of the subsequent nanostructures into bigger frameworks.

Nanofabrication is the design and manufacture of devices with dimensions measured in nanometer. A nanometer is one billionth of a meter. The prefix “nano-” comes from the Greek word nanos, meaning dwarf. (Scientists originally used the prefix just to indicate “very small,” as in “nanoplankton,” but it now means one-billionth, just as “milli-” means one-thousandth, and “micro-” means one-millionth). Figure 1.1 gives a feeling for the ‘nano world’, which is populated by atoms, molecules, and molecular machines such as the ribosome, a cellular organ producing proteins in our body.

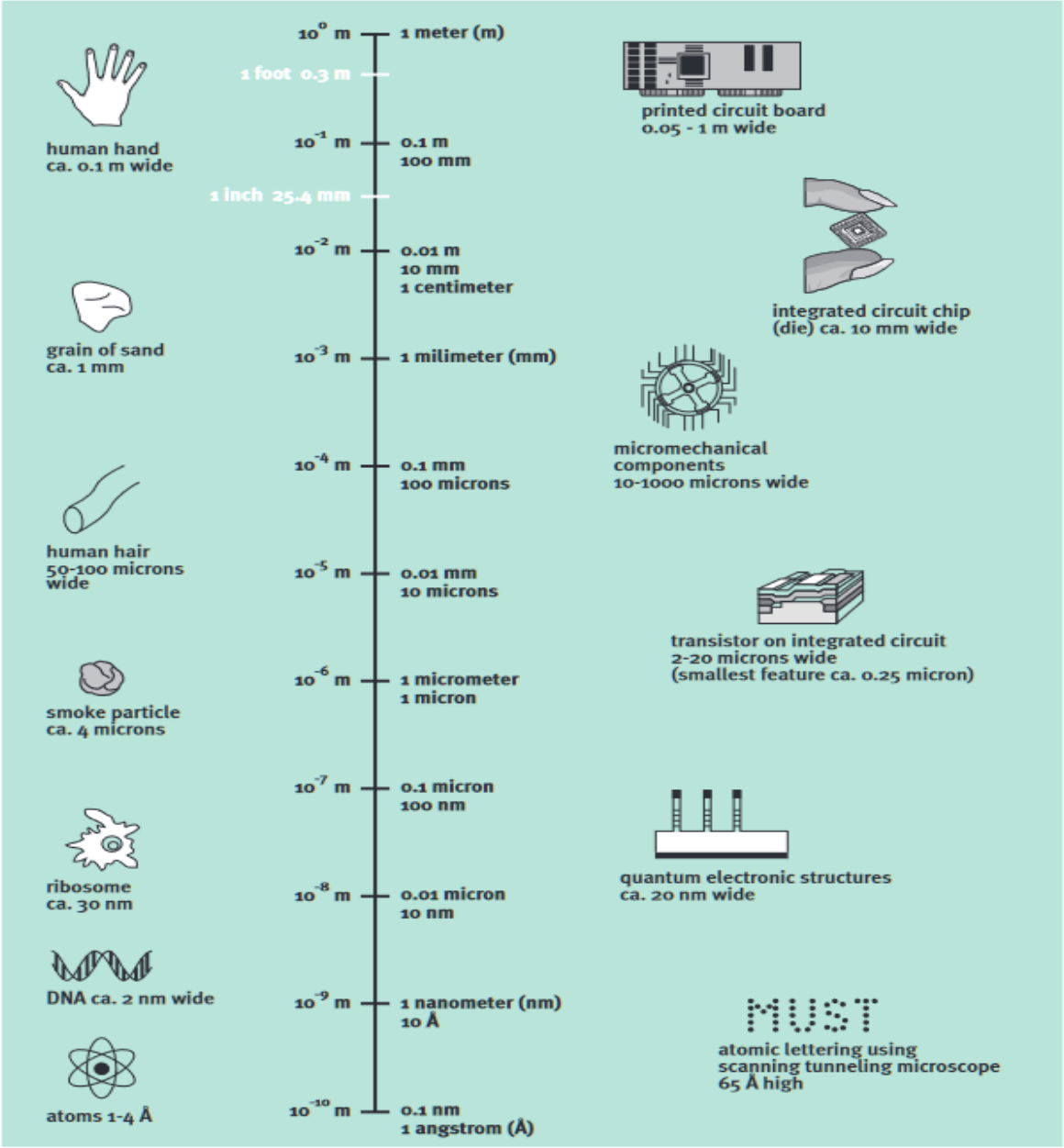

Figure 1.1 From the 'real' to the nanoworld. Figure adapted from the Office of Technology Assessment [5].

As far back as the creation of the transistor in 1947, and later the reconciliation of every electronic segment in a 'single chip', scaling down of these gadgets has been a continuous essential process. The component size of coordinated circuits has contracted by a relatively consistent rate of about 30% at regular intervals throughout the previous 15 years. This trend is known as Moore's Law (Fig 1.2). The transistor density on a manufactured integrated circuit has doubled every eighteen months,

while the storage capacity of dynamic random access memory (DRAM) chips has increased with a factor of four every three years. It enabled faster circuits, more complex designs, and more economical production processes. Spurred to continue this miniaturization trend, researchers continue to develop novel processes with improved quality [1]. It is expected that minimum dimensions of integrated circuits will continue to shrink at this rate over the coming decade. This can be seen from the current 'roadmap' [2] of the future for the semiconductor industry (table 1.1) [4].

Figure 1.2 The number of transistors on integrated circuit chips [3].

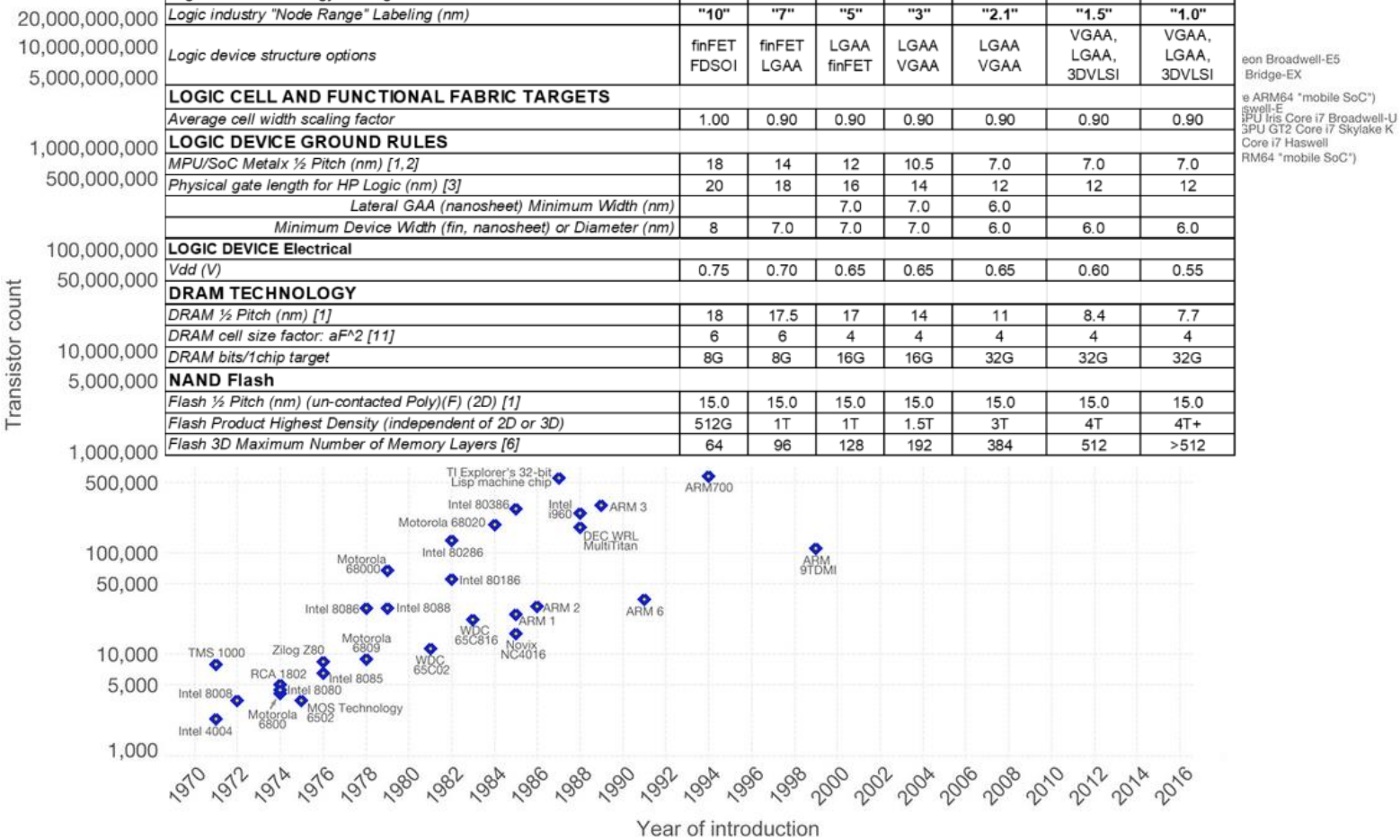

2017 IRDS Executive Summary - ORTC							
YEAR OF PRODUCTION	*2017*	*2019*	*2021*	*2024*	*2027*	*2030*	*2033*
Logic device technology naming	P54M36	P48M28	P42M24	P36M21	P32M14	P32M14 T2	P32M14 T4
Logic industry "Node Range" Labeling (nm)	"10"	"7"	"5"	"3"	"2.1"	"1.5"	"1.0"
Logic device structure options	finFET FDSOI	finFET LGAA	LGAA finFET	LGAA VGAA	LGAA VGAA	VGAA, LGAA, 3DVLSI	VGAA, LGAA, 3DVLSI
LOGIC CELL AND FUNCTIONAL FABRIC TARGETS							
Average cell width scaling factor	1.00	0.90	0.90	0.90	0.90	0.90	0.90
LOGIC DEVICE GROUND RULES							
MPU/SoC Metalx ½ Pitch (nm) [1,2]	18	14	12	10.5	7.0	7.0	7.0
Physical gate length for HP Logic (nm) [3]	20	18	16	14	12	12	12
Lateral GAA (nanosheet) Minimum Width (nm)			7.0	7.0	6.0		
Minimum Device Width (fin, nanosheet) or Diameter (nm)	8	7.0	7.0	7.0	6.0	6.0	6.0
LOGIC DEVICE Electrical							
Vdd (V)	0.75	0.70	0.65	0.65	0.65	0.60	0.55
DRAM TECHNOLOGY							
DRAM ½ Pitch (nm) [1]	18	17.5	17	14	11	8.4	7.7
DRAM cell size factor: aF^2 [11]	6	6	4	4	4	4	4
DRAM bits/1chip target	8G	8G	16G	16G	32G	32G	32G
NAND Flash							
Flash ½ Pitch (nm) (un-contacted Poly)(F) (2D) [1]	15.0	15.0	15.0	15.0	15.0	15.0	15.0
Flash Product Highest Density (independent of 2D or 3D)	512G	1T	1T	1.5T	3T	4T	4T+
Flash 3D Maximum Number of Memory Layers [6]	64	96	128	192	384	512	>512

Table 1.1 The overall roadmap technology characteristics [4].

In another reality where innovation is developing at a pace a lot higher than any purpose of time in written history, nanoengineering is pushing the limits of regular technological practices. Many nanotechnology-enabled products are already on the

market and enjoying commercial success. After the innovation of the scanning tunneling microscope (STM) in 1980 by Gerd Binnig and Heinrich Rohrer at IBM Zurich, which also earned them the Nobel prize in physics in 1986, nanotechnology picked up fast. The development of STM was a precursor to the development of atomic force microscope (AFM) which ultimately allowed scientists to see the materials at unprecedentedly small scales. We have made considerable progress since the 1980s and the time is immaculate to audit a portion of the key nanotechnology improvements in STEM fields. The different phases of improvement have been condensed in the following Table 1.2 [10].

Year	Development in nanotechnology
1959	R. Feynmaninitiatedthought process
1974	The term nanotechnology was used by Taniguchi for the first time.
1981	IBM Scanning Tunneling Microscope
1985	"Bucky Ball"
1986	First book on nanotechnology Engines of Creation published by K. Eric Drexler, Atomic Force Microscope
1989	IBM logo was made with individual atoms
1991	S. Iijima discovered Carbon Nano tube for the first time.
1999	1st nano medicine book by R. Freitas"Nano medicine" was published
2000	For the first time National Nanotechnology Initiative was launched
2001	For developing theory of nanometer-scale electronic devices and for synthesis and characterization of carbon nanotubes and nano wires, Feynman Prize in Nanotechnology was awarded
2002	Feynman Prize in Nanotechnology was awarded for using DNA to enable the self-assembly of new structures and for advancing our ability to model molecular machine systems.
2003	Feynman Prize in Nanotechnology was awarded for modeling the molecular and electronic structures of new materials and for integrating single molecule biological motors with nano-scale silicon devices.
2004	First policy conference on advanced nanotech was held. First center for nano mechanical systems was established, Feynman Prize in Nanotechnology was warded for designing stable protein structures and for constructing a novel enzyme with an altered function.
2005-2010	3D Nano systems like robotics, 3D networking and active nano products that change their state during use were prepared.
2011	Era of molecular nano technology started

Table 1.2 Different stages of development in nanotechnology [10].

In parallel, developments in the territory of microfabrication have made an extraordinary open door for assembling micron-sized structures [6]. In order to realize diverse novel applications with ultimate precision and high efficiency, various nano/microfabrication techniques are carried out in research area, which can be generally divided into two essential approaches: 'top-down' and 'bottom-up'. Top-

down approaches are good for producing structures with long-range order and for making macroscopic connections, while bottom-up approaches are best suited for assembly and establishing short-range order at nanoscale dimensions. Schematic representation of the formation of nanostructures via the top-down and bottom-up approaches (a) is shown in Fig 1.3 [7]. In top down fabrication approach (b), a tapered probe, manipulated by a macroscopic machine, allows "writing" small features by scratching the probe apex on a soft polymer surface. Notice the removed material disperses on the sides of the created grooves. In bottom-up fabrication approach (c), example of self-assembling set to occur on previously chemically functionalized surfaces; chemisorption happens due to interactions between adsorbing molecules and specific sites on the substrate. The resulting nano-electronics material emerges with much more effective functions when proper shapes and microstructures are provided [8,9].

As one of the crucial and basic systems in microfabrication, optical lithography is broadly connected and created from the fabrication of integrated circuits to microelectromechanical systems (MEMS). Lithography strategies will be presented in detail in chapter 3.

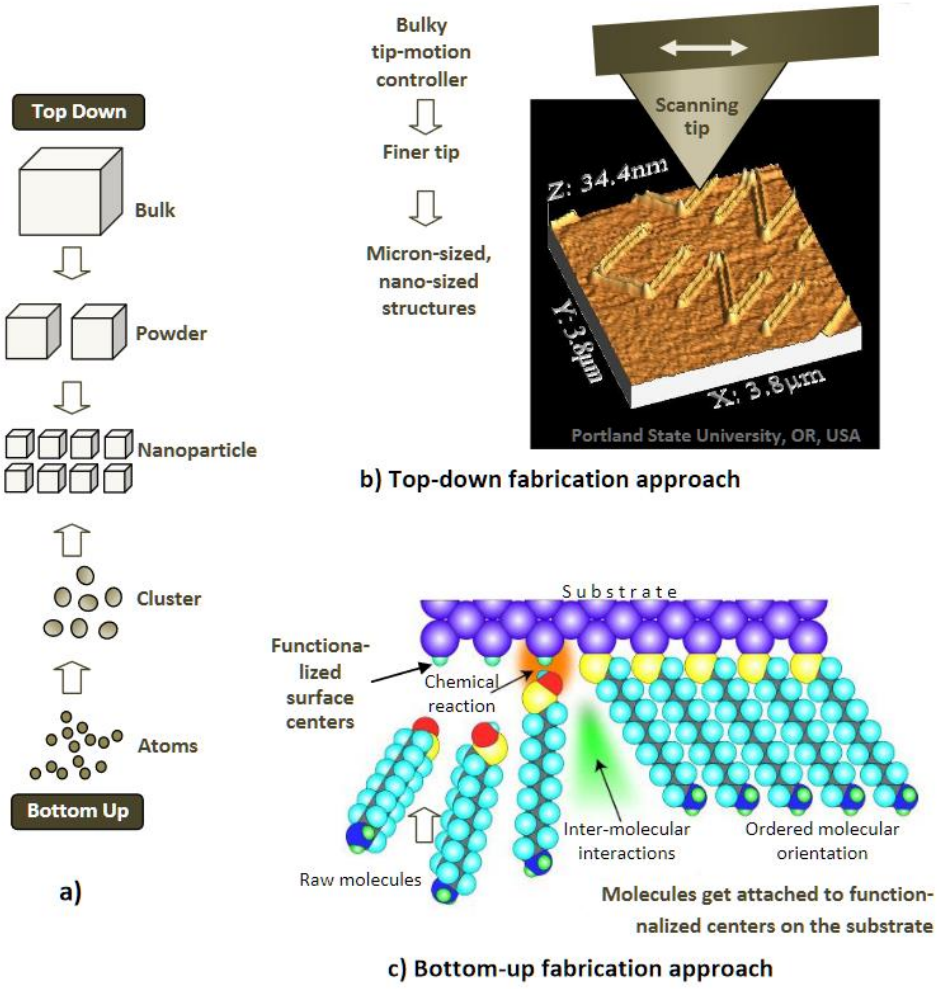

Figure 1.3 Schematic diagram of top-down and bottom-up approach. [(b) Image attained at Portland State University, Portland, Oregon, USA; courtesy of Rodolfo Fernandez. c) Image courtesy of Dr. Hiroyuki Sugimura, Nanoscopic Surface Architecture Laboratory, Department of Materials Science and Engineering Kyoto University, Japan.]

1.2 Nanotechnology in medicine

Countless applications of nanotechnologies are currently opening up. Nanotechnologies are enabling the development of smaller, cheaper sensors, which

will have a wide range of applications from monitoring the pollution in the environment, the freshness of food, or the stresses in a building or a vehicle. Uses of nanotechnologies in medicine are particularly encouraging in the more extended term. These can be expected to enable drug delivery targeted at specific sites in the body so that, for example, chemotherapy is less invasive. Nanotechnology is being used for detection, diagnostics, therapeutics and monitoring. Subjects like nanotechnology put together imaging technologies and lab-on-a-chip point of care diagnostics, advanced nano-bio-sensor technologies, implantable nano sensors, nano arrays for advanced diagnostics and therapy, invasive therapy technologies and cellular based therapy.

1.2.1 Biomedical application of MEMS

Micro-Electro-Mechanical Systems (MEMS) are a class of miniature devices and systems fabricated by micromachining processes. MEMS innovation is a forerunner to the moderately increasingly well-known field of nanotechnology, which alludes to science, designing and innovation beneath 100 nm down to the atomic scale. This miniaturization ability has enabled MEMS to be applied in many areas of biology, medicine, and biomedical engineering – a field generally referred to as BioMEMS [14]. The field of microelectromechanical system was invented initially by the microfabrication techniques for a variety of applications such as electronics, sensors, actuators [11,12,13]. Models incorporate basic sensors utilized amid medical procedure, long-term sensors for prosthetic gadgets, and exceedingly modern sensor clusters for quick lab-quality determination at home. Figure 1.4 shows analog devices

with small size (7.3 mm^3) MEMS microphone suitable for hearing-aid applications [15].

Figure 1.4 MEMS microphone [15] (Source: http://www.analog.com/).

BioMEMS also give numerous opportunities for improved drug delivery: low-dose vaccinations and painless transdermal drug delivery are possible through precisely fabricated microneedles which penetrates into the skin's barrier layer without reaching the nerves [16]. More details on microneedles will be discussed in the following chapter.

Chapter 2

Transdermal Drug Delivery and Biofluid Extraction

Transdermal drug delivery means that a medicinal compound is delivered across the skin—the dermis—for subsequent systemic distribution. Hence, strictly this does not only include the more commonly understood "patch", but also traditional subcutaneous administration (a subcutaneous injection is administered as a bolus into the subcutis, the layer of skin directly below the dermis and epidermis, collectively referred to as the cutis) by means of a hypodermic needle and a syringe. With the increasing need for non-invasive biological fluid sampling and real time physiological monitoring, interest in exploring different methods to extract dermal interstitial fluid (ISF) has grown in recent years. This chapter demonstrates an overview of transdermal drug delivery, the fundamental concept of human skin anatomy and skin interstitial fluid (ISF).

2.1 Transdermal drug delivery

Transdermal therapeutic systems are defined as self-contained, self-discrete dosage forms, which when applied to the intact skin deliver the drug at a controlled rate to the systemic circulation. A straightforward patch sticks to the skin like a glue wrap, which uses detached dispersion of medications over the skin as the conveyance component. Regular to all strategies for transdermal drug delivery, by this expansive definition, the medication goes through an artificial route into the body. The principle preferred standpoint of this methodology is that the medication goes into the body undistorted without going through the body's various defense systems. This method relies on the transport of drugs across the skin into the blood stream. The structure and properties of the skin are important factors for this method of administration.

Transdermal delivery offers to an alluring option to oral delivery of medications and is ready to give an option in contrast to hypodermic injection [21-24]. In the United

States in 1979, the first transdermal system for foundational delivery of scopolamine for three days to treat motion sickness was approved. After about 10 years, nicotine patches turned into the principal transdermal blockbuster, raising the profile of transdermal delivery in medicine. Today, there are 19 transdermal delivery systems for such medications as estradiol, fentanyl, lidocaine and testosterone; mix patches containing more than one medication for contraception and hormone substitution; and iontophoretic and ultrasonic delivery systems for the absence of pain. Somewhere between 1979 and 2002, another fix was affirmed every 2.2 years. In the course of recent years (2003– 2007), that rate has dramatically multiplied to another transdermal delivery framework every 7.5 months. It is evaluated that more than one billion transdermal patches are right now produced every year [23]. Table 2.1 shows

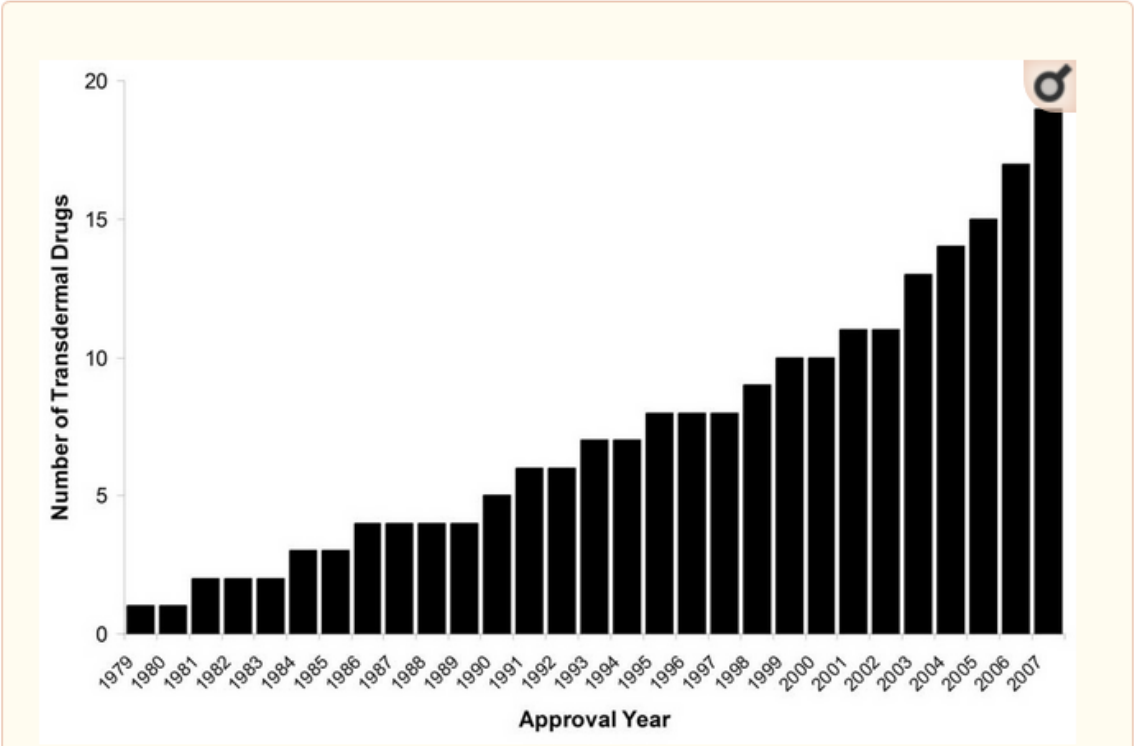

cumulative number of transdermal drugs approved by the FDA since the first approval in 1979 [25].

Table 2.1 Cumulative number of transdermal drugs approved by the FDA [25].

There are many drawbacks that came out gradually for oral administration of drugs and applying transdermal patches to deliver drugs across the skin became an attractive approach for the patients who are suffering painful injection but transdermal delivery, which relies on drugs passively diffusing across the skin is severely hindered by the low permeability of the outer skin. To increase permeability and reduce the pain simultaneously, the idea of combining the benefits of needle injection and transdermal patches was brought out, resulting in the creation of the microneedle concept which can be used for both drug delivery and extraction of biofluid for sampling.

2.2 Skin as a barrier

The skin is the largest organ of the body, with a total area of about 20 square feet. The skin protects us from entry of foreign elements but it is also a vital route for drug delivery and biofluid extraction. The human skin can be categorized in three primary layers: the topmost layer is epidermis, the layer underneath that is the dermis, and the deepest layer is hypodermis. It is epidermis layer that is optimally targeted for interstitial fluid extraction-superficial enough to be painless. The thickness of the epidermis layer is approximately 50-150 μm [18]. The two major layers of concern in the epidermis are the Stratum Corneum (SC) and the stratum spinosum. The topmost layer of the skin, which is what is exposed to the outside environment of the body, is the stratum corneum also called as horny layer and is the rate limiting barrier that restricts the inward and outward movement of chemical substances [17]. The stratum corneum is followed by two very thin layers called the stratum lucidum and the stratum granulosum. These layers are followed by the relatively thick stratum spinosum, the other primary layer of the epidermis. Between this layer and the dermis, which is the secondary layer of the skin after the epidermis, lies a thin separating layer called the stratum basale. The thickness of these layers will vary depending on where they are in the body but generally the thickness of the stratum

corneum is less than 40 μm where the thickness of the epidermis is between 0.2 and 0.3 mm [19]. Figure 2.1 shows the cross-sectional illustration of human skin.

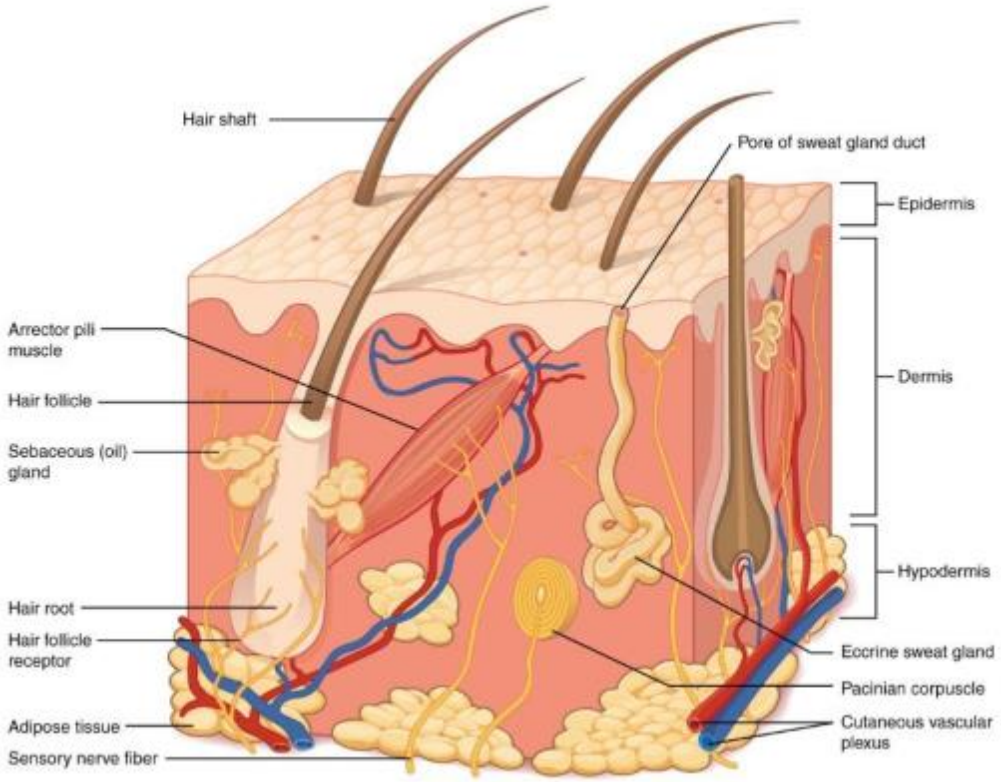

Figure 2.1 Cross-section of human skin [20].

2.2.1 Thickness of stratum corneum

A microneedle must be structured with the capacity to cut the skin effectively. This incorporates having a moderately sharp tip and a needle with a fairly high aspect ratio (the proportion of height to base length) and also a lumen (the inside space of a tubular structure, such as an artery or intesine) situated accurately so it doesn't plug up amid skin penetration. Drug penetration across the stratum corneum is limited primarily by the lipids organized in bilayer structures [26]. Understanding the distinctive layers of the skin will empower better plan and design of microneedle for progressively effective skin infiltration. Some typical approximation of the thicknesses of stratum

corneum and the entire epidermis at different regions of a grown-up body are shown in the table 2.2.

Body Location	Full Epidermal Thickness (µm)	Stratum Corneum Thickness (µm)
Elbow	325	70
Knee	210	35
Leg	195	35
Chest	205	25
Palm	210	45

Table 2.2 Tabulated thickness for the human epidermis and the stratum corneum at various body location [27].

2.2.2 ISF

Finding and observing of infection is regularly done by estimating biofluids found in blood, urine, spit, and other natural liquids. Another rich wellspring of biomarkers is the interstitial liquid that encompasses cells and tissues in the body, yet trouble in getting to this liquid has constrained its utilization in research and prescription. We conducted in vivo tests with experimental studies coupled with theoretical modeling to design microneedles that cut into the superficial layers of skin, and in this manner empower withdrawal of interstitial liquid through micro channels in a simple, straightforward non invasive manner. Researchers can access interstitial fluid using these microneedles to advance discovery of novel biomarkers and help doctors to use interstitial fluid for possible future diagnosis and monitoring of disease.

Chapter 3

Device Fabrication Tools and Techniques

The fabrication of out-of-plane and in-plane microneedles is explored and developed by utilizing microfabrication techniques. This chapter represents three key procedures explicitly utilized in the microneedle fabrication process which are photolithography, wet etch, and dry etch.

3.1 Photolithography

Photolithography is a staple of the microfabrication business. Developed in 1959, photolithography uses optical radiation to image the mask on a silicon wafer using photoresist layers. [29,30]. In general, photoresist, a photosensitive material, has two types, positive and negative. Upon exposure, the positive photoresist becomes more soluble. On the contrary, the negative photoresist becomes less soluble after exposure. The transfer of the pattern on the mask is done by the exposure process onto the photoresist. The patterns on a mask can be created down to ten of nanometers in size [30]. A simple representation of basic steps of photolithography is shown in Fig. 3.1. And in Fig. 3.2, the mechanism of positive and negative photoresist upon UV exposure is illustrated.

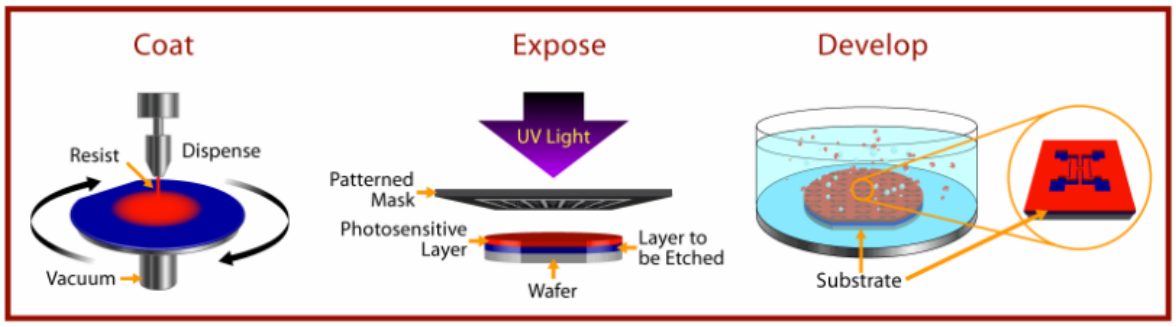

Figure 3.1 Basic steps of photolithography (source : www.scme-nm.org)

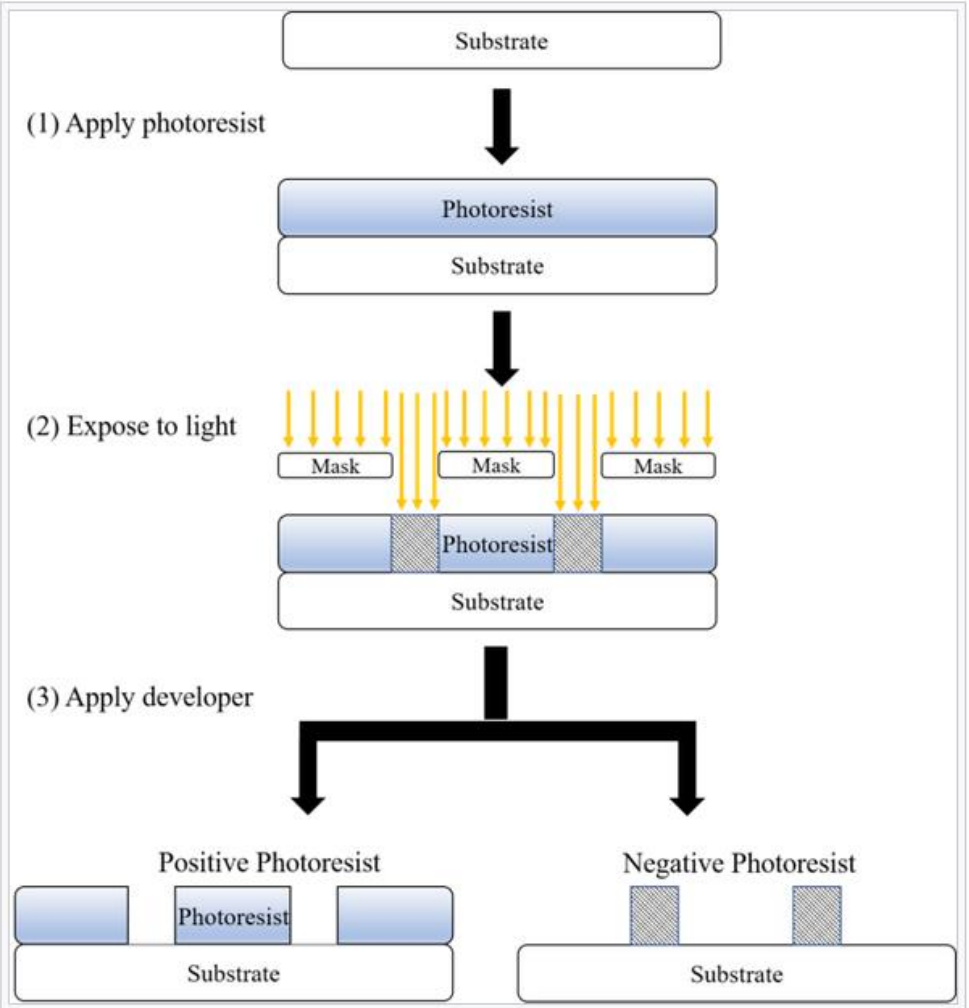

Figure 3.2 Positive and negative photoresist (source: wikipaedia).

As shown in Fig. 3.2, A mask with desired pattern needs to be created first. With spin-coating the substrate with a photoresist the photolithography process starts. Prior to this application of liquid form of photoresist, usually an adhesion promoter such as hexamethyldisilazane (HMDS) is spun on the wafer. The thickness of the photoresist depends on the spinning speed and photoresist viscosity and the thickness is typically in the range 0.5–2.5μm. In order to remove the solvents from the resist and improve adhesion a soft baking process is performed for 5 to 30 minutes at 60^{o} to 120^{o}. After this, the photomask with the desired structural feature which was prepared before is well positioned above the photoresist using a mask aligner, then UV light travels through and focuses on the photoresist layer that is going to be soluble or insoluble depending on which type of photoresist spun onto the substrate. After the

development, the defined pattern will act as a barrier to protect the underlying film from wet or dry etching in the following process. Ultimately, the pattern is transferred from a photomask to the substrate successfully. Fig 3.3 shows the picture of a lithography system we used at the University of Waterloo for alignment and UV exposure of resist-coated wafers.

Figure 3.3 MA/BA6 Mask Aligner (Courtesy to SUSS MicroTec).

In our project, we also used another method for pattern transferring, which is called maskless lithography that directly transfers the information onto the substrate by laser writing, without utilizing an intermediate photomask. Maskless lithography offers topside alignment and backside alignment with high accuracy. For this purpose, we used Heidelberg MLA150 maskless aligner for pattern transfer. Another advantage of using MLA150 maskless aligner is that it can expose an area of 100 x 100 mm^2 with structures as small as 1 micron in less than 100 minutes – independent of number of structures within this area. Alignment in multi-layer applications is achieved within less than a minute by using the integrated cameras with varying resolution. Layer to

layer alignment accuracy is better than 500 nm. Fig 3.4 shows the Heidelberg MLA150 maskless aligner in Quantum Nano Fab (QNF) we used.

Figure 3.4 Heidelberg MLA150 maskless aligner (source: https://www.himt.de/index.php/maskless-write-lasers.html)

Photolithography is a key step to transfer the pattern we designed to photoresist AZ4620 followed by wet or dry etching to define pillar and hole structures.

3.2 Etching

Etching is another fabrication step that is of fundamental importance to both VLSI processes and micro/nanofabrication. To selectively remove layers from the surface of a wafer resulting in desired patterns, etching is a critically essential process. The wafer is protected from the etchant by the photoresist that has been patterned using lithography acting as a masking material. It is often utilized in the microfabrication processes of semiconductor devices for the needs of wafer planarization, isolation, and cleaning.

There are several important metrics in the etching process such as uniformity, etching rate, selectivity, anisotropy and undercut. Selectivity is the degree to which the etchant can differentiate between the masking layer and the layer to be etched. Directionality has to do with the etch profile under the mask [31]. Another critical parameter in the etching process is anisotropy or isotropy. Figure 3.2.1 shows the difference between isotropic and anisotropic etching.

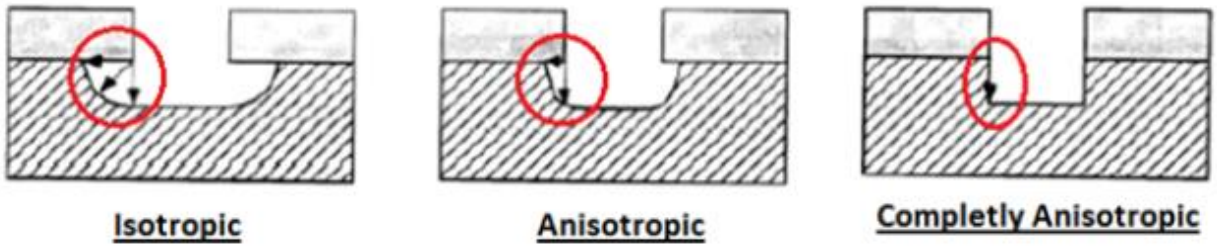

Figure 3.5 Schematic of isotropic, anisotropic and completely anisotropic etching [source: http://www.vlsi-expert.com/2014/07/effect-of-etching-process_28.html]

From Fig 3.5 we can see that, the etchant attacks the material in all directions at the same rate, hence creating a semicircular profile under the mask in an isotropic etch. In contrast, in an anisotropic etch, the dissolution rate depends on specific directions and straight side-walls or other noncircular profiles can be obtained.

Etching process can also be categorized by two fundamental techniques based on the type of etchant: wet etch (liquid-based etchants) and dry etch (plasma-based etchants).

In this chapter, using this classification different wet etching processes will be discussed followed by dry etching techniques.

3.2.1 Wet etching

The fundamental concept of wet etching is the conversion of solid materials into liquid compounds using different chemical solutions. These processes are usually done by dipping the substrate in the chemical solution or the substrate is sprayed by the solution. In general, a wet etching procedure includes one or more chemical reactions that eat the original reactants and bring new species. In wet etching, the selectivity is generally very high because the individual film can adapt the used chemicals very precisely.

A fundamental wet etching process entails three basic stages: 1) diffusion of the etchant to the surface; 2) the reaction between the liquid etchant and the material being etched away; and 3) diffusion of the reaction byproducts from the reacted surface. In Fig 3.6. the simple mechanisms of wet etching has shown. Wet etching is usually isotropic, i.e., it etches all directions at a similar rate.

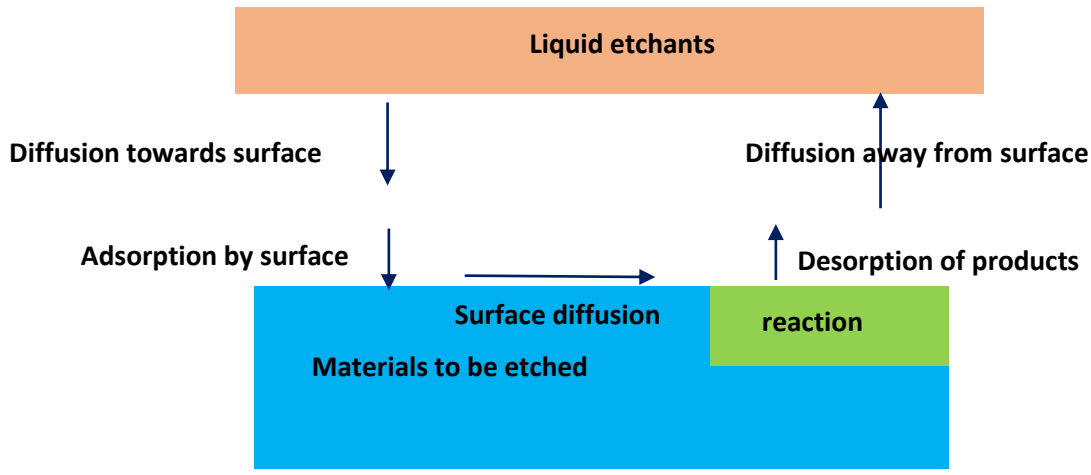

Figure 3.6 Three basic steps of wet etching.

3.2.1.1 Isotropic wet etching

From the 1950s to the present, for isotropic wet etching, a mixture of hydrofluoric acid, nitric acid, and acetic acid ($HF/HNO_3/CH_3$ COOH) is the most common etchant solvent used to thin down the silicon wafer. The etch rate is determined by the concentration of each etchant. Isotropic etching of silicon using $HF/HNO_3/CH_3$ COOH (various different formulations have been used) is still frequently used to thin down the silicon wafer. The etch mechanism for this combination has been elucidated and is as follows: silicon oxidization is done by HNO_3, which is subsequently dissolved away in the HF. The etch works as well without the acetic acid. For short etch times, silicon dioxide is usually used as a masking material against HNA (hydrofluoric, nitric, acetic) but for longer etch time silicon nitride is preferred. As the reaction takes place, the material is removed laterally at a rate similar to the speed of etching downward. This lateral and downward etching process takes places even with isotropic dry etching which is described in the dry etch section.

The reaction can be broken down into two simultaneous steps: (1) oxidation of silicon into silicon dioxide (SiO_2) by HNO_3 (Eq. (3.1)) and (2) SiO_2 removal using HF (Eq. (3.2)). In Eq. (3.3), the overall reaction is given. The important factor is here that the etching rate is limited by the rate of oxide removal. The rate-limiting factor will be the HF diffusion to the silicon surface which will result in more faster etching (shrinking) of the pillar top.

$3Si + 4HNO_3 = 3SiO_2 + 4NO + 2H_2O$ Eq. (3.1)

$SiO_2 + 6HF = H2SiF_6 + 2H_2O$ Eq. (3.2)

$3Si + 4HNO_3 + 18HF = 3H_2SiF_6 + 4NO + 8H_2O$ Eq. (3.3)

Two terms were introduced in 2010 on a wafer-scale etching technique based on R. Bhandari's research: (1) dynamic (with stirring) and (2) static etching(without stirring) [34]. Fig 3.8 illustrates the combination of etching progression with dynamic and static etching. Based on the abovementioned theories, in this work, to sharpen silicon pillars into a sharp needle-shaped profile a static wet etching system made up of the mixed solution HF (49%)–HNO_3 (69%) in a ratio of 1:19 by volume was utilized.

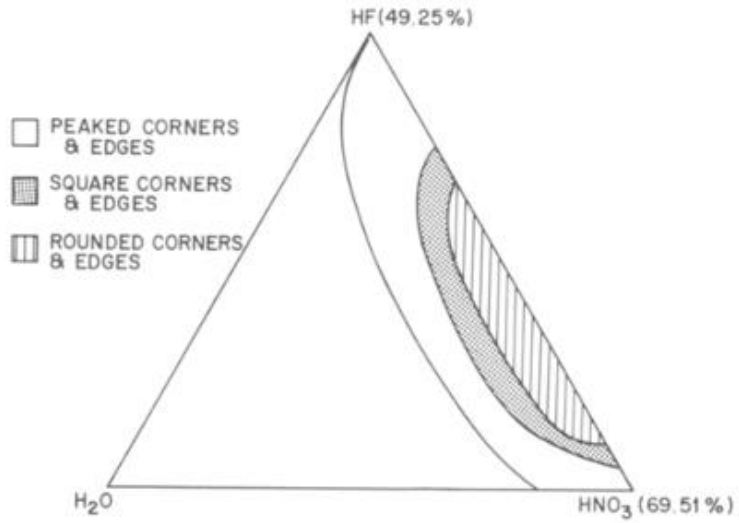

Figure 3.7 Curves of constant etch rate of silicon (mils/min) as a function of etchant composition in the system 49.25% HF, 69.51% HNO_3, and diluent [34].

Fig 3.7 demonstrates the observed geometry effects on the initially rectangular parallelepipeds. We can see that the geometry of the etched 25% HNO_3 on this axis, the geometry becomes square and the surface has a matte appearance. Further increase of HNO_3 above 35% is accompanied by progressive rounding of the corners and the development of a highly specular surface.

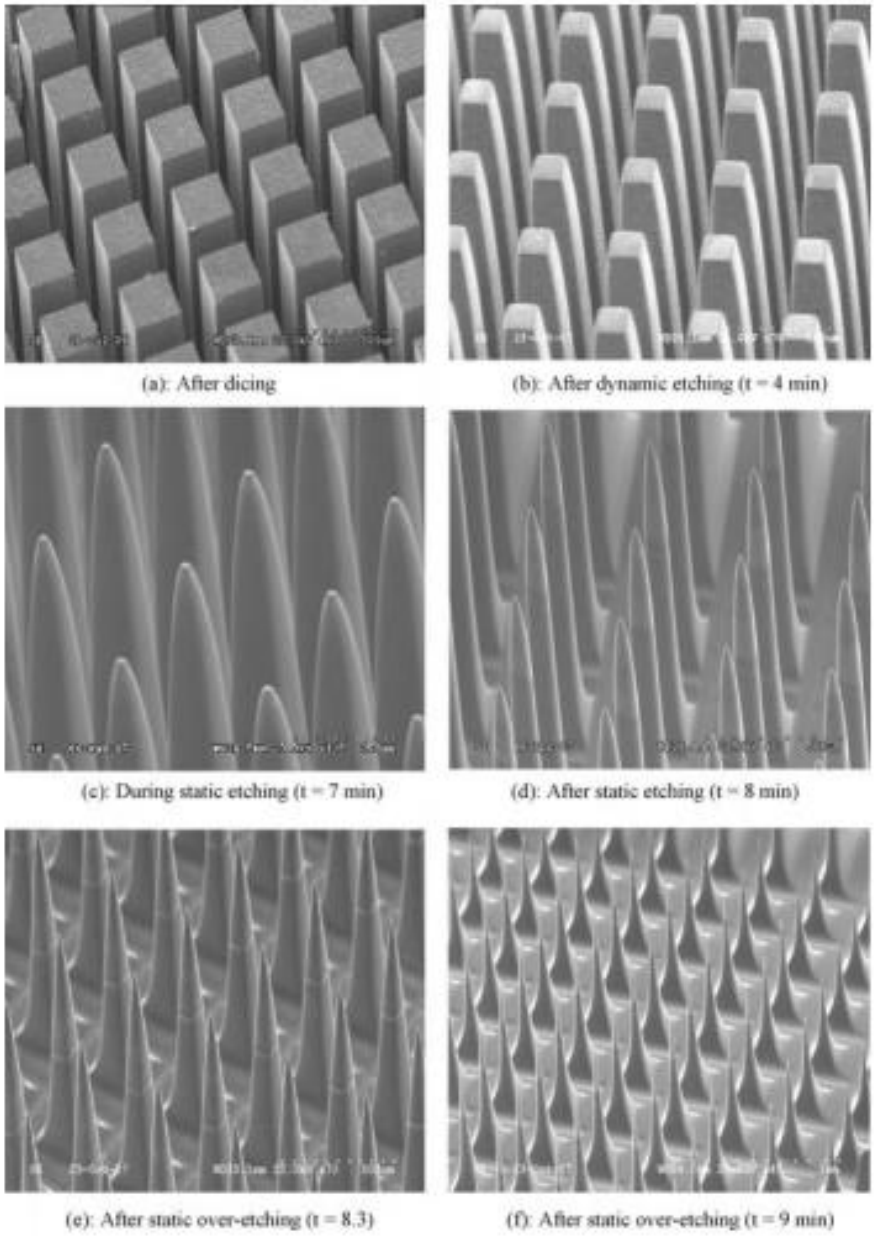

Figure 3.8 SEM images showing progress of needle formation from dicing through etching (a–f). The rectangular microneedless (a) are transformed into sharp needle shapes (d) during static etching (8min). The change in geometry is observed due to the high etch rate (20 μm/min) [35].

Underetching remains a problem in isotropic etching in the fabrication of precise lateral structures. The isotropic etch front has almost a spherical form if the etch solution is well stirred. While fabricating a microchannel with isotropic etching, the channel width is dependent on the channel depth, and mask design needs to be

considered. But the major advantages of wet etching are high selectivity, a relatively planar etching surface, and the controllable etch rate. For removing thin layers isotropic wet etching is often used. Well-stirred etch solution is necessary for this process because of the possible bubble formation on the etched front. In table 3.1 some common recipes for isotropic wet etching are listed.

Materials	Etchants	Selective to
Si	$HF/HNO_3/CH_3COOH$	SiO_2, Si_3N_4
Si	KOH	SiO_2, Si_3N_4
SiO_2	NHF_4, HF	Si
SiO_2	HF, H_2O	Si
Si_3N_4	H_3PO_4	SiO_2
Al	H_3PO_4, HNO_3, H_2O	SiO_2

Table 3.1 Common recipes for isotropic wet etching

3.2.1.2 Anisotropic wet etching

In semiconductor manufacturing processes, anisotropic etching is preferable. As mentioned before, most wet etching profiles are isotropic but an exception is seen for etching crystalline materials, whereas etching profiles of dry etching are anisotropic.

Anisotropic etching of silicon is typically accomplished by KOH. Crystalline orientation determines the etch rate of KOH in single-crystalline silicon. The <111> plane of the silicon crystal has two orders of magnitude slower etch rate than the <100> plane; so, the <111> plane defines the single-crystalline structures etched in KOH. For this reason, the etching process in KOH is also called anisotropic etching. Since this innovation is a wet-etching process, the equipment is straightforward and simple .Anisotropic etching in KOH is not compatible with standard CMOS processes because of the fact that KOH is a source of mobile ion contamination. By using a barrier layer or a metal-ion free etchant such as Tetramethylammonium hydroxide (TMAH) the problem of metal ions can be mitigated. For precise fabrication with anisotropic wet etching, controlled etch stop plays an important role. Different methods to reduce the etch rate are:

(a) Silicon surface can be coated with a protective layer such as nitride or oxide;

(b) The dependence of etch rate on orientation; and

(c) Controlled hole generation.

Polycrystalline materials like silicon shows usually anisotropic etching because an etch rate selectivity 400 times higher in the <100> crystal direction than in the <111> direction is shown using etchants like potassium hydroxide (KOH). An anisotropic wet etch on a silicon wafer creates a cavity with a trapezoidal cross-section. The bottom of the cavity is a <100> plane, and the sides are <111> planes, see Fig. 3.9 [32]

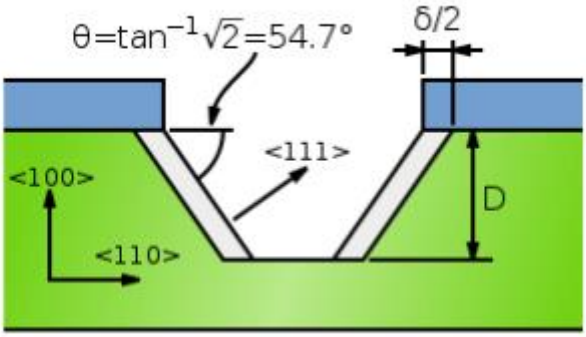

Figure 3.9 Anisotropic wet etch on Si wafer. The blue material is an etch mask, and the green material is silicon [32].

By using KOH wet etching technology, silicon microneedle structures with high accuracy and good reproducibility can be fabricated based on the etching rate ratio between the crystal planes in the silicon lattice. In 2005, a research group in Tyndall National Institute produced a systematic method of microneedle manufacturing with well-defined structures [33]. The process flow chart starting from a standard, P-type, bare silicon wafer with orientation of (100) is shown in Fig. 3.10. As it is shown, via wet etching process, the exploitation of silicon microstructures with high index crystal planes forming microneedle shapes is done by using 29% KOH and a temperature of 79 °C. In step 3 the illustration of the formation of (111) silicon crystal planes are visible. With an octagon at the base, (111) crystal planes are etched away by faster etching planes (etch rate > 1.3 μm/min) after a certain etch depth. The needle shape is

defined by the eight high index crystal planes, defined as (312) planes [33]. Fig 3.11 illustrates the result of one single microneedle shape with a height of 280 μm.

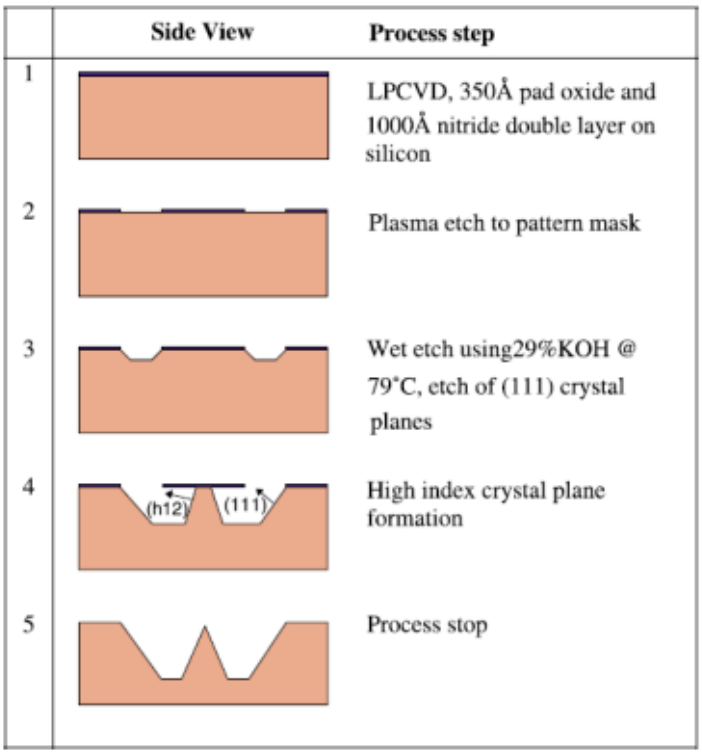

Figure 3.10 Simple wet etch process flow [33]

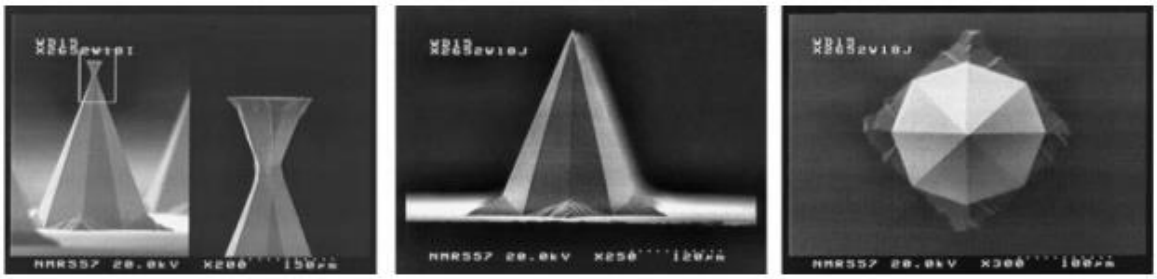

Figure 3.11 SEM picture of a single microneedle: side view with detail of negative slope etch (left); side view (middle); top view (right) [33].

3.2.2 Dry etch

Dry etching was first introduced in late 1970's and is one of the most widely used processes in today's semiconductor manufacturing because it is easier to control, is capable of defining feature sizes smaller than 100 nm, and it is capable of producing highly anisotropic etching. In dry etching, the substrate material is removed by

chemical reactions, by purely physical methods, or with a combination of both chemical reaction and physical bombardment.

Plasma may be a totally or partly ionized gas composed of equal numbers of positive and negative charges, in addition to some neutral molecules. By applying a strong radio frequency electromagnetic field to a gas, plasma can be created, which will break down gas molecules and generates ions, free radicals, electrons, photons and reaction by-products such as ozone. These reactive species have high energy so they create highly active and low-temperature plasma which is used to etch materials precisely and efficiently. A simple representation of how plasma interacts with silicon substrate is shown in Fig 3.12.

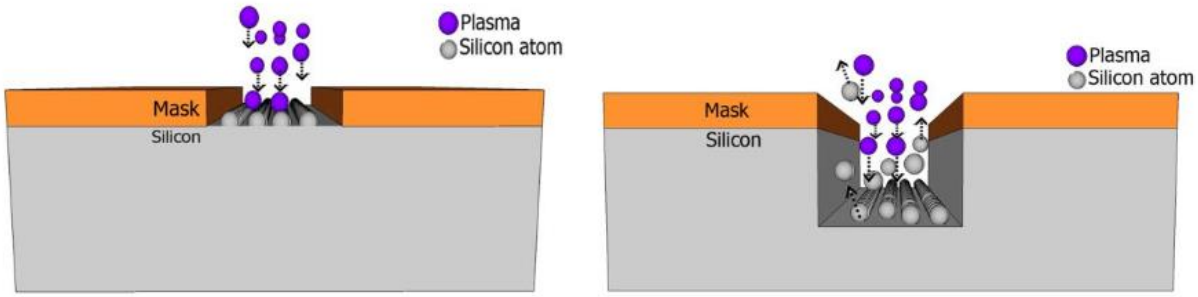

Figure 3.12 Interaction between plasma and silicon atom

Dry etching has many advantages when compared with wet etching. These include higher anisotropy and smaller undercut. However, the selectivity of dry etching techniques is poorer than that of wet etchants, and one must take into account the finite etch rate of the masking materials. There are mainly three basic dry etching techniques, namely high-pressure plasma etching, reactive-ion etching (RIE), and ion milling, utilize different mechanisms to obtain directionality.

The three basic dry plasma etching techniques are depicted in Fig 3.13. It shows plasma gives rise to isotropic profiles, high etch rates and high selectivity, but ion milling presents positively tapered profiles, low selectivity and low etch rates, whereas RIE enables the achievement of profile control due to the synergetic

combination of physical sputtering with chemical activity of reactive species with high etch rate and high selectivity [35].

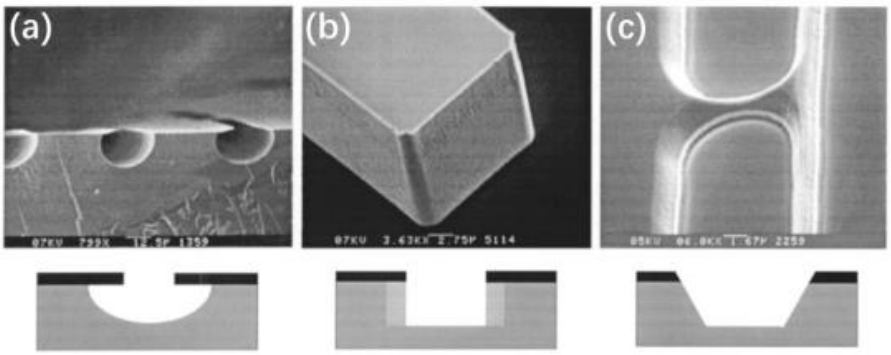

Figure 3.13 Typical etching profiles of the three basic mechanisms of dry plasma etching. (a) plasma etching (b) reactive ion etching (RIE) and (c) Ion milling. (Courtesy to H. Jansen, H. Gardeniers, etc.)

If the etching relies only on ion bombardment, it becomes very time consuming and inefficient. Thus reactive ion etching (RIE) has been considered one of the most diverse and most widely used processes in industry and research. The process is much faster since the process combines both physical and chemical interactions. In Fig 3.14, we can see the comparison between the etch rates with or without the aid of Ar ion beam. By pure chemical or physical dry etch alone, very slow etch rate is achieved whereas it is more efficient and faster when it is ion-assisted chemical etch.

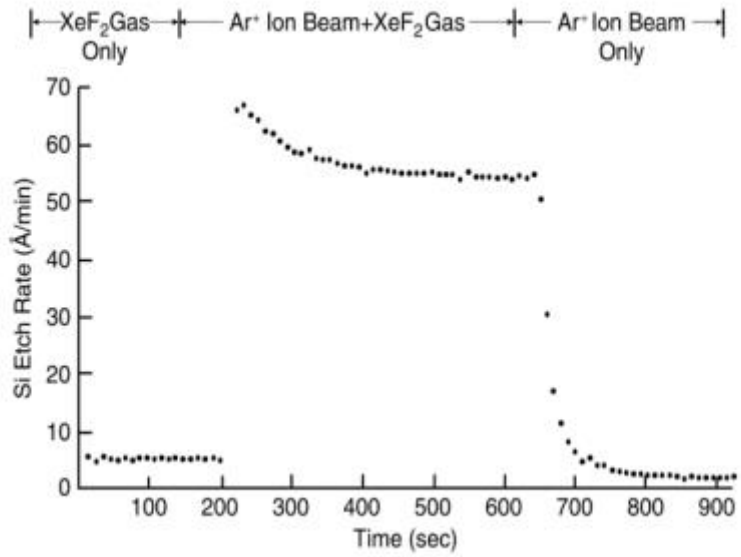

Figure 3.14 Etch rates of silicon as only XeF_2 gas, only Ar ion beam, and combination of them are introduced to the silicon surface. Ion-assisted chemical etch increases the efficiency of the etching.

In RIE, several gases are introduced inside a reactor where the substrate is placed. Using an RF power source, a plasma is struck in the gas mixture which breaks the gas molecules into ions. This is illustrated in Fig 3.15. In the chemical part of reactive ion etching, the free radicals are accelerated towards, and reacts at, the surface of the material being etched, forming another gaseous material. The physical part which is similar in nature to the sputtering deposition process is also important. If the ions gain high enough energy, without the help of chemical reaction, they can knock atoms out of the material to be etched. To balance the chemical and physical etching, the development of a dry etch process is a very complex task. Anisotropy can be influenced by changing the balance since the chemical part is isotropic and the physical part is highly anisotropic; the combination can form sidewalls that have shapes from rounded to vertical. In some cases, the sample chuck temperature is deliberately elevated to boost volatility of the product. A schematic of a typical reactive ion etching is shown in the Fig 3.16.

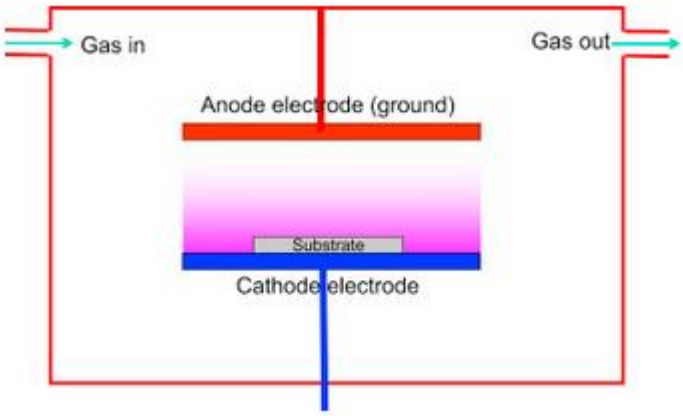

Figure 3.15 simple RIE configuration (source: https://www.sciencedirect.com/topics/materials-science/plasma-etching)

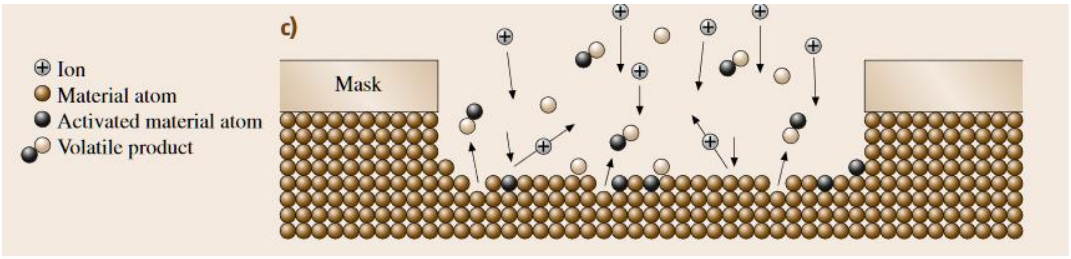

Figure 3.16 Simple RIE process [35].

One advantage of RIE system is that reasonably safe gases can be supplied into the chamber. CF_4 is an example of this. In plasma this gas can generate many F atoms (free radicals) and these free radicals are extremely reactive and spontaneously attack silicon and produce SiF_4. However, this gas shows fairly inert nature under normal conditions. In such plasma reaction, silicon will be readily turned to SiF_4. In addition, ions in the plasma will bombard the cathode similar to sputtering. This action creates an additional source of energy that can accelerate the etch rate parallel to the ion trajectories. Because ions are directed at normal incidence to the cathode, this has the effect of accelerating the etch rate normal to the substrate. This will result in an etch profile that has minimal undercut and is strongly anisotropic. Different reaction steps of RIE for Si etching by using CF_4 is shown in Fig 3.17 [35].

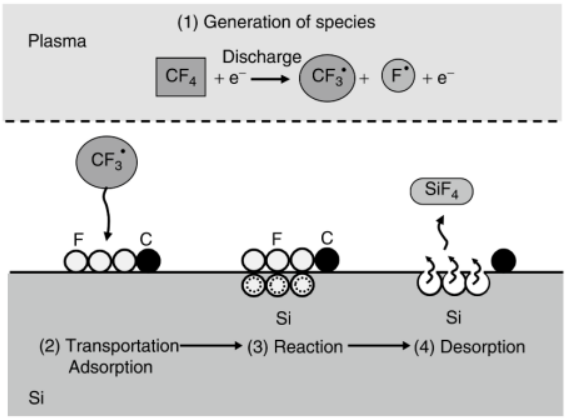

Figure 3.17 Reaction steps of RIE using CF4 for Si etching [35].

Using RIE technique, the directionality of the ion's velocity produces much more collisions on the horizontal surfaces than on the walls which generates faster etching

rates in the vertical direction. In some cases, side-wall passivation methods are used to increase the etch anisotropy further.

In mid-90's, $SF_6/CHF_3/O_2$ based silicon etching systems were most popular options for anisotropic silicon etching. However, by 2000's a new deep silicon etching technique was developed by researchers at Robert Bosch GmbH, currently known as Bosch Process which is capable of achieving aspect ratios of 30:1 and silicon etching rates of 10 – 20μm/min and using this technique through wafer etch is also possible.

In this technique, the passivation deposition and etching steps are performed sequencially in a two-step cycle, as shown in Fig 3.18 [37,38]. SF_6/Ar is typically used for the etching step and a combination of Ar and a fluoropolymer (nCF_2) for the passivation step is used in commercial silicon DRIE etchers. With a typical thickness about 50 nm, a Teflon-like polymer is deposited during the latter step, covering only the side-walls where Ar+ ion bombardment removes the Teflon on the horizontal surface. Because of the cyclic nature of this method, the side-walls of the etched structures exhibit a periodic wave-shaped roughness of 50 – 400 nm. Fi 3.19 shows some micro/nano structures with high aspect ratio etched using DRIE process [39].

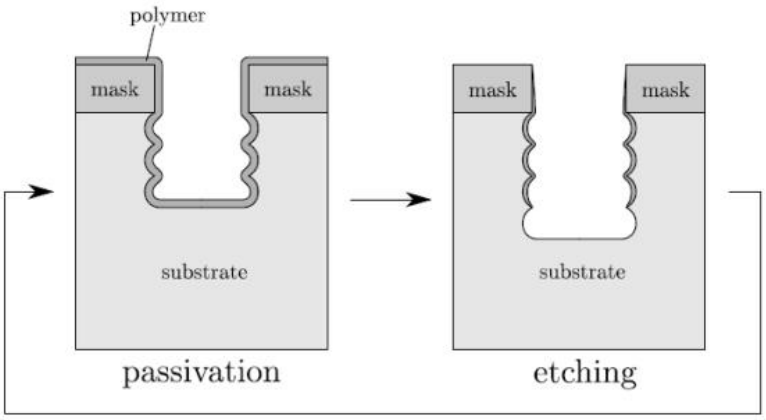

Figure 3.18 Bosch process and the alternation between the passivation and etching step [37,38].

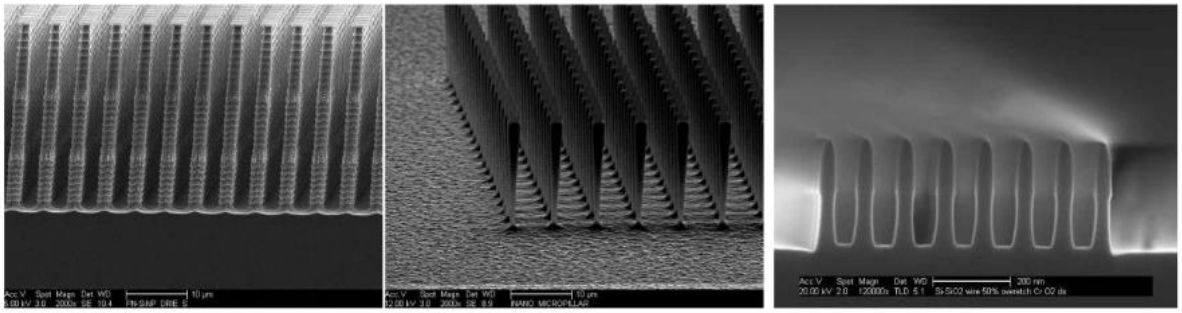

a b c

Figure 3.19 High aspect ratio micro/nano structures using DRIE process [39].

To sum up wet etch can be easily implemented in the experiment with quick reaction, but it is quite a difficult task to control and define the precise feature sizes that are smaller than 1 μm. Alternatively, dry etch like DRIE process itself is an established approach to create structures (pillars and holes in our work) with fairly high aspect ratio. But it is a major challenge to develop an optimized recipe for etching of microneedles. In our research, we exploited both dry etch and wet etch within the experiments.

Chapter 4

Overview of Microneedles

As a conventional drug delivery method, oral administration of drugs was considered in the past, but gradually some downsides came out because such techniques are often not applicable for new protein based, DNA-based, and other therapeutic compounds produced by modern biotechnology [40-42]. For the patients who have needle phobia, also to reduce hypersensitivity, bruising, discomfort and bleeding at the site of administration, applying transdermal patches to deliver drugs across the skin became an attractive approach. However, delivery of active pharmaceutical ingredients through transdermal route is severely restricted and hindered due to low permeability and the excellent barrier properties of the stratum corneum of the skin as we discussed in chapter one [43-44].

Disrupting the barrier properties and increasing the permeability of the stratum corneum is one of the techniques utilized in enhancing transdermal drug delivery. With this intention, the idea of combining the benefits of needle injection and transdermal patches is brought out. Microneedles are generally hundreds of microns long, few to tens of microns wide at the tip, and on the order of 100 μm wide at the base and they can painlessly penetrate the SC and create micropores through which drug molecules can readily permeate, and they can also collect sample of interstitial fluid painlessly. Even though the concept of microneedles was first introduced in 1976, it was not possible to make such micron-sized medical devices until the first exploitation of microelectromechanical systems (MEMS) for this purpose in 1998 [45]. Therefore, this chapter will focus on some of the basic designs and materials used to fabricate microneedles.

4.1 Types of microneedles and applications

A microneedle is a needle with delicate parts on the micrometer length scale. In spite of the fact that there are numerous instances of "microneedles" with lengths of a couple of millimeters, a typical comprehension of microneedles is that the length of the needle is shorter than 1 mm. What can be said is that microneedles are altogether smaller than normal needles, particularly concerning the length. A classification for microneedles usually used in literature is based on the fabrication process: in-plane or out-of-plane microneedles. In-plane needles are arranged along the plane of the substrate while out-of-plane needles are arranged perpendicular to the plane of the substrate. Fig 4.1 shows the comparison between the orientation of in-plane and out-of-plane microneedles [28].

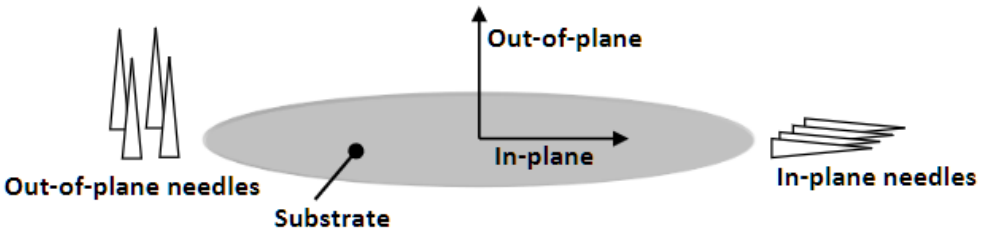

Figure 4.1 Orientation of In-plane and Out-of-plane microneedles [28].

Microneedles can be divided into two major categories which are; solid and hollow. Different materials can be used to fabricate each of these and they can be applied to different functionality depending on their designs.

4.2 Solid microneedles

Solid microneedles are usually much stronger, sharper and easier to fabricate than hollow microneedles [16]. They are effective for drug transport because of their mechanical strength and sharper tip [46]. For delivering a variety of substances such as 5-aminolevulinic acid, Insulin, DNA, and vitamins solid microneedles have been fabricated out of silicon, polymers and metal [47].

4.2.1 Silicon solid microneedle structures

Silicon was used as the first material to fabricate solid microneedles for pre-treatment of skin prior to patch application [48]. In 1998 Henry showed that silicon microneedles were able to increase skin permeability to Calcein by up to 3 orders of magnitude when compared to diffusion of Calcein through intact skin. In these experiments, silicon microneedles were inserted into the human skin obtained from autopsy; using a Franz diffusion cell, the group measured the permeability of Calcein through the epidermis for instances where the skin was first pre-treated with microneedles and compared this with the permeability of Calcein through intact skin without microneedles inserted. In terms of increasing the transport of drugs through the skin by a great extent, this experiment proved this technique to be effective (Fig 4.2) [48].

Figure 4.2 Permeability of drug through skin with no microneedles inserted, microneedles inserted and remained inserted during topical application of drug, microneedles inserted then removed after 10 seconds, and microneedles inserted then removed after 1hour [48].

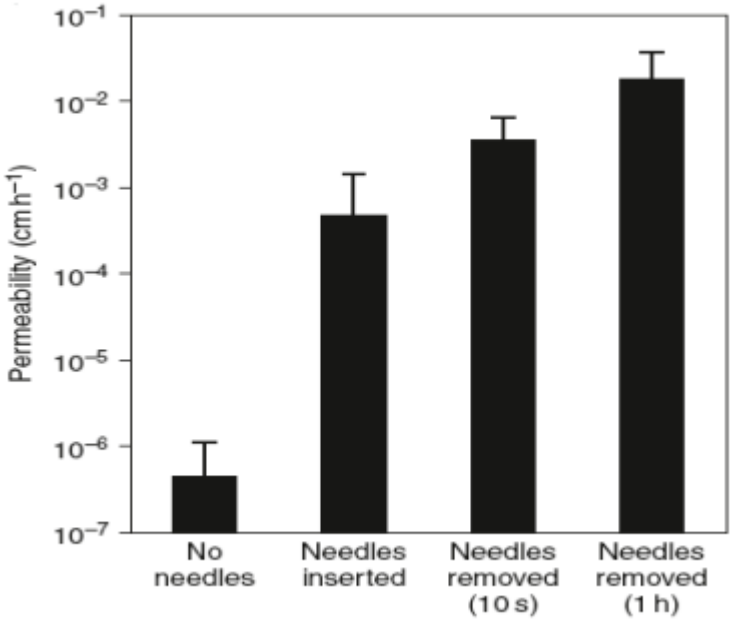

An out-of-plane silicon needle array featuring 100 μm diameter, 1.5 mm long needles on an area of 4.2 mm × 4.2 mm was one of the earliest stated microneedles in the scientific literature (Fig 4.3) [49]. These needles are used as electrical electrodes and designed to stimulate the visual cortex of the brain in order to regain sight because of their extreme slenderness. Associated to this application, in-plane microneedle probes are now used for activity recording and cellular chemostimuli of brain tissue [50,51]. Solid out-of-plane microneedles have been used to penetrate the stratum corneum to facilitate EEG (Electroencephalogram) measurements for anesthesia monitoring [52,53].

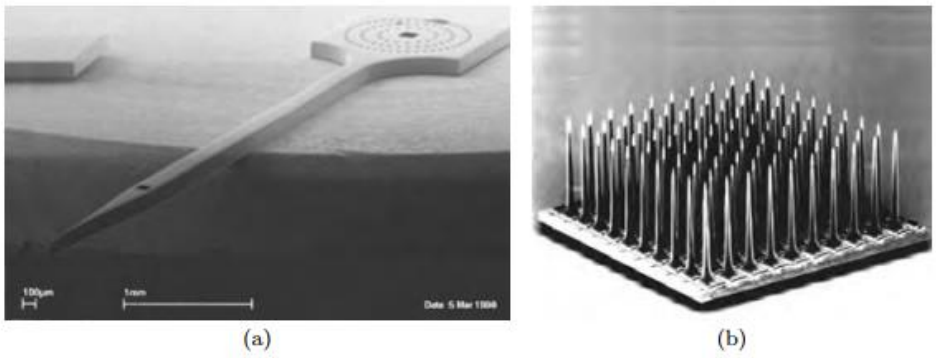

Figure 4.3 (a) 6 mm long, hollow, in-plane microneedle [54]. (b) Individually addressable, 1.5 mm long, solid, out-of-plane microneedles used as electrodes [49].

Another example of solid microneedle using silicon is shown in Fig 4.4 [55]

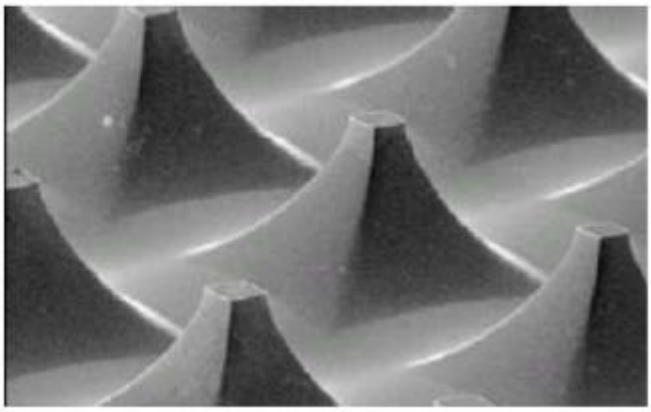

Figure 4.4 Silicon microneedle array used for gene delivery in skin [55].

4.2.2 Polymer solid microneedle structures

Because of the brittleness and cost of silicon [56], as alternative to silicon solid microneedles have been fabricated out of different polymer materials. Another advantage of polymer microneedles is its biodegradable nature. Compared to silicon, polymer is a cheaper, and embossing for mass production has been proposed for obtaining polymer microneedle structures [57]. Various types of biocompatible polymers such a poly-glycolic acid (PGA) [58] and polycarbonate (PC) [59] have been used to fabricate microneedles. Jung-Hwan Park and his research group presented PDMS micromolding technique to fabricate an array of 200 PGA solid microneedles in 2007 [60-61]. Microneedle master structures were fabricated using microlenses etched into a glass substrate that focused light through SU-8 negative resist to produce sharply tapered structures [61]. Fig 4.5 (a) shows the results after replicating SU-8 master structures using PDMS micromolding technique.

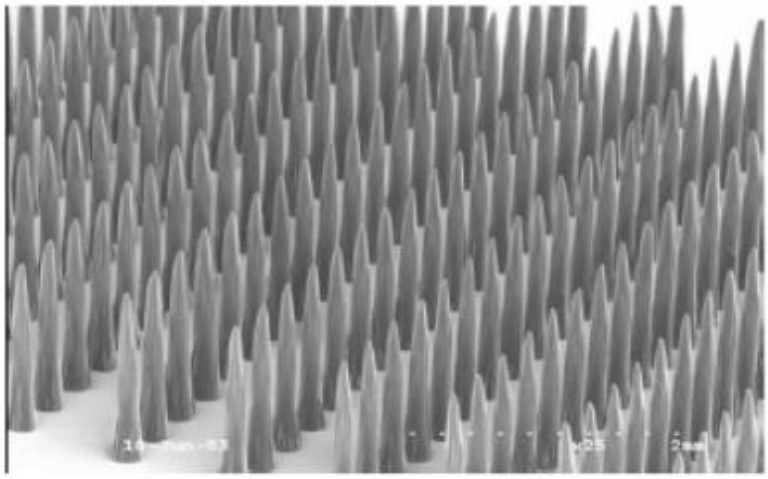

Figure 4.5 Tapered solid microneedles made of PGA [61].

In contrast, polymers are limited by their mechanical properties. The tips of microneedles fabricated using polymers are inevitably blunt due to the low modulus and yield strength of polymers [62]. Using biodegradable polymers, beveled tip and tapered microneedles have been fabricated (Fig 4.6) [63]. As the main material for the fabrication of many polymer microneedles, polyglycolic acid (PGA) has been chosen because it is relatively inexpensive and believed to be mechanically strong [64].

Moreover, the viscoelastic property of polymers may allow more mechanical flexibility of the materials, thus reducing chances of damage during handling [65].

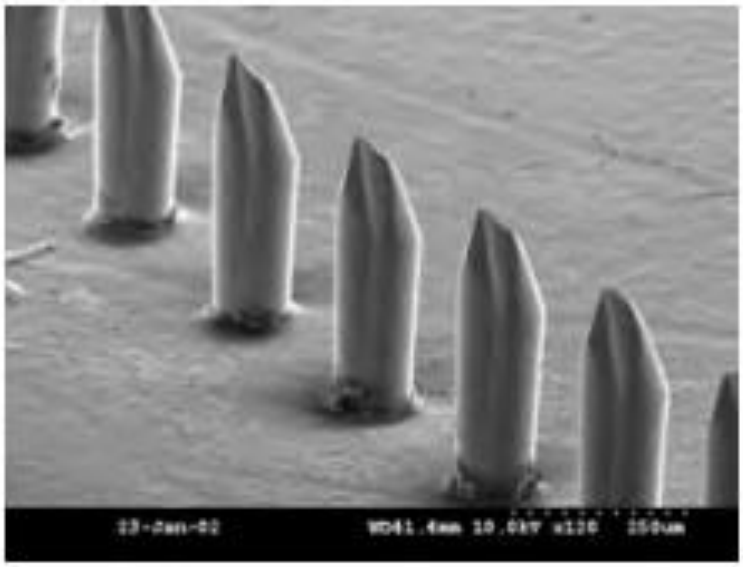

Figure 4.6 Biodegradable microneedles (beveled microneedles inserted through human epidermal tissue in vitro). The needles are approximately 400 μm long [63].

4.2.3 Metal solid microneedles

In transdermal drug delivery application, microneedles fabricated out of metal are commonly used which can be for example steel [66] or titanium [67] using the poke with patch method. For example, using the poke with patch method, Martanto et al (2004) have used laser-cut steel microneedles for transdermal insulin delivery. The blood glucose level in the diabetic rats was observed to have decreased by as much as 80% following Insulin delivery using microneedles. Fig 4.7 shows the comparison between the results obtained for blood glucose levels after microneedle and hypodermic needle insulin delivery [68].

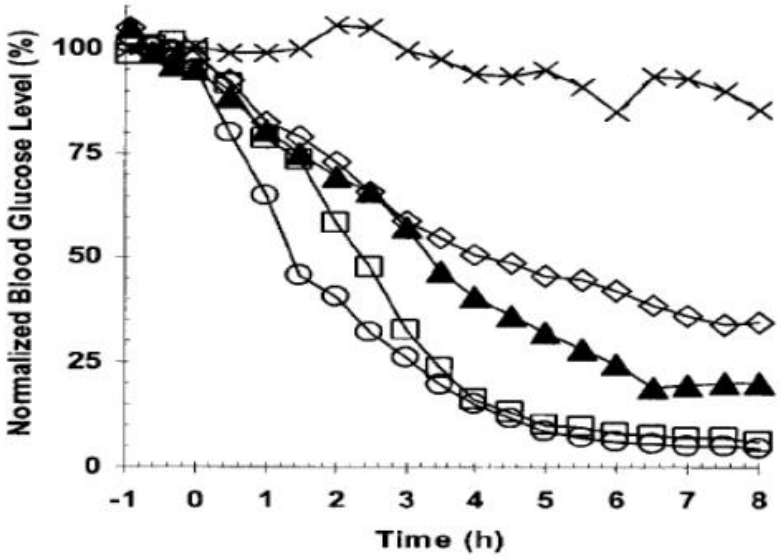

Figure 4.7 Changes in blood glucose level of hairless rat after Insulin delivery via different routes. Dark triangles indicate microneedle delivery while the X indicates delivery across untreated skin. Other symbols indicate delivery using hypodermic needles [68].

Many companies now fabricate solid metal microneedles array. An example of solid stainless microneedles is shown in Fig 4.8.

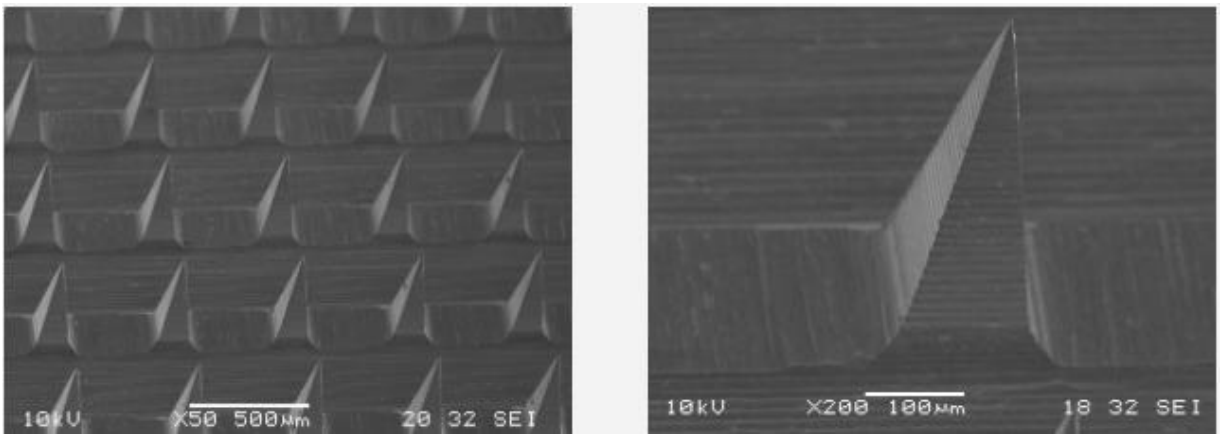

Figure 4.8 Stainless steel microneedle arrays SEM micrograph of a sharp stainless steel microneedle (source: https://micropoint-tech.com/technology-of-micropoint/)

4.3 Hollow microneedles

Hollow microneedles are generally used for fluid infusion of liquid drug and nanoparticles into the skin. Although due to the expensive fabrication methods they

are less widely used. But less expensive methods of fabricating hollow microneedles are evolving [69].

Despite the advanced fabrication strategies needed to get them, hollow microneedles need simpler formulations without the necessity to formulate a coating method. Hollow microneedles were used into inject Insulin to hairless rat skins [70]. Although hollow microneedles are more prone to fracture on insertion to skin than solid microneedles, they pose the advantage over most solid microneedles of being able to provide continuous infusion into the skin. Furthermore, there have been some efforts to resolve the limitations associated with infusion using hollow microneedles such as blockage of the tip while inserted in the skin. Side opened hollow microneedles has been designed and fabricated to address the decreased infusion rate caused by a blockage at the microneedle tip [71]. Fabrication of pocketed microneedles as an intermediate between hollow and solid microneedles can be used to provide nanoparticles and larger solids into the skin [72]. Hollow microneedles can be fabricated out of silicon, metal as well as polymer materials.

4.3.1 Silicon hollow microneedles

In 1999, the first hollow out-of-plane microneedles were produced [73]. Because of their mechanical properties and their biocompatibility potential, silicon microneedles are justified. Fig 4.9 shows that 150 μm long hollow silicon microneedles can be fabricated by combining the fabrication process of solid silicon microneedles with DRIE Bosch process to create a hollow shell structures with high aspect ratio, and afterwards isotropic wet etching processes were used to obtain sharper tips [73-74].

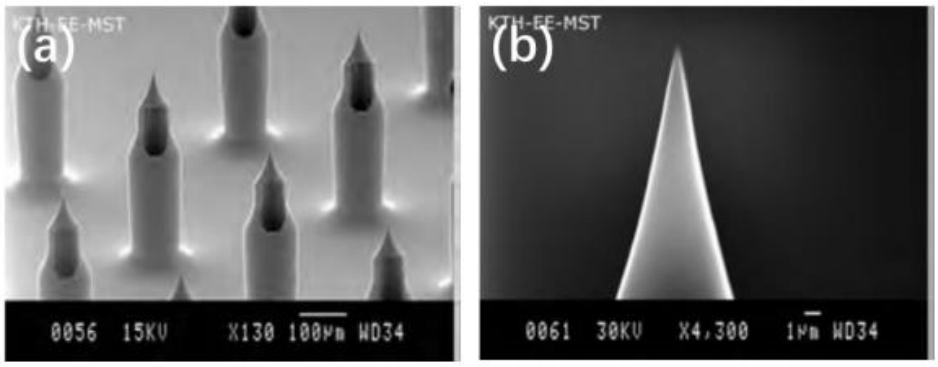

Figure 4.9 The circular side-opened design developed [73]. (a) 400 μm long, ultra-sharp, side-opened microneedles. (b) Magnified view of the microneedle tip. The tip-radius is below 100nm [75]

Clogging issue must be considered discreetly once the microneedles were tested on human, no matter for drug delivery or biofluid extraction. To avoid the clogging a method was developed using side-opened microneedles [79]. By combining anisotropic DRIE and isotropic dry etching of silicon, a three-dimensional needle structure was formed that intersects with the needle bore at the shaft of the needle (Fig 4.10). The 210 μm needles have a relatively low fluidic resistance and were capable of penetrating aluminum foil without being damaged.

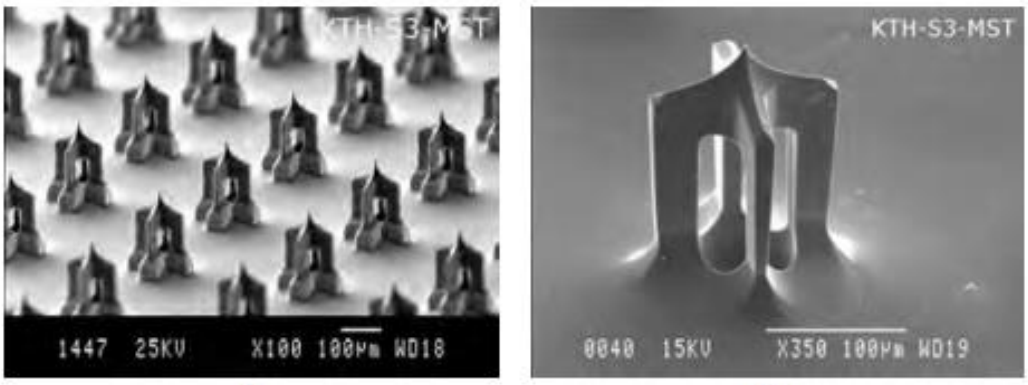

Figure 4.10 Cross-shaped, hollow, side-opened, silicon microneedles (a) Needles with a 50 μm long base shaft. (b) Needles without a base shaft [79].

In 2003, an approach to fabricate tetrahedrally-shaped hollow microneedles in silicon by combining DRIE and wet etching by KOH was presented (Fig 4.11) [80]. The main

advantage of such approach is that the needles become really sharp as a result of intersecting crystal planes while the tetrahedral shape ensures mechanical robustness.

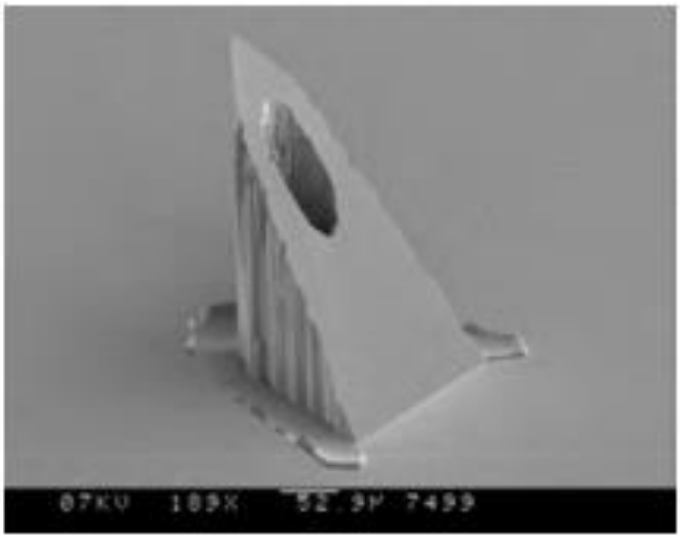

Figure 4.11 350 μm long silicon microneedle etched by combining DRIE and wet etching [80].

Another type of hollow silicon microneedles was presented in 2000 [76-77]. Using DRIE the fabrication of about 200 μm long needles starts by etching the needle bores from the backside of the silicon wafer. The front side of the wafer was etched by isotropic dry etching (Fig 4.12). In a later study, the needles were tested by delivery of methyl nicotinate (a vasodilating agent) into human subjects [78]. On a standard 1 ml syringe, microneedle array chips containing a few needles were mounted and pressed against the subject's volar forearm while injecting. It was estimated that nearly 1 μl (0.1 M concentration) was injected during the 30 second administration period.

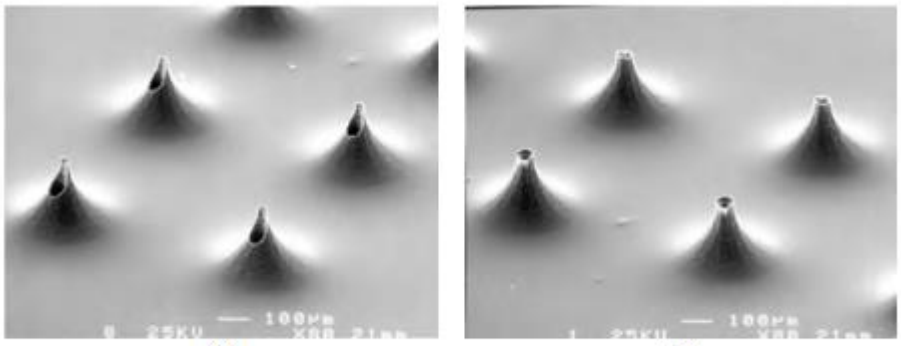

(a) (b)

Figure 4.12 Hollow silicon microneedles. (a) Pointed tip. (b) Flat tip [78].

4.3.2 Metal hollow microneedles

Metal hollow microneedle patches are typically produced by forming microneedle-shaped cavities using polymer followed by electro-deposition of metal on top of them [81-85]. Fig 4.13 (a,b) shows the SEM images of the first metallic hollow microneedle manufactured in 1999 [83]. According to the research, skin permeability increased up to 100,000-fold by hollow microneedles.

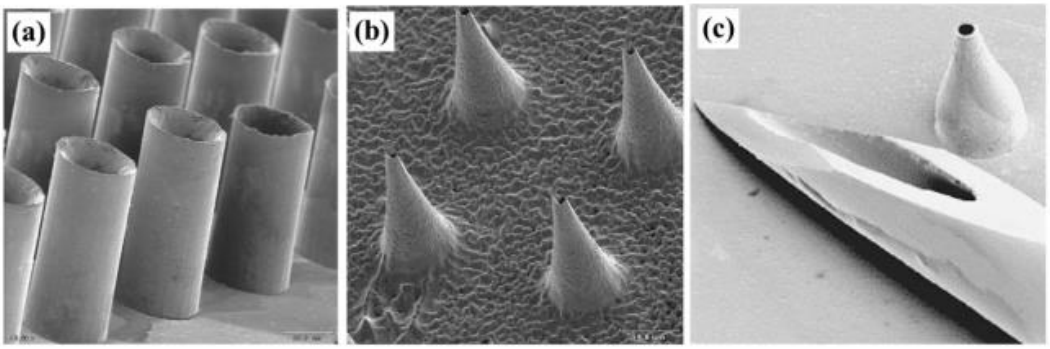

Figure 4.13 Nickel hollow microneedles: (a) hollow microneedles with blunt tip [82] (b) hollow microneedles with sharp tip [83] (c) hollow microneedle formed by electrodeposition of metal onto a polymer mold used for needle insertion and fracture force measurements [84].

An SEM image of the 37 hollow microneedle array fabricated with NiFe, alongside a 26-gauge hypodermic needle is shown in Fig 4.14 (a). The fabrication method for the hollow microneedle array involved creating solid microneedles first using the silicon RIE technique, and creating a female-mold for silicon solid microneedles using SU-8 photoresist, followed by electro-deposition of NiFe [81]. Using the fabricated hollow microneedles, skin permeability testing for calcein, insulin, BSA, and nanospheres (25 nm) was conducted.

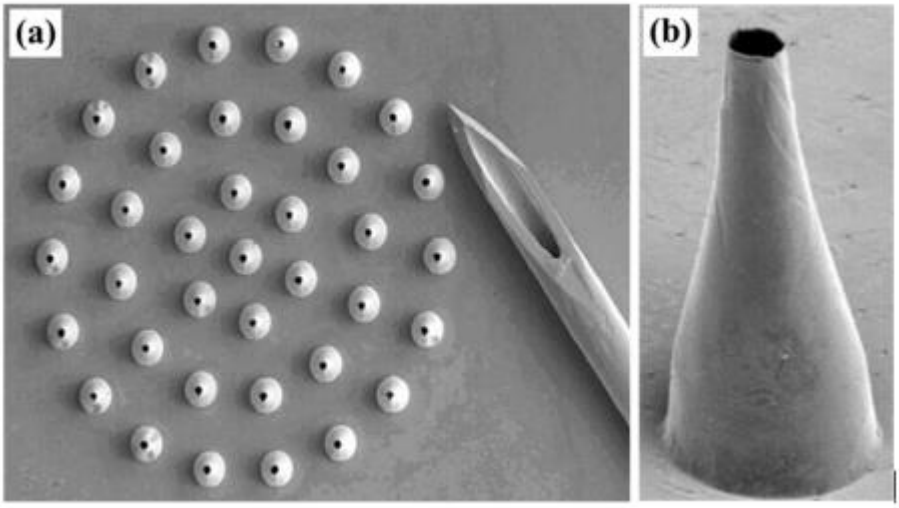

Figure 4.14 NiFe hollow microneedles (a) array of tapered metal microneedles shown next to the tip of a 26-gauge hypodermic needle, (b) a single tapered metal microneedle made by electro-deposition onto a polymeric mold [81].

4.3.3 Polymer hollow microneedles

A similar microneedle design to the Fig 4.15 was presented by Moon and Lee [86]. But instead of silicon, the needles were fabricated in polymer PMMA (polymethyl methacrylate) using LIGA-techniques with inclined x-ray exposure (Fig 4.15) [87]. The noticeable fact was that 900 μm needles were demonstrated to cause bleeding after insertion to the back of a human hand while insertion into a fingertip did not cause any bleeding.

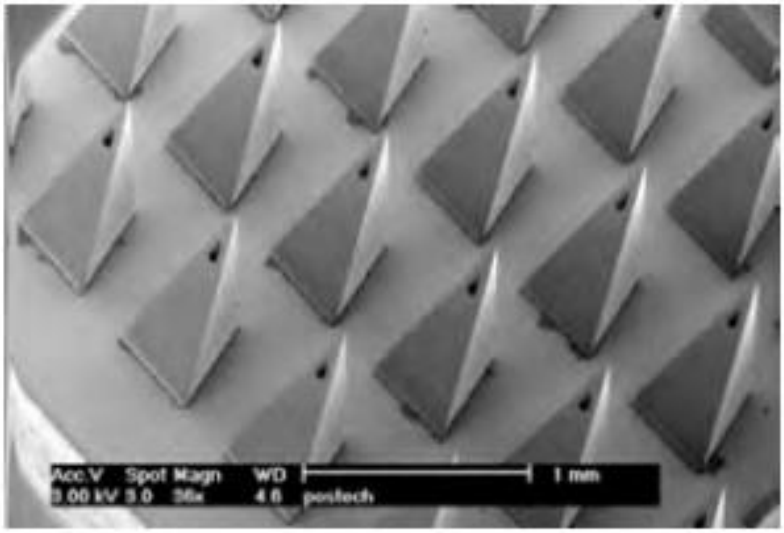

Figure 4.15 Microneedles made in PMMA using LIGA techniques [86].

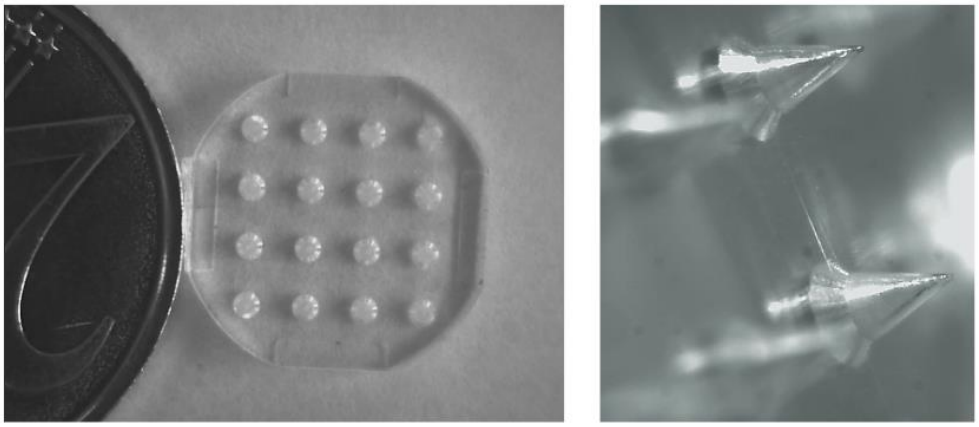

Figure 4.16 A 16 hollow microneedle array moulded in highly biocompatible polymeric material [88].

To prevent the phenomenon called the "bed of nails" effect which, due to the elastic response of skin, may prevent correct microneedles insertion, a proof-of-concept microneedle array (Fig 4.16) has been designed and optimized taking into account mechanical resistance and fluid flow [89].

The challenge for designing and fabricating hollow polymer microneedle systems often resides in the fact that they should be practical in a wide range of applications and they must be optimized in terms of mechanics and fluid dynamics, as well as being cost-competitive with traditional hypodermic injections. Volume of injection, injection time, needle resistance, and, most of all, production costs are the main problems encountered in designing microneedle solutions.

4.4 Other microneedle devices

4.4.1 Coated microneedles

Microneedles coated with different drug substance are applied to the skin in a technique also referred to as the 'coat and poke' approach. This process involves coating the drug to be delivered around the surface of the microneedle. The drug coating dissolves in the skin fluid and the dissolved drug diffuses through the skin

into the blood capillaries upon inserting the microneedles through the skin [90]. There are different coating methods available such as roll coating, spray coating, and dip coating. Gill and Prausnitz proposed a novel dip coating method suitable for efficient coating at the micron scale in 2006 [90]. Metal and silicon both can be used to fabricate coated microneedles. The dip coating method has also been used in a number of other experiments, for example Jiang used the dip coating method to coat drugs unto metal microneedles to insert into human cadaveric sclera tissue [91].

A commercially developed coated metal microneedle device is the Microflux microneedle patch [92] which comprises an array of 190 or 321 microneedles on a 1 or 2 cm^2 base plate and they are usually 330 or 200 μm long with a thickness of 35 μm and 170 μm (Fig 4.17).

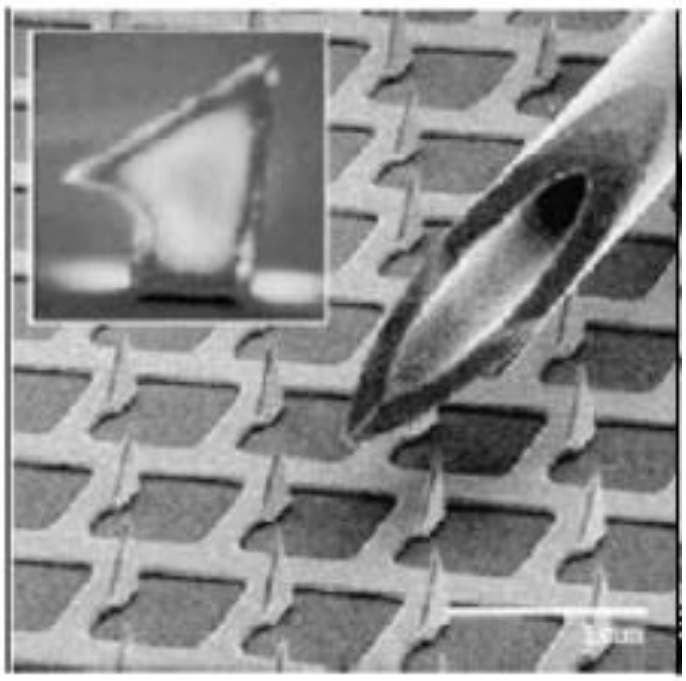

Figure 4.17 An array of metal microneedles of the Macroflux® patch [92]

4.4.2 Self-dissolving microneedles

Dissolving microneedles are made of a soluble/biodegradable material with the drugs encapsulated within the microneedle structure. To produce this type of microneedle, micromolding techniques are used [93]. After the insertion, the needle matrices dissolve in the skin and release their cargoes (Fig 4.18) [93,94,43]. Generally, these types of arrays are made of sugars, carbohydrates or synthetic polymers [93], and have been utilized to deliver a range of different substances including insulin [95,96], low molecular weight heparin [97], ovalbumin [98], adenovirus vector [99], vaccine antigens [99], in addition to low molecular weight drugs. Dissolving microneedles have also been used successfully in combination with other permeation enhancing strategies such as iontophoresis [100].

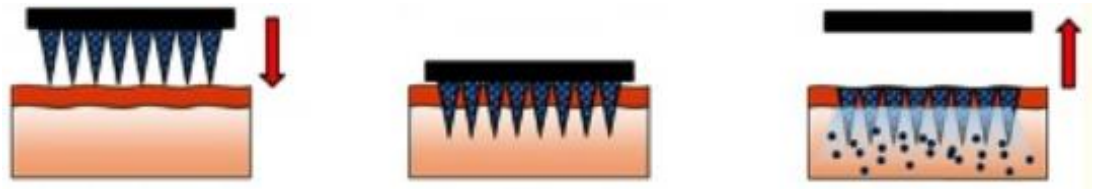

Figure 4.18 Simple schematic of the mechanism of self-dissolving microneedles [102].

Usually high temperature is needed to fabricate polymer microneedles and sometimes encapsulating microneedles use a non-biocompatible polymer. Other studies have designed novel methods for making dissolving microneedles that do not require such high temperatures and allow for the delivery of sensitive molecules such as protein. An example of the dissolving microneedles fabricated by the group Lee et al, 2007 is shown in Fig 4.19 [103].

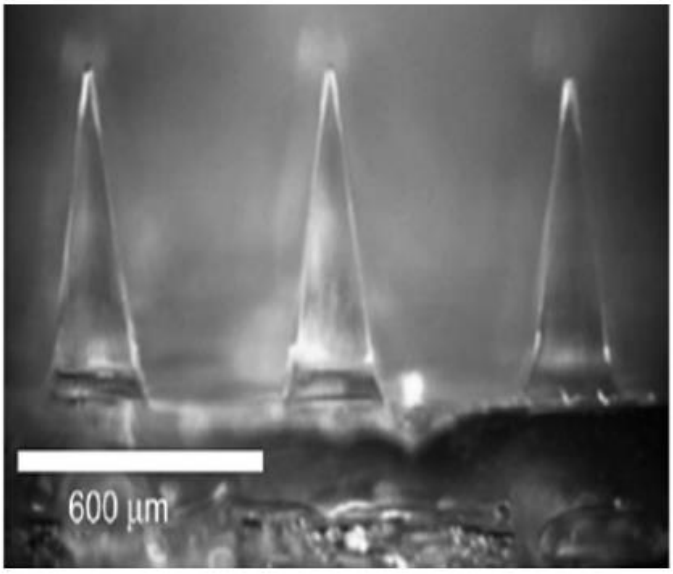

Figure 4.19 Dissolving microneedles containing bovine Serum albumin [103].

4.5 Conclusion

In the first place, as the field has turned out to be progressively developed, more applicable and sufficient trial assessments are being performed, incorporating into vivo preliminaries. Second, the lengths of the needles are becoming longer. Third, the material choice is increasingly broad and polymer needles are gaining more ground.

A compact applicator or a special insertion device is used to achieve skin penetration by several groups. While hollow microneedles have turned out to be more desirable in late years for providing a better alternative in both the delivery quantity and more controllable flow rate, some research groups effectively work and produce different fabrication strategies for solid microneedles.

Chapter 5

Methods and Fabrication of Microneedles

5.1 Chip design for out-of-plane microneedles

The objective of the process is to make a hollow silicon out-of-plane needle-shape array for ISF extraction in an innovative double-side DRIE approach and etch the tip using wet and dry etching processes. We followed some basic logic for our process and they are as follows: defining the bore-hole structure on one side of wafer and pillar structure on the other side of the wafer; afterward, sharpen the pillars into needles using wet and dry etching while exposing the bore-holes at the same time using wet etching. Hence, our process includes three vital steps: lithography, DRIE, wet and dry etching. The backgrounds of these techniques have been introduced and discussed in Chapter 3. In Mukerjee's paper three different designs for the microneedle tip shape were investigated, termed as 'volcano-like', 'micro-hypodermic' and 'snake-fang' design [18]. The relative position of the central bore hole to the shaft of the needle is the only difference visible between them. Three different microneedle shape fashions designed by Mukerjee is shown in Fig 5.1. The silicon walls at the tip seem relatively fragile and ISF extraction can be hindered by the blockage of the centered bore with tissue upon infiltration into the skin in 'volcano-like' design. In comparison with 'volcano-like' design, 'micro-hypodermic' design shows robustness in the microneedles to penetrate skin without any breakage. However, bore hole plugging was one of the problem with this design. Therefore, our out-of-plane microneedle array was designed based on the 'snake-fang' fashion, as shown in Fig 5.2. The enhancement of skin penetration can be obtained by peripheral supporting solid needles. The bore holes were shifted 30 μm from the center of the column.

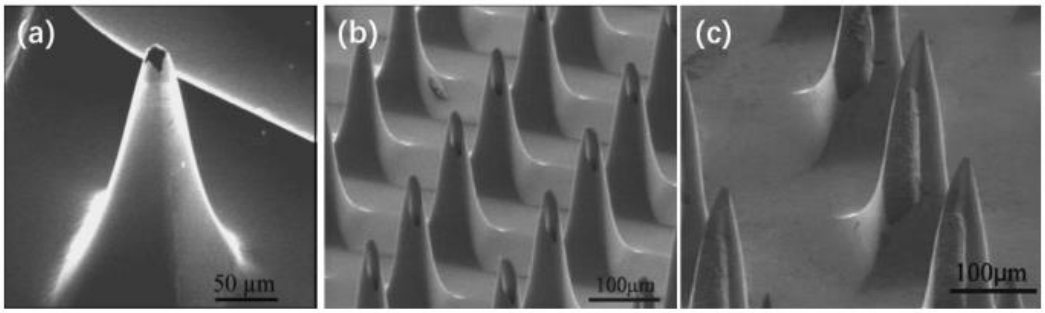

Figure 5.1 SEM pictures of three different designs (a) 'volcano-like', (b) 'micro-hypodermic', and (c)'snake-fang'[18].

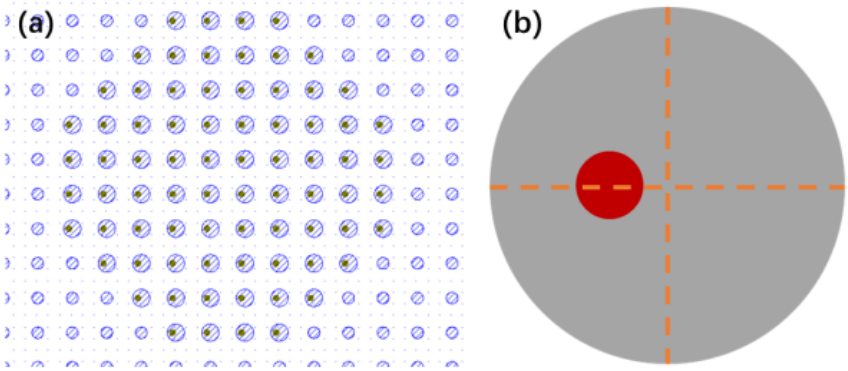

Figure 5.2 The design of hollow microneedle array. (a) 200 µm in diameter pillars and 40 µm in diameter holes with 76 holes per die. (b) 30 µm offset from the central bore hole to the center of the pillar.

5.2 Fabrication process

The proposed fabrication process for hollow out-of-plane silicon microneedles is illustrated in Fig 5.3. With about a thickness of 10 µm, a single layer of AZ 4620 photoresist was spun onto one side of a 4-inch silicon (double-side polished) wafer which we term as the 'backside'. In Fig 5.3(b), to pattern the hole structures that are approximately 30 µm in diameter on the photoresist, a standard photolithography was performed. Using Bosch Process (DRIE) bore holes about 300 µm deep into the backside of the wafer defining a fairly high aspect ratio (HAR) structure (around 1:10) was etched (Fig 5.3 (c)). Note that at this moment the other side of the wafer termed as 'frontside' is still flat. The DRIE process was stopped before the bore-holes were etched through the wafer to it's frontside. As shown in Fig 5.3(d), the frontside pillar

pattern was defined similar to the backside patterning, with the double-sided alignment to the holes on the backside. Again the AZ4620 photoresist was spun and patterned to create cylindrical pillars aligned to the bore-holes. This alignment also enabled accurate patterning of holes such that their centers were offset with the circles that defined needle. This was to address tissue coring within the needle bore during insertion [18]. Using DRIE pillars of approximately 300 μm in height and 200 μm in diameter were then etched (Fig 5.3(e)), maintaining an overlap of 100 μm between the pillars and holes. At this point, the bore-holes were still not exposed on the frontside; essentially they are still buried channels. Afterwards, using a mixed solution of hydrofluoric acid and nitric acid (wet etch), the circular pillars were sharpened into needles and the through wafer holes were fully opened (Fig 5.3(f) and 5.3 (g)). Taking the advantage of the isotropic etching nature of the chemical mixture i.e., the etching rate decreases from the needle tip to the base, this was possible [34]. Holes were exposed on the side wall of the needles creating channels from the needles to the wafer's backside. This final step is a critical and novel process for creating hollow microneedle structures. Dry etch i.e, SF_6/O_2 plasma was also performed to sharpen the needle tip.

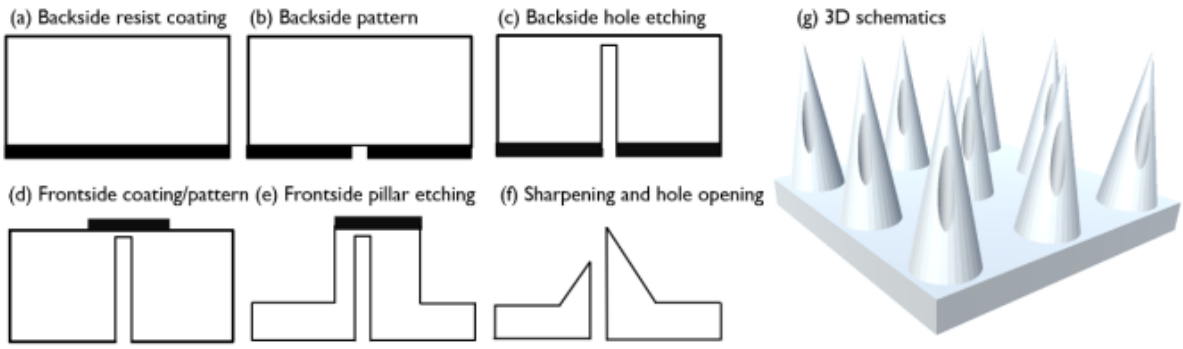

Figure 5.3 Schematic fabrication processing of hollow silicon microneedle arrays. (a) Spin coating on the backside, (b) Standard lithography, (c) DRIE on the backside, (d) Backside alignment lithography, (e) DRIE on the frontside, (f) Wet etch (PR was removed prior to this).

5.2.1 Photolithography

Before performing lithography, standard cleaning procedures for silicon wafers were done. Silicon wafers are cleaned by an HF (1:10) dip and DI water rinse, followed by acetone and isopropanol (IPA) rinsing and blow dry with a N_2 gun. Oxygen plasma treatment can also be done prior to further processing to remove residue on the surface of a silicon wafer. Afterwards, to remove all moisture from the surface of the wafer, a soft bake (prebake) is done on the hot plate at 120°C for 3 minutes. The next step is to spin coat one layer of hexamethyldisilazane (HMDS) which increases the adhesion for the photoresist application after cooling down to room temperature. HMDS is spin coated at 3000 rpm for 30 seconds and it dries completely after the spin coating. The whole process requires about 30 minutes to complete. On the backside of a double-side polished wafer, positive photoresist AZ4620 with a thickness about 10 μm was spun at 2000 rpm for 40 seconds followed by the standard photolithography. Fig 5.4 (a-b) shows the hole and pillar pattern after lithography with HMDS coating prior to photoresist application, and without HMDS treatment, Fig 5.4(c) presents a poor result caused by spin coating photoresist.

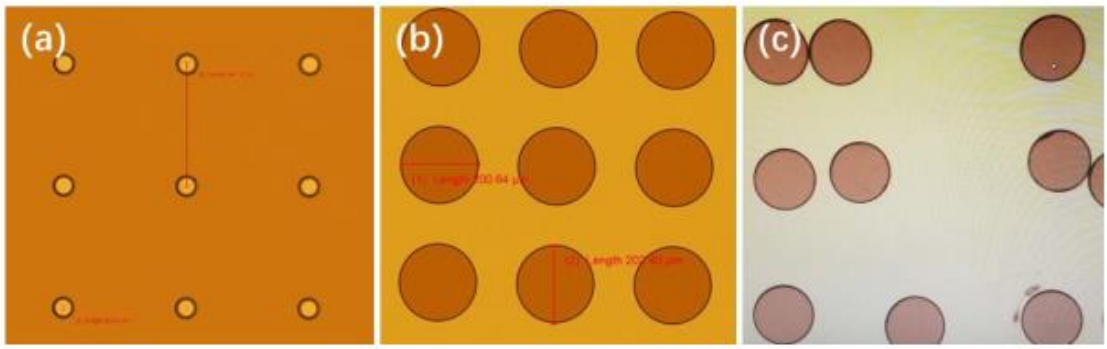

Figure 5.4 Importance of HMDS coating. The pattern is defined after standard lithography and development with and without HMDS coating. HMDS promotes the adhesion to define a better pattern. Structures migration on the wafer is visible if without HMDS application. (a) 30 μm in diameter holes, 300 μm pitch. (b) 200 μm diameter pillars. (c) Structures migrating after photoresist development.

For pillar structures, in the process of lithography, diameter with various sizes of pillars has been designed as shown in Fig 5.5.

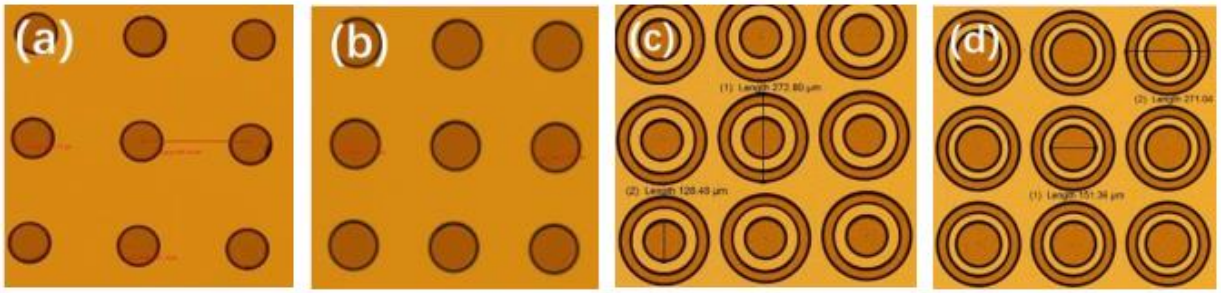

Figure 5.5 Pillars with different diameters. (a) 100 μm in diameter pillars. (b) 150 μm in diameter pillars. (c) 130 μm ID 270 μm OD. (d) 150 μm ID 270 μm OD

The key step of the lithography process is the backside alignment which is to precisely placing the holes with different offsets relative to the center of the pillars. A detail on the alignment process is illustrated in Fig 5.6. Before the loading of the sample, the picture of mask aligner is taken as shown in Fig 5.6 (a), and then in Fig 5.6 (b), aligning the marks accurately is shown.

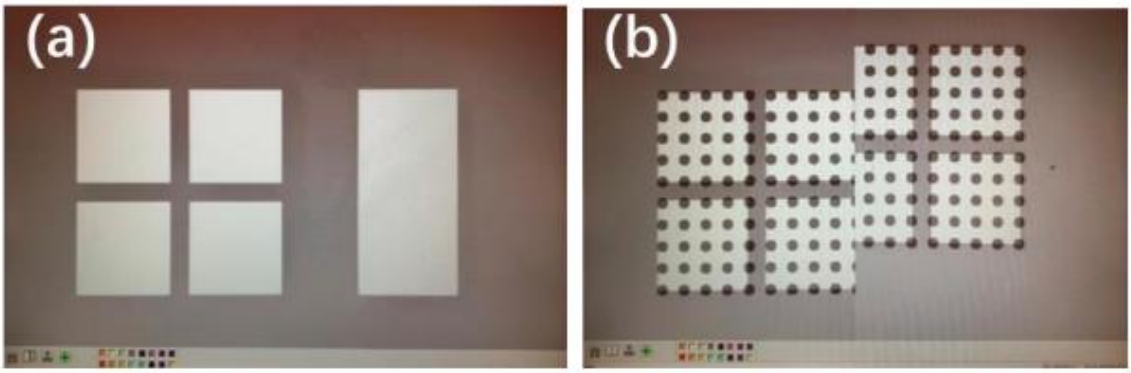

Figure 5.6 Backside alignment process in Karl SUSS MA6. (a) only the captured pattern. (b) By rotating X, Y, Z knobs, align the marks accurately.

5.2.2 DRIE

There are two main technologies for high-rate DRIE: Cryogenic and Bosch-based DRIE [49]. But for production method, only the Bosch process is the vastly recognized [64]. Photoresist or other mask crack under extreme cold condition is the most essential limitation of cryo-DRIE. Another associated issue is that the by-products have a tendency of depositing on the nearest cold surface such as the substrate and electrode [104-106]. There are many applications of DRIE but the major goals are usually in producing trenches or other features of very high aspect ratio [107].

5.2.2.1 DRIE on the backside

In our research, the standard Bosch process recipe was modified and developed at the Quantum NanoFab at University of Waterloo for both our pillar and hole etching to achieve a high aspect ratio features. The etch rate is around 400 nm/cycle where each cycle is 12 seconds and uniformity is approximately 2%. Our target is to obtain around 350 μm deep holes 30 μm in diameter and pillars with approximately 300 μm high and 100 μm in diameter. In our initial experiments, Bosch process was exploited with 300 cycles to produce 110 μm deep holes with a vertical profile, but the diameter got enlarged from 30 μm to 50 μm. In Fig 5.7 (a), the cross-section view after 300 cycles of Bosch processing is shown and in Fig 5.7(b) the change in the diameter after DRIE is clearly visible.

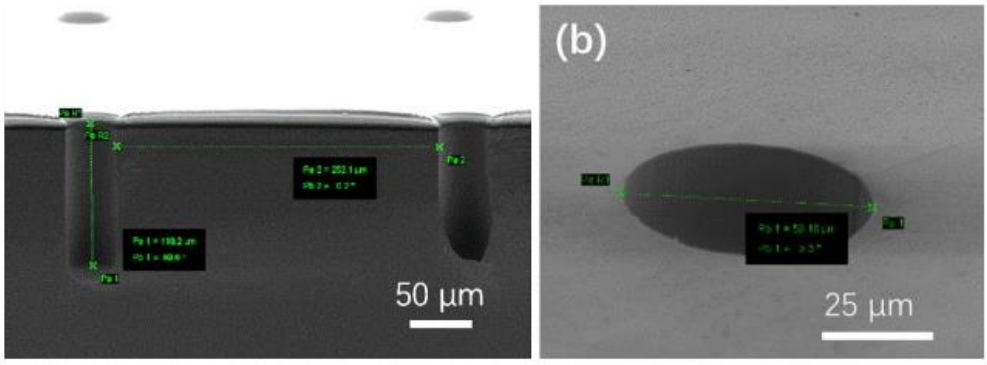

Figure 5.7 SEM results after 300 cycles of Bosch processing. (a) cross-section view. (b) top view at an angle 70°.

Later, additional 1500 cycles were done on the abovementioned samples. To create the holes to a depth of 400 μm, DRIE process of approximately 6 more hours were performed. A significant overcut was observed and the diameter was enlarged to 126 μm. Fig 5.8 shows the results after the total 1800 cycles.

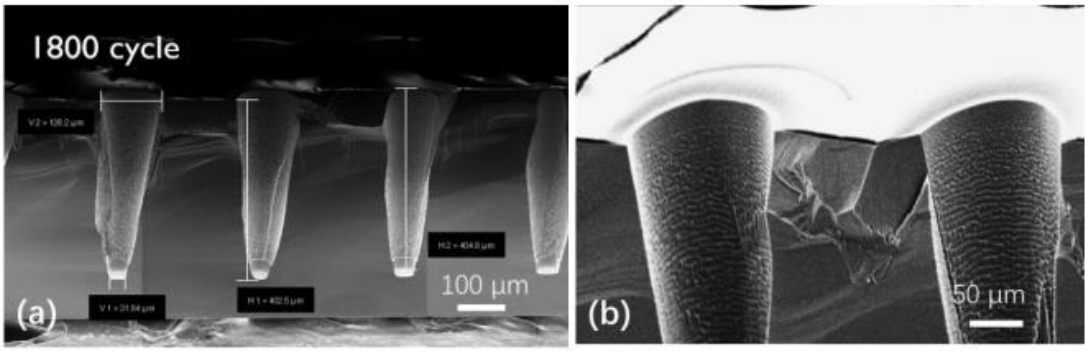

Figure 5.8 The SEM picture after 1800 cycles of Bosch processing. (a) A cross-section view. (b) A zoomed-in view [108].

As shown in Fig 5.8, to form vertically deep holes 30 μm in diameter, profile and the diameter should be more efficiently controlled to form vertically deep holes 30 μm in diameter. Aspect ratio dependent etching (ARDE) is widely reported for deep silicon etching. An example of ARDE of trenches in varying widths is shown in Fig 5.9(a). Fig 5.9(b) demonstrates the ARDE lag measured as trench depths are normalized to that of a 100-μm-wide trench [108]. The etch rate rapidly decreases with the aspect ratio; over a certain critical point of aspect ratio, the etch rate likely reaches a constant minimal value, all while the etch mask is continually consumed so leading to a lateral etching on the surface. Therefore, both enhancement of photoresist selectivity and optimization of the etching recipe are required to mitigate the consequences of ARDE.

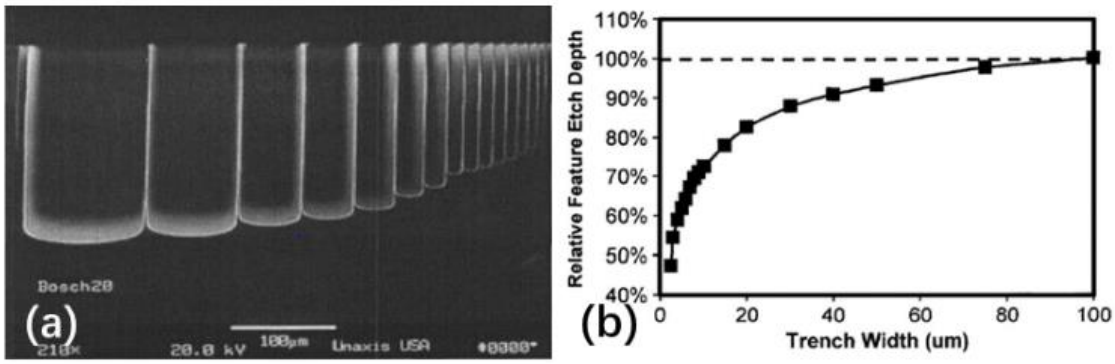

Figure 5.9 (a) ARDE lag revealed in typical TDM plasma etch process. The final etch depths in wider trenches are larger. (b) A plot of trench depth normalized to that of a 100-µm-wide trench. Approximately 50% ARDE lag is presented in a 2.5-µm-wide trench [108].

The depassivation time and bias voltage should be respectively increased to remove the passivation polymer at the bottom of the holes by enhancing the ion bombardment to etch deeper holes with a vertically straight profile. At the University of Toronto, a DRIE machine which offers a high selectivity of up to 1:200, was used to optimize the recipe. In Fig 5.10 (a) the SEM result after etching with different optimized recipes is shown. By increasing the RF power, ramping the process pressure, and altering the length of Argon (Ar) bombardment time, we are able to produce holes approximately 310 µm deep and 30 µm in diameter which is shown in Fig 5.10 (b); a top view of the holes after DRIE is illustrated in Fig 5.10 (c). There was no change in the diameter and it remained at 30 µm. Therefore, holes with approximately 310 µm deep and 30 µm in diameter can be obtained by an optimized recipe, consisting of increased RF power followed by a high aspect ratio etching recipe. Only 1 hour is needed for the whole recipe. Fig 5.10 [I] the result with an original Bosch recipe. A 214 µm deep hole with a critically vertical profile. By ramping the RF power from 100W to 120W, 243 µm deep holes can be achieved [II]. By adjusting Ar time from 700 ms to 800 ms, deeper holes with a 266 µm depth can be fabricated [III]. The best recipe is 500 cycles with 120W power optimized recipe followed by a high aspect ratio recipe for 278 cycles [IV].

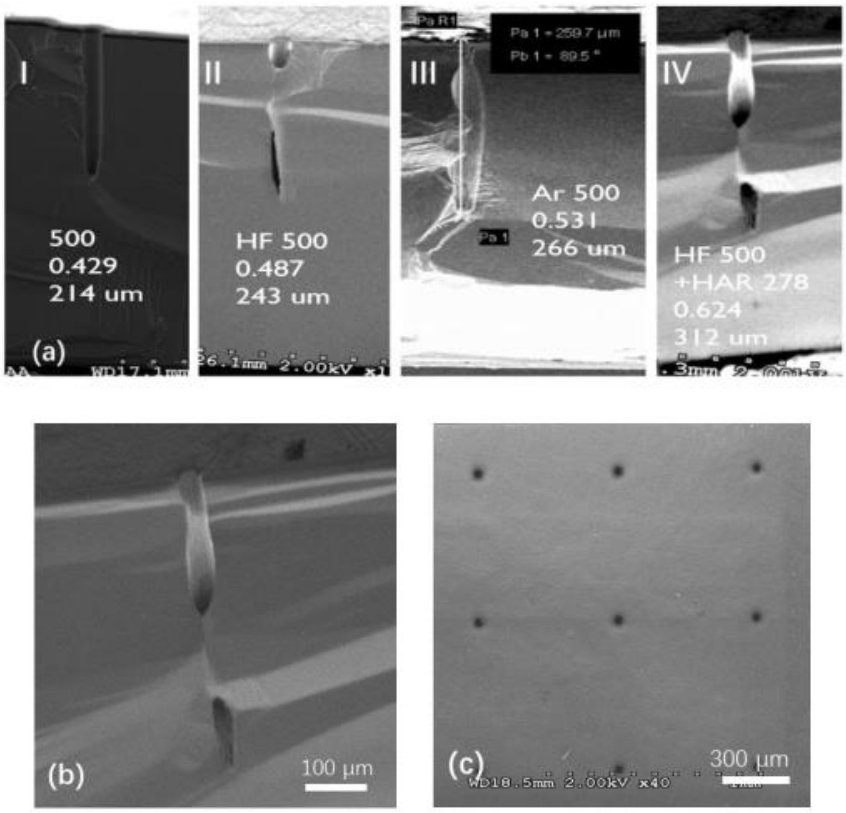

Figure 5.10(a) From left to right, SEM results are shown after 500 cycles etching. (b) a zoomed-in view of the hole. (c) a top view of the holes.

5.2.2.2 DRIE on the frontside

On the contrary, more reliability is observed of DRIE on the frontside; due to low aspect ratio dependency, fabricating pillars approximately 330 µm tall, 200 µm in diameter was possible.

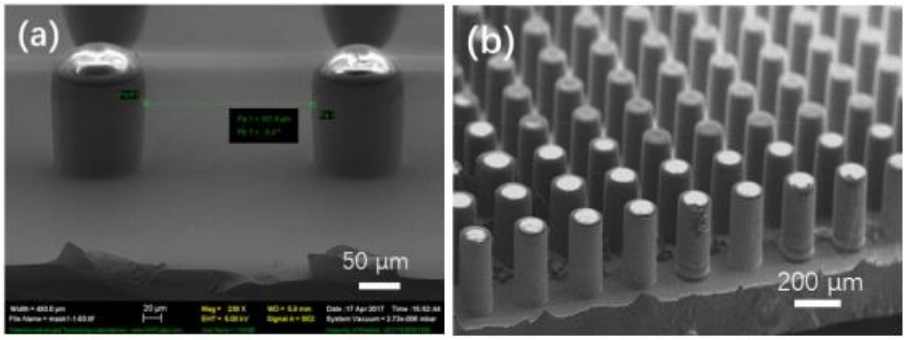

Figure 5.11 SEM pictures after Bosch process etching. (a) 300 cycles. The pillar is ~100 µm tall and 100 µm in diameter. (b) 900 cycles. The pillar is ~330 µm tall and 150 µm in diameter.

To define a hollow needle structure, the combination of holes and pillars is the key step as we mentioned earlier in lithography paragraph (Fig 5.5). The perfect well-aligned structure is formed on the backside via alignment lithography. In Fig 5.12, integration of holes and pillars after double-sided etching is shown. Another design is shown in Fig 5.13 where solid pillars are positioned between hollow pillars to enhance chip robustness and strength when the pillars are subsequently sharpened into needles and inserted into skin.

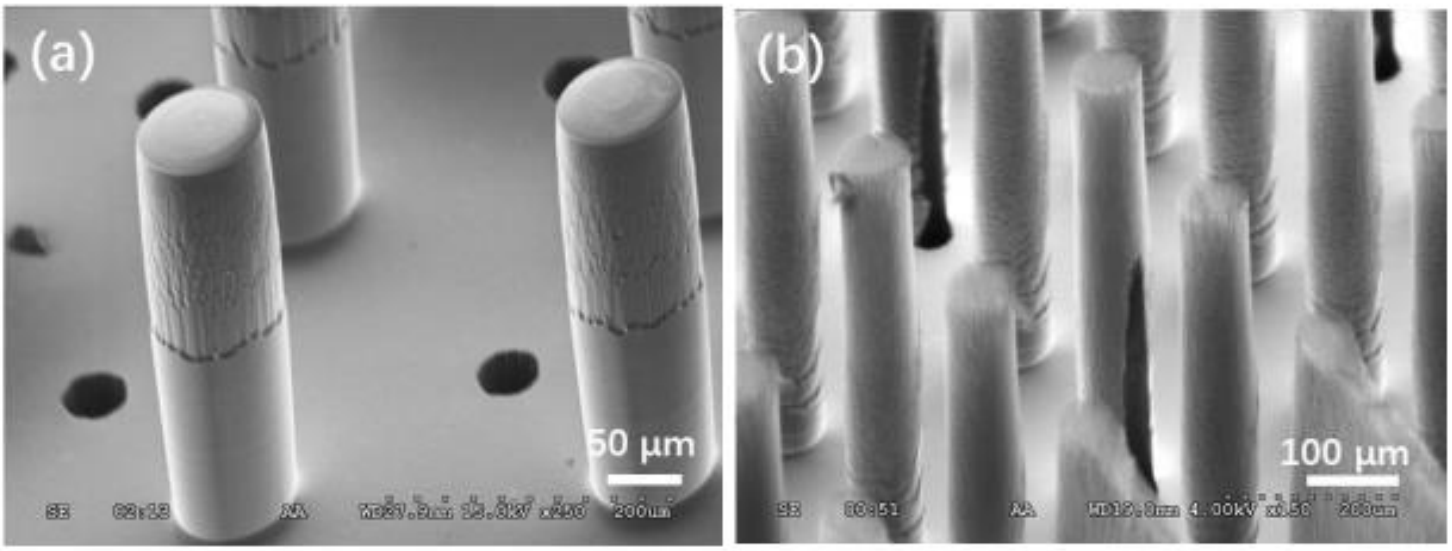

(a) (b)

Figure 5.12 The integration of holes and pillars. (a) misalignment between pillars ~80 µm in diameter and holes with 40 µm in diameter; (b) pillars well-aligned to bore holes. After the DRIE process, bore holes are exposed at the base of columns.

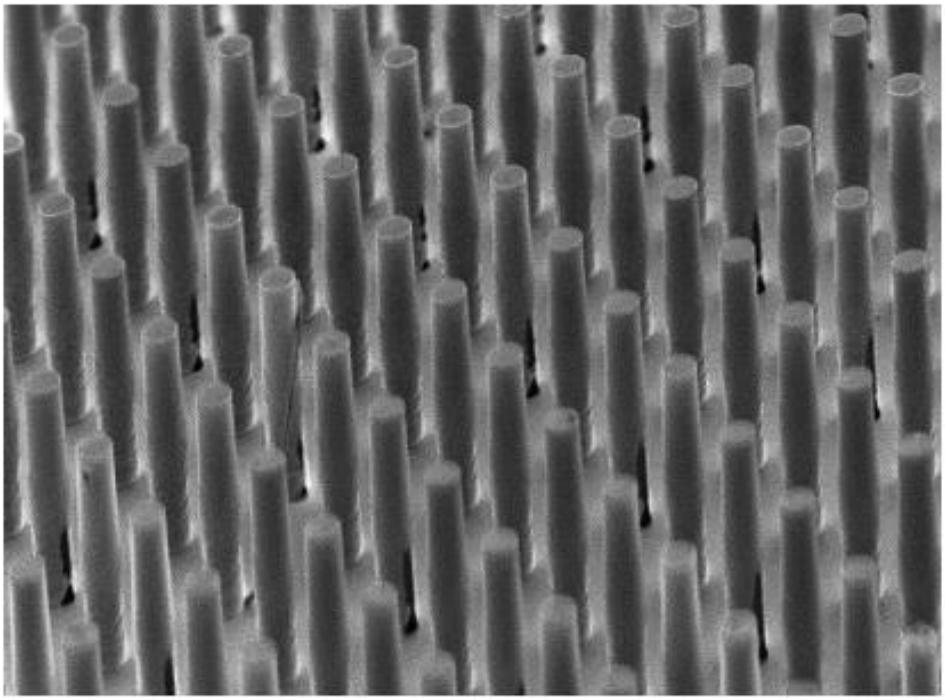

Figure 5.13 An array of hollow pillar structure. 300 μm is the center to center spacing. For ISF collection, 50% of the needles have bored holes, and the other half are solid to distribute the pressure in this particular design.

5.2.3 Wet etch to sharpen the needle

5.2.3.1 Solid microneedles

In our work, to sharpen up the silicon pillar top to form a needle shape, a static wet etching involving a solution of HF (49%)–HNO3 (69%) mixed at a ratio of 1:19 by volume was set up. At the beginning, wet etching tests were done on solid pillars to obtain solid silicon needles. In Fig 5.14, pillars with 200 μm high and 100 μm in diameter is shown after acetone, IPA, photoresist stripper and oxygen plasma treatments were performed to remove photoresist on their tops.

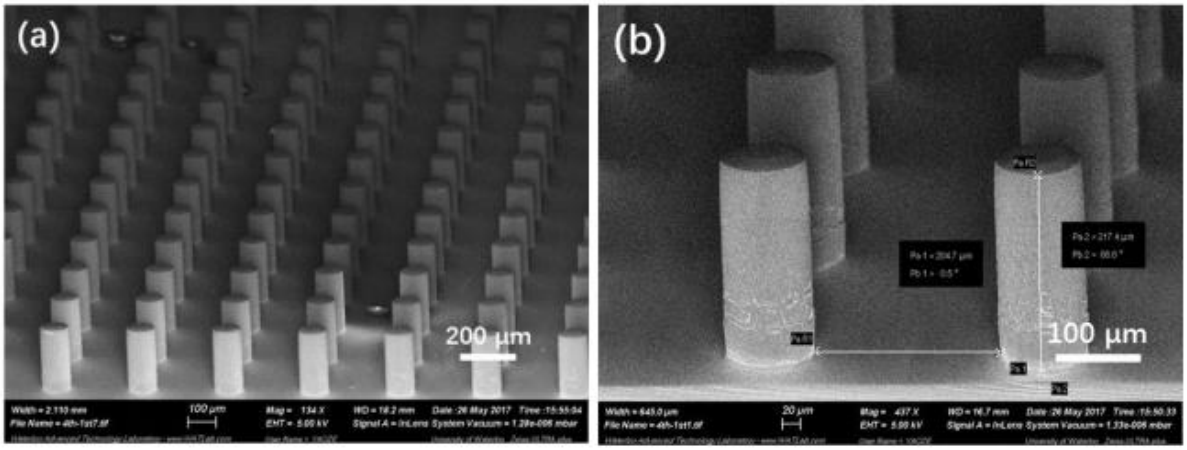

Figure 5.14 The SEM results of pillars after DRIE process. (a) Solid pillar array. (b) pillars with a zoomed-in view.

After 20 minutes of wet etching, Fig 5.15 shows the SEM results where the tip diameter is approximately 60 µm while the base was measured to be approximately 90 µm in diameter. The pillar height is approximately 190 µm. We can conclude that the vertical shrinkage is much less than the lateral tip shrinkage while the etching rate decreases gradually from the needle tip to the base with this experiment.

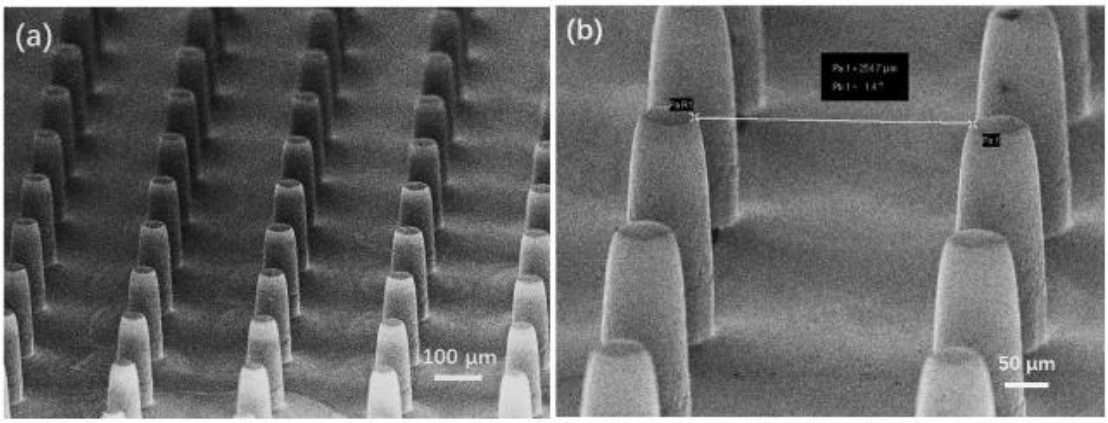

Figure 5.15 SEM images exhibit the blunt cone-shaped pillars. (a) high uniformity of the wet etch; (b) zoomed-in view of the slightly sharped pillar tops.

After that, another additional 20 minutes of wet etching was performed subsequently to make the top of the pillars sharper. SEM images of a very sharp solid microneedles array are shown in Fig 5.16. Upon performing this additional 20 minutes wet etching, the height of the pillar decreased from 200 μm to 150 μm, and concurrently the diameter at the base decreased from 100 μm to 70 μm while the dramatically decreasing of the tip radius to less than 5 μm is observed.

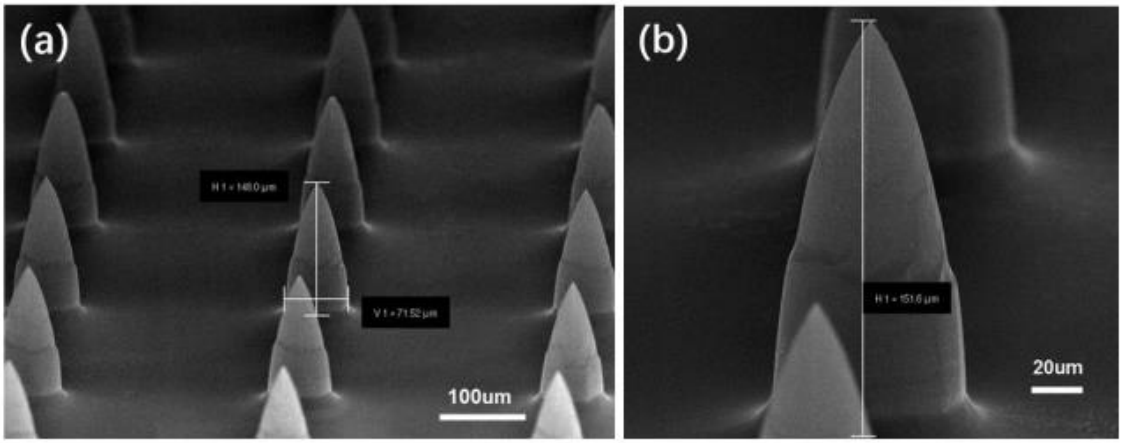

Figure 5.16 SEM images after 20 minutes more wet etching. (a) high uniformity of a solid silicon microneedles array, and (b) an individual sharp needle in a zoomed-in view.

If wet etching is performed for an excessive amount of time, over-etching will be present. Two types of over-etching are illustrated in the SEM images in Fig 5.17. Approximately 20 μm or in some cases less than 10 μm is decreased in the height of needles.

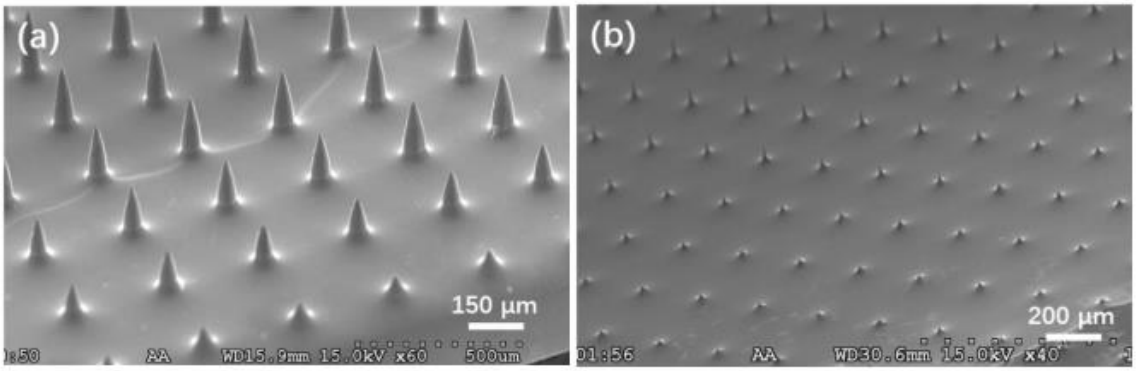

Figure 5.17 SEM image showing the shape after over-etching.

5.2.3.1 Hollow microneedles

After producing sharp solid microneedle array successfully, the next step was to obtain the hollow structure combining holes with needles. With different offsets relative to the center of the pillars, several hollow shapes can be achieved and 'micro-hypodermic' and 'snake-fang' fashions were produced in our experiments (Fig 5.18).

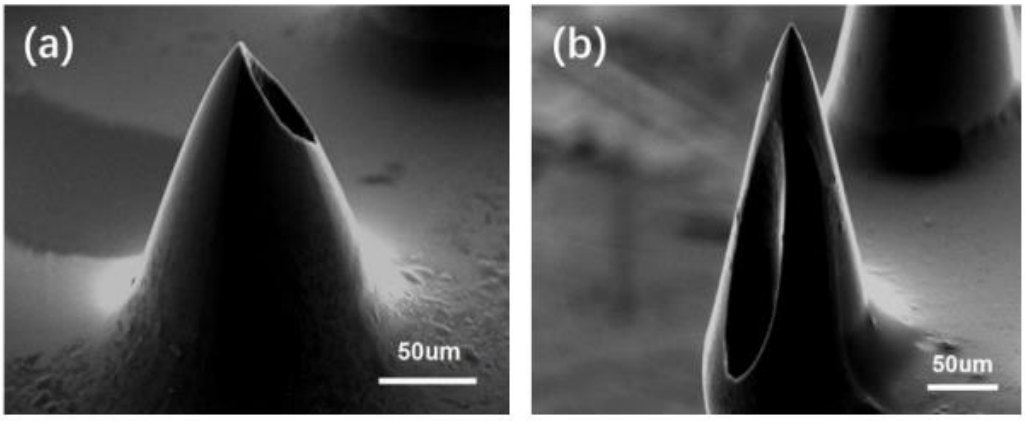

Figure 5.18 SEM images of two different hole offsets for producing the hollow Si microneedles. (a) the 'micro-hypodermic', and (b) 'snake-fang' fashions of microneedle design.

While the bore hole in the 'micro-hypodermic' needle design is extended within the side of the needle, the potential of coring skin during ISF extraction may be present [18]. Therefore, an array of the 'snake-fang' design was fabricated. With different needle base diameters, Fig 5.19 (a-d) shows the 'snake-fang' hollow silicon microneedle array. Figure (e- f) exhibit a solid-hollow microneedle array and a needle height of approximately 300 μm, larger than that of Fig 5.19 (a)-(d).

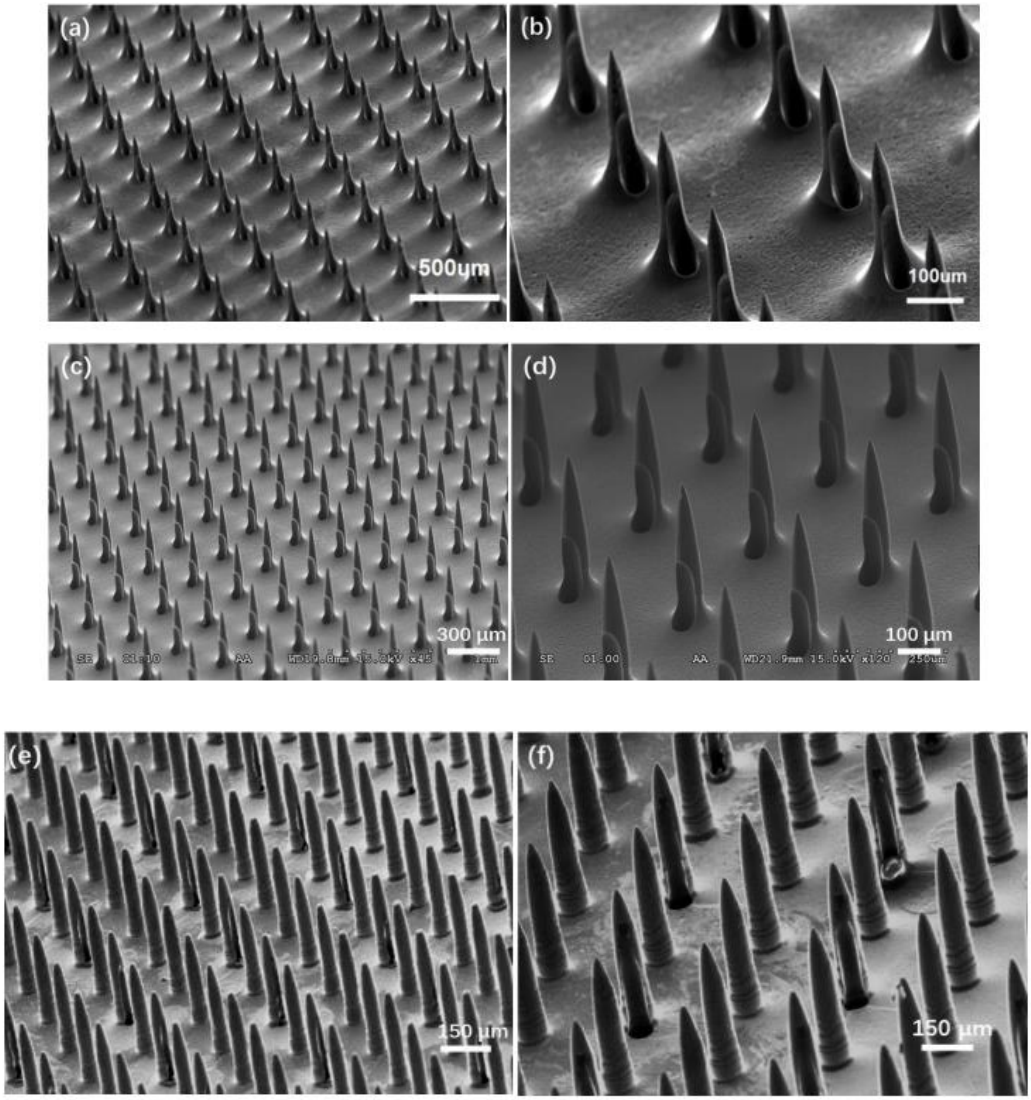

Figure 5.19 SEM images: (a-d) with different base diameter, the hollow silicon microneedle arrays (a) 200 μm high and 100 μm in diameter at the base; (b) a zoom-in view of image (a); (c) height is 200 μm and the base diameter is 60 μm; (d) a zoom-in view of image (c); (e-f) a solid-hollow silicon microneedle array: (e)For ISF collection, 50% of the needles have bored

holes, and the other half are solid to distribute the pressure upon skin insertion; (f) 300 μm high and 80 μm in diameter microneedles in a zoomed in view.

5.2.4 Dry etch to sharpen the needle

As we mentioned before, for the fabrication of micromechanical devices, dry anisotropic etching of silicon is an important technology. Due to its non-dependency on the crystal planes unlike wet etching e.g., KOH solutions, dry etch is performed in many cases.

In our research, plasma etching was considered to minimize the vertical height loss for making taller needles. SF_6 DRIE etching (isotropic) was performed at Quantum NanoFab at University of Waterloo (with the SF_6 flow rate of 160 sccm and chamber pressure of 25 mTorr. The ICP power was kept at 1500 W with a 13.56 MHz frequency for both deposition and etching cycles; the RF bias power was kept at 20 W with a DC bias of 20 V for etching). In Fig 5.20 (a), an array of pillars with height of 300 μm aligned to holes of approximately 80 μm is shown. After performing 10 minutes of SF_6 dry etching on the above sample, the top of the pillar becomes sharper (2 μm/ min etching rate at the pillar bottom and base) and is shown in Fig 5.20 (b).

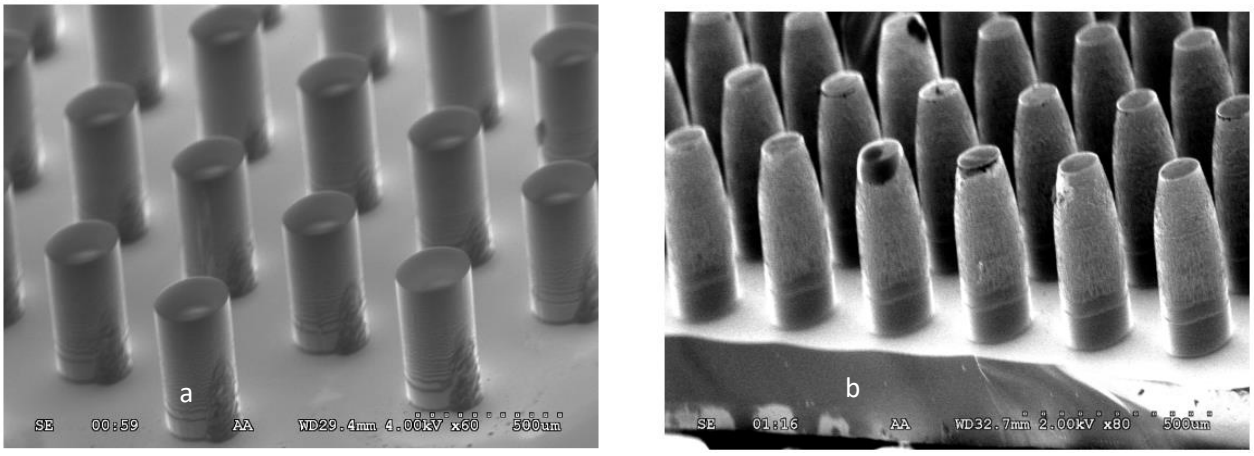

Figure 5.20 An array of pillars with 300 μm high. (a) before dry etching. (c) after 10 minutes of dry etching.

Another 10 minutes of dry etching is performed to the above sample and the top of the pillars got more spiked as needed. But a damage on the top of the pillars is noticed

due to the SF_6 ion bombardment. Fig 5.21 shows the SEM results of the more sharpened needle tip (a) and some top part removal due to the ion bombardment (b). A great uniformity is observed in this process.

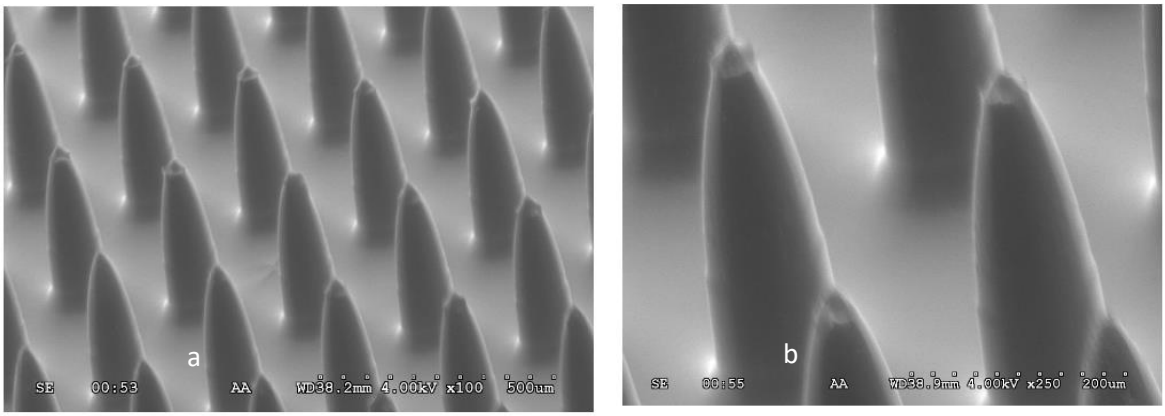

Figure 5.21 SEM images after total 20 minutes of SF_6 dry etch. (a) the tip of the pillars was sharpened more. (b) a zoomed-in view to show the top part removal due to SF_6 ion bombardment.

Another SEM results show the shrinkage of the pillar part on the top after 30 minutes of SF_6 dry etching process in Fig 5.22. Some of the pillars on the edge was broken due to ion bombardment.

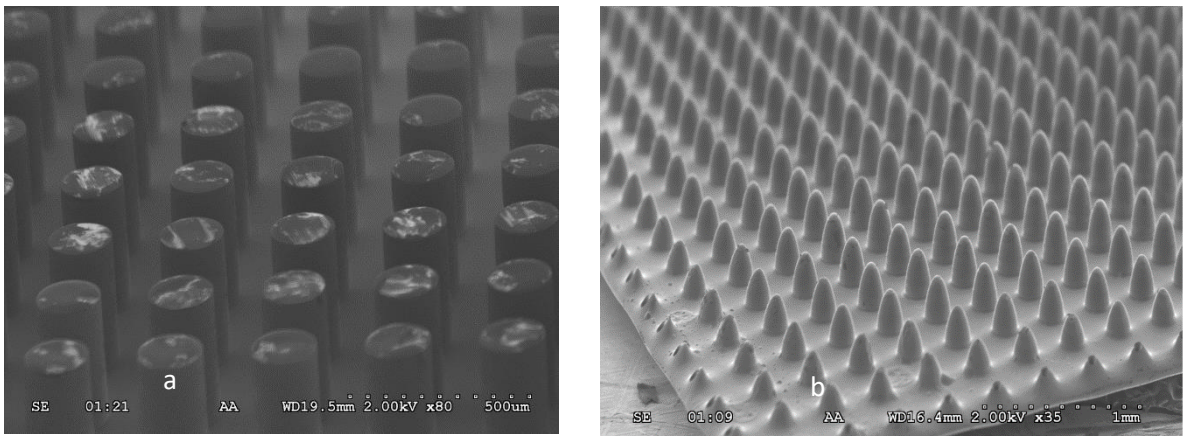

Figure 5.22 (a) an array of 200 μm high pillars before SF6 plasma etching. (b) after 30 minutes of SF_6 plasma etching.

These are some interesting facts to consider while making sharper microneedles using SF_6 plasma etching. Good results with respect to uniformity and reproducibility have been obtained using this dry etching process. Elimination of handling dangerous acids

and solvents, better process control and easy automation are some of the major advantages of using this technique to make the needle sharper. Further research is needed to improve the process and to achieve sharper needles without the damage.

5.3 Chip design for in-plane microneedles

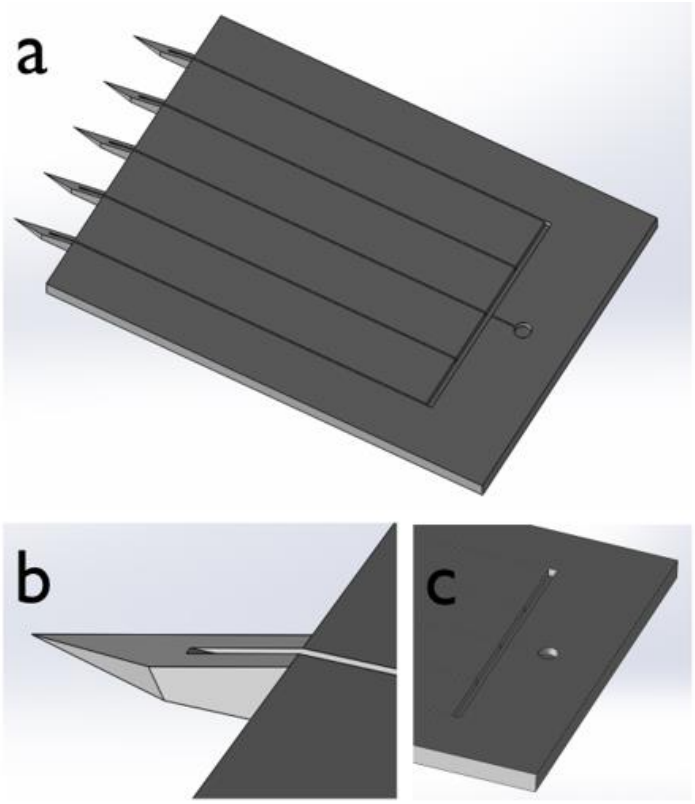

Figure 5.23 Schematic diagram of (a) the in-plane microneedle chip and the zoom-in views of (b) needle tip and (c) microfluidic network and the reservoir.

In Fig 5.23, the schematics of a silicon in-plane microneedle with open capillary microfluidic channels is shown. The needle with length of approximately 2 mm enables the penetration into elastic body tissues (e.g., skin) with sufficient insertion depth (Fig 5.24). Whereas the wedge squared shape of the needles (Fig 5.24a) can be fabricated with moderately simple processing, the large tip requires significant force to break the skin.

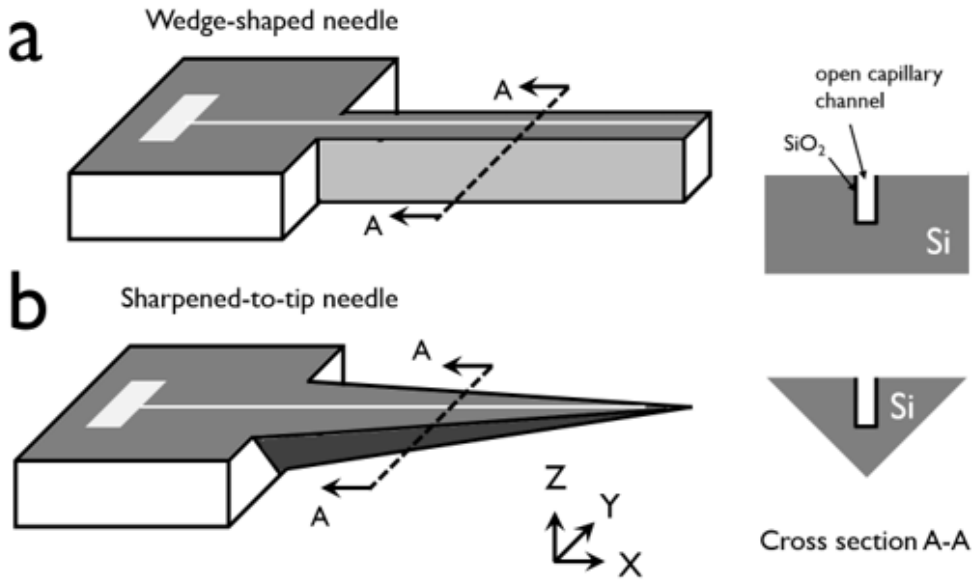

Figure 5.24 Schematic diagram of a silicon in-plane microneedles with open capillary microfluidic channels (a) wedge-shaped needles and (b) sharpened-to-tip needles.

Silicon wafers with the thickness of 500 μm were used for this work. With a pitch of 2 mm, five microneedle arrays with 2 mm long needle shaft and base of 500 μm were integrated in each device. In the microneedle shaft the open trenches are embedded through which fluid will flow and enter the microfluidic channel network and end up in a reservoir on the backside of the device which is the opposite to the needle tips. Channel with a certain aspect ratio of depth to width is important for capillary drawing and it shows in the open channel design. Because of some processing constraints such that the trench width is designed as 10 μm, the trench depth is limited to 100 μm. Considering the length of few centimeters, the trench structure with very high aspect ratio may experience channel interruption triggered by some practical processing issues i.e, the coating of the resist, etching steps etc. To lessen the processing defects, the layout of multi-channels was designed. It also enables the elongating of the liquid-air meniscus of the capillary filling of the channels within the microfluidic network, hence making possible to recover more fluids.

5.4 Fabrication process

5.4.1 DRIE

A silicon wafer with the <100> crystalline orientation was used to fabricate the microneedle pattern using standard photolithography techniques. First, the Si wafers are cleaned by immersion into hydrofluoric acid (HF: deionized water = 1:10) for 30 seconds, followed by a solvent and deionized (DI) water rinsing, and a nitrogen blow drying. Immediately afterward, an adhesion promoter hexamethyldisilazane (HMDS) is spin-coated at 500 rpm for 30 seconds. Then to get a thickness of approximately 11 μm, positive photoresist AZ 4620 is spin-coated at 2000 rpm for 40 seconds, followed by a pre-baking at 90°C for 5 minutes. To extend long etching through the silicon wafer, the photoresist coating can be repeated once again to make a 22 μm thick bi-layered photoresist (termed as double layered resist). For the photoresist erosion under high bias power, ultrathick photoresist is required. The ultraviolet (UV) light exposure was carried out with a Heidelberg MLA150 maskless aligner operating at a dosage of 1000 mJ/cm^2 for the single-layered resist and 1800 mJ/cm^2 for the double-layered resist. Then the exposed sample is immersed into a developer solution (AZ 400k 4:1 developer).

In our experiment, silicon samples were anisotropically etched in an Oxford Instruments PlasmaLab 100 inductively coupled plasma reactive ion etcher (ICP-RIE) 380. The Si sample was attached on a 4 inch silicon carrier wafer using Fomblin oil as an thermally conductive adhesive. The deposition sub-cycle is 5 seconds long, with the C_4F_8 flow rate of 160 sccm (standard cubic centimeter per minute) and chamber pressure of 20 mTorr; the etching sub-cycle is 7 seconds long, with the SF_6 flow rate of 160 sccm and chamber pressure of 25 mTorr. The ICP power was kept at 1500 W with a 13.56 MHz frequency for both deposition and etching cycles; the RF bias power was kept at 20 W with a DC bias of 20 V for etching and at 5 W with a DC bias of 0 V for deposition. Moreover, the silicon etching processing can be modified as an isotropic etching to facilitate the needle sharpening process. This experiment utilized a continuous SF_6 gas with the flow rate of 160 sccm and chamber pressure of 15 mTorr; the ICP power was kept at 1000 W with a 13.56 MHz frequency and RF bias power

was kept at 20 W with a DC bias of 150 V (± 10 V). Note that in all the above mentioned plasma etching process the continuous helium cooling was utilized to ensure the wafer temperature kept at 15 ^{o}C. The major process steps are illustrated schematically in Fig.5.25. In this study, the scanning electron microscopy (SEM) inspection was carried out using a Hitachi S-3000N SEM and Zeiss LEO 1530 FESEM.

Aspect ratio dependent etching (ARDE) is widely reported for the deep silicon etching [108-110]. Aspect-ratio refers to the proportions of the depth and width of an etched object into the silicon wafer. The etching rate rapidly decreases with the aspect ratio of the etched structures. The mechanism probably lies that the ion flux down to the bottom of the structure decreased as the aspect-ratio of the structures (i.e., trenches) increases. Trenches with higher aspect ratio probably start to pinch-off at the bottom as a result of insufficient passivation layer removal; over a certain critical point of the aspect ratio, the etching rate would probably reach a constant extremely low value. In the simplest process design, the grove and wedge are patterned and etched at the same time using DRIE; but since the grove is very narrow, it etches much slower than the open area surrounding the wedge as a result of the aspect-ratio dependent etching process, such that when the wedge is fully etched through, the groove is etched only half way as desired [111].

The single-sided simultaneous etching of the needle shaft and open trenches is demonstrated in Fig 5.25 (a-c). First, a custom wafer polished for etching on both sides is spin-coated with photoresist on its backside. Photolithography is then applied to pattern this photoresist, allowing the DRIE process to etch 10 μm wide open trenches through the wafer from the backside (Fig. 4e). The DRIE is halted after the high aspect-ratio trenches are etched (Fig 5.25f); the wafer's front side is still flat at this point. The process is repeated for the frontside (Fig. 5.25g), but rather than trenches, the photoresist is patterned to create needle shaft aligned to overlap with the trenches (Fig 5.25h). Then an "isotropic" (i.e. etching in all directions) wet chemical etching step is

utilized to sharpen the needle shaft structures in the presence of a sacrificial structure (Fig 5.25c) [34]. The isotropic "wet" etching to sharpen silicon structure uses the mixed solution of nitric acid (HNO_3) and hydrofluoric acid (HF), at a volume ratio of 19:1, respectively. This etching chemistry is divided into two steps: first HNO_3 oxidizes silicon into silicon dioxide (SiO_2), then SiO_2 is etched away by HF. It is important that the etch rate of silicon is limited to the rate of oxide removal. If so, HF diffusion to the silicon surface will be the rate-limiting factor, which will result in faster etching of the needle tip. A 30 minutes' acetone soak was performed to clean the sample, following by a 10 min oxygen plasma treatment in a reactive-ion etching system (Phantom II, Trion Technology Inc.) to make the silicon sample hydrophilic.

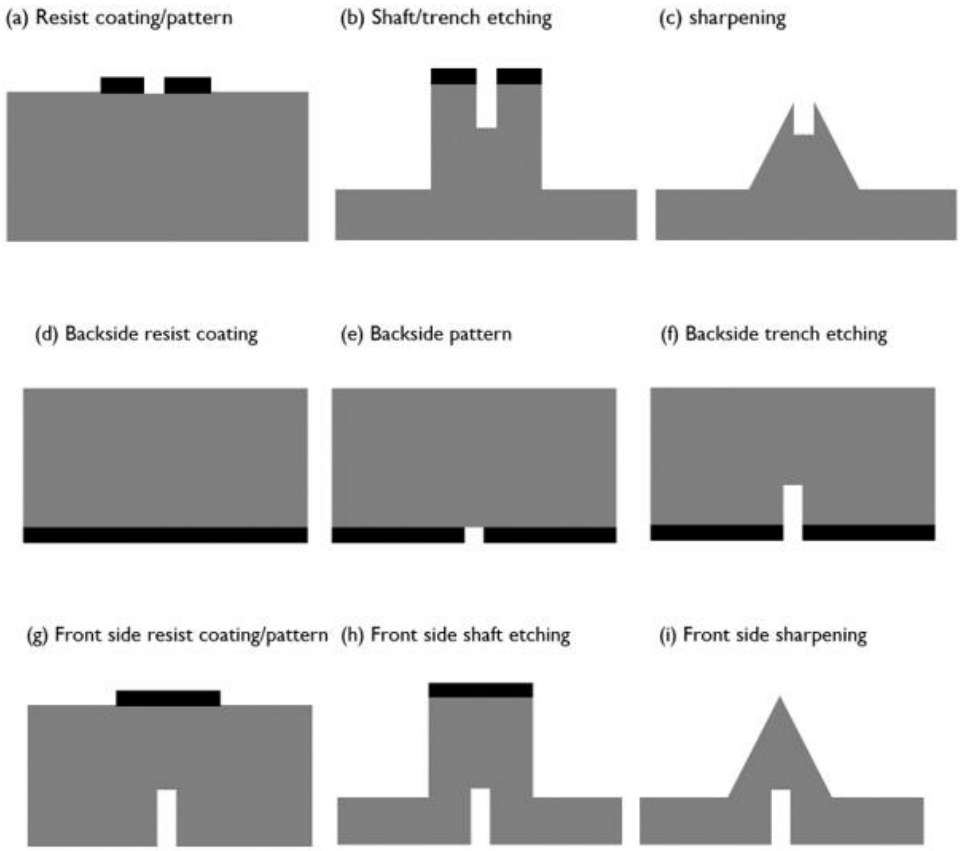

Figure 5.25 Schematic fabrication processing of silicon in-plane microneedle arrays (a-c) single-sided processing and (d-i) double-sided processing along the A-A cross section.

5.5 Results and discussion

Using a standard Bosch process, the needle shaft and open trenches are simultaneously etched. To etch a 200 μm high needle shaft, with a straight and smooth sidewall profile, a 600 cycle of standard Bosch DRIE was performed (Fig 5.25 (a)). The microfluidic network with open trenches was simultaneously etched (Fig 5.25 (b)). A wedge-shaped needle rather than a needle with a pointed distal end was fabricated by DRIE. By immersing in an acetone soak for 30 min, the remaining photoresist was removed and then an oxygen plasma treatment was performed for 10 minutes prior to the isotropic etching process for sharpening. Afterwards, a SF_6 plasma etching was done for 30 min, followed by 60 min of wet etching to sharpen the needle. The etch rate at the top is faster than that at the bottom, resulting in the sharpening of the needle. Note that due to the wet etching, the open trenches were damaged.

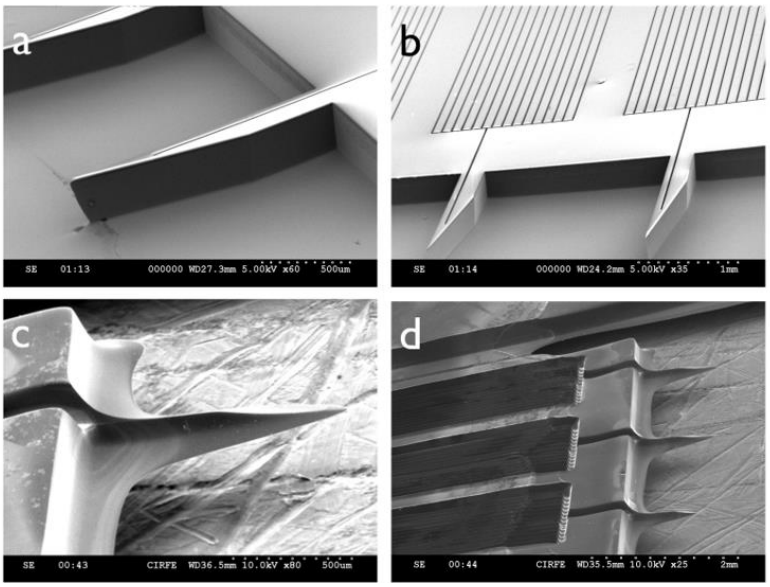

Figure 5.26 SEM images of single-sided processed in-plane microneedles (a-b) before wet etching and (c-d) after wet etching.

Further investigation was done for the etching of the microfluidic network, i.e., trenches and reservoirs (Fig 5.27). The three 10 μm wide trenches in parallel (> 1 cm in length) were patterned and etched by the standard Bosch process, half-way etching for 600 cycles. For the half-way etching, the depth of the trenches (i.e., 160 μm) are

slightly smaller than that (i.e., 250 μm) of the open space between needles. By extending the etching to 1300 cycles, Bosch DRIE etched through wafer at the large space between needle shaft. However, the extended etching makes the narrow trench slightly deeper from 160 μm to 200 μm (Fig 5.26(c)and Fig 5.26(d)). The much slower etch rate within the high aspect ratio trenches is caused by the ARDE. The trenches at the needle tip were found to be deeper than that of the trenches in the silicon.

The reservoir etching also takes advantage of the ARDE to slow down the etching rate at the large reservoir region (i.e., 500 μm × 2000 μm) for avoiding the through wafer etching. The ARDE is activated by utilizing the sacrificial structures, consisting of 20 μm × 100 μm rectangular pillar arrays with a pitch of 20 μm (Fig 5.27(b), became (f) after etching).

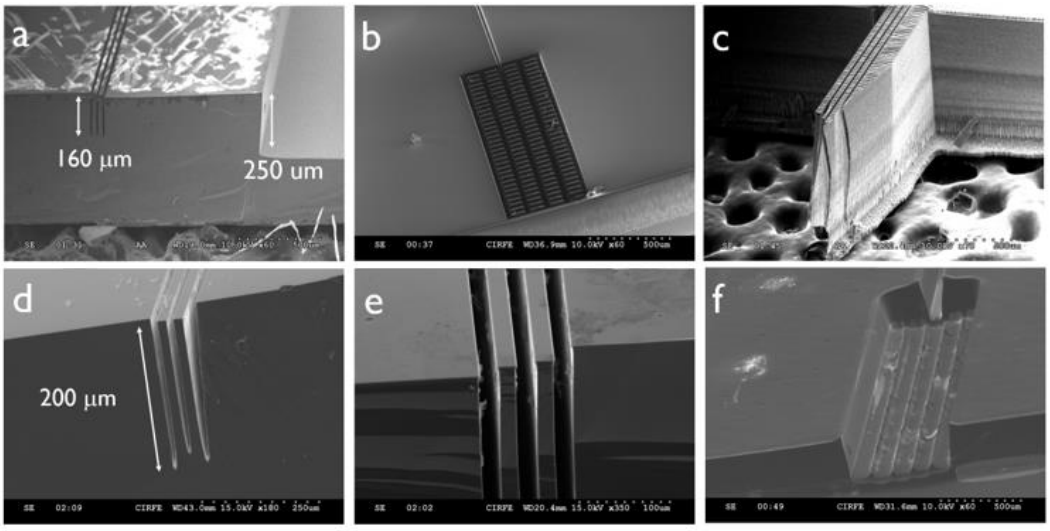

Figure 5.27 SEM images of the microfluidic channels from the single-sided processed microneedles: (a) trench and (b) reservoir from the half-way etching (600 cycles of Bosch processing); trenches and reservoir from the through-wafer etching (1300 cycles of Bosch processing), (d-i) images from different angles.

5.5.1 Wet etching for needle sharpening

Wet etching (mixture of HF and HNO_3) was used to sharpen the needles. In this process, a kapton tape was used to attach the sample onto a clean silicon wafer. By dipping the device in static etchant for 30 min, the wedge-shaped needles were sharpened to a tip, with open trenches being intact (Fig 5.28(a). In Figure 5.28 (b), a zoom-in view of the needle end shows a tip less than 1 μm, smoothly tapering to the base.

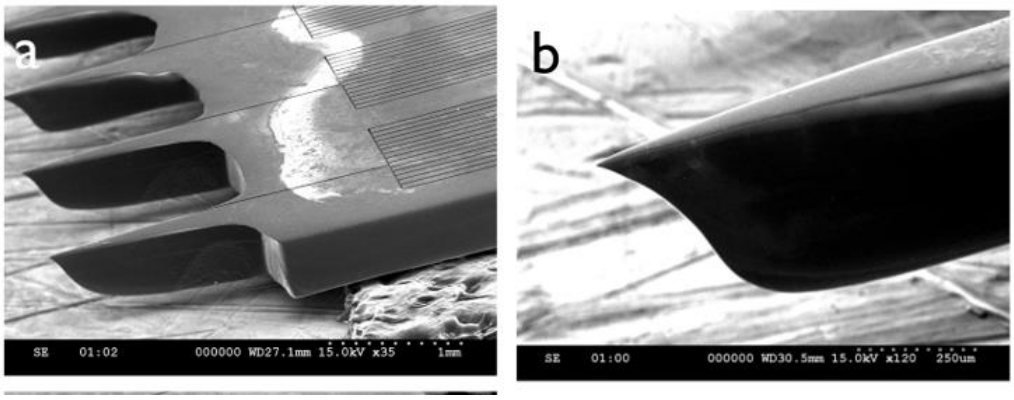

Figure 5.28 SEM images of (a) the sharpened microneedle shaft and (b) a zoom-in view of a needle tip.

Sharpened microneedles are sufficiently robust to penetrate porcine and human skin. The platform enables the delivery of drugs to the target site of interest body tissues, and extraction of interstitial fluid (ISF) and blood in skin.

5.6 In-Vivo tests using hollow out-of-plane microneedles

An integrated system consisting of a microneedle arrays and reservoirs was developed. PDMS was cut out into desired dimensions with a reservoir facing the backside of the microneedle array. By using oxygen plasma cleaning and heating assembly on hotplate, the PDMS reservoir was bonded to the silicon microneedle array.

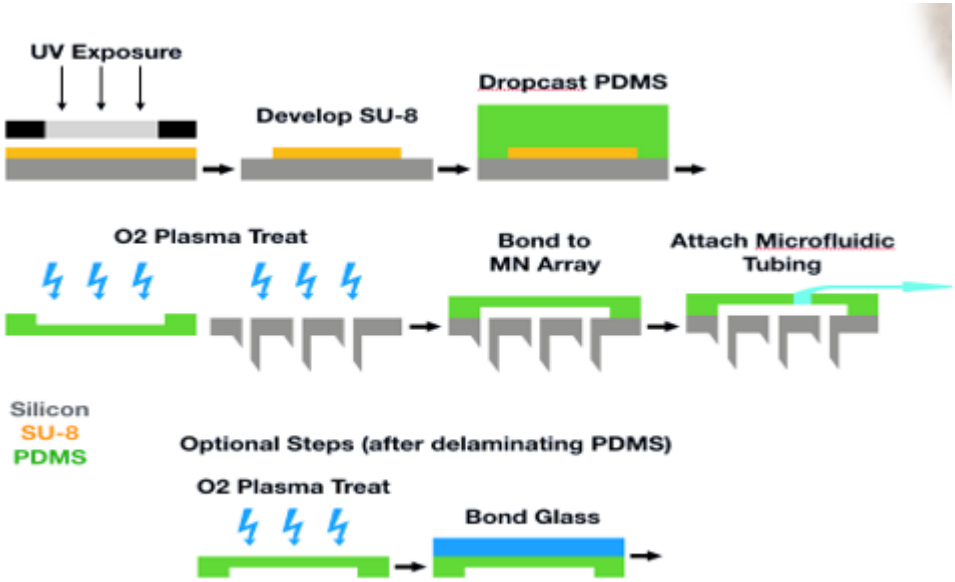

Figure 5.29 A simple schematic fabrication process flow of PDMS extraction apparatus.

Figure 5.30 Fabricated PDMS extraction apparatus.

Extraction tests with silicon hollow out-of-plane microneedles were performed on a living human arm. The tests were done in the following manner: by pushing on the device with thumb pressure on the center of the array and holding it for about 20 minutes, the insertion of the microneedles was successfully performed; a syringe pump was set to withdraw fluid at a predetermined fluid extraction rate for a predetermined total volume immediately afterward; detach microneedle array from the skin by lifting directly outwards once the withdrawal process is complete. Fig 5.31 shows SEM results of the microneedle array before and after extraction tests.

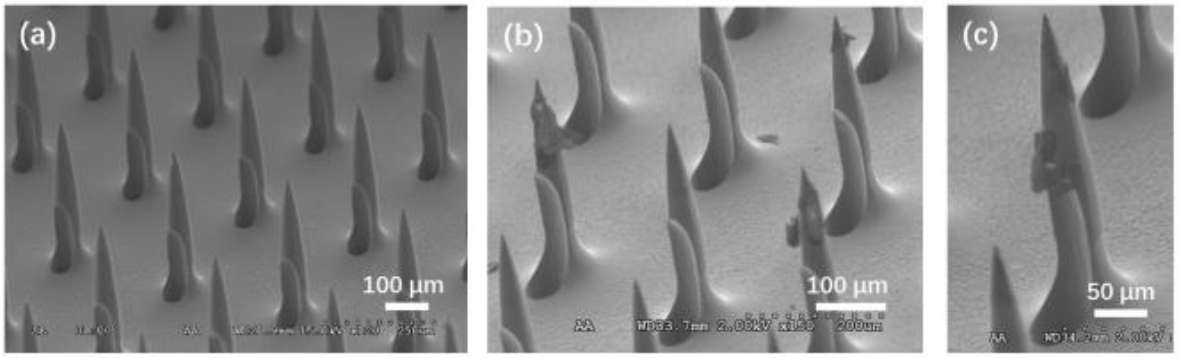

Figure 5.31 An SEM image of the microneedle array before insertion (a). (b-c) The tissue and liquid residual on the needle.

These tests presented above show some promising results. The highly impermeable outer-most layer of skin is penetrated by hollow silicon microneedle which can reach the epidermis layer in which ISF is located and extracted successfully inside the bore hole of the microneedles.

5.7 Conclusion

In today's transdermal drug delivery research and development, microneedles are achieving noteworthy attention. By bypassing the skin's outer layer of stratum corneum microneedles can also access biomarkers such as interstitial fluid (ISF) without interfering with the nerves in the deeper layer of skin which is very useful for painless sampling for various medical diagnosis. In our work, we have successfully fabricated out-of-plane and in-plane microneedles which can penetrate through the skin and extract interstitial fluid (ISF). These microneedle devices can be adapted to extract clinically relevant volumes of interstitial fluid through skin safely in a reproducible manner.

This thesis presents the fabrication process of making out-of-plane and in-plane silicon microneedles robust enough to penetrate through the skin. This work demonstrates a novel double-side DRIE approach with modified recipe for producing hollow out-of-plane silicon microneedle arrays and the fabrication of silicon in-plane microneedles with microfluidic channels using also a novel double-side DRIE. While the out-of-plane silicon microneedles are sharpened by both wet and dry etching, the in-plane microneedles were etched by wet etching process alone.

In our experiments, solid silicon out-of-plane microneedles were first fabricated with the tip radius approximately about less than 5 μm and wet etched on the frontside only. Using double sided polished silicon wafer, patterns of holes and pillars were designed on each side of the wafer and the etching from the both sides were integrated which results in the accomplishment of hollow silicon microneedles with two bore placements and this method was used to fabricate 200 μm and 300 μm high hollow silicon microneedles successfully and were sharpened by both wet etch and SF6 plasma etch process. On the other hand, a standard bosch process was used to make 2 mm long needle shaft with 500 μm base with multiple microfluidic channels in a total dimension of 1.7 cm x 1 cm chip for in-plane Si microneedles. The needle tips

were sharpened by using wet etching process while the microchannels were kept intact.

Fascinating in-vivo tests were executed to extract ISF through skin using the hollow out-of-plane microneedles because such microneedles can only penetrate through the outer layer of skin without hitting the nerve system. In-plane microneedles were also robust and sharp enough to penetrate through the skin and can be used for drug delivery and extraction of biofluids for various purposes.

Finally, comprehensive additional research and studies are necessary to optimize the extraction apparatus and to investigate the safety of these microneedles upon insertion (i.e, microbial infection).

References

[1] Wittekoek, S., 1994. Optical lithography: Present status and continuation below 0.25 μm. Microelectronic Engineering, 23(1-4), pp.43-55.

[2] Mahler, G. and Wawer, R., 1998. Quantum networks: dynamics of open nanostructures. VLSI Design, 8(1-4), pp.191-196.

[3] https://en.wikipedia.org/wiki/Moore%27s_law

[4] https://irds.ieee.org/images/files/pdf/2017/2017IRDS_ES.pdf

[5] Congress, U.S., 1995. Office of technology assessment. Adolescent health, 1.

[6] C. Combs and M. Nichols, "Introduction To Micro/Nano Fabrication," Life Sci., vol. 91, no. 23–24, p. 1140, 2012.

[7] http://www.mtl.kyoto-u.ac.jp/english/laboratory/nanoscopic/nanoscopic.htm

[8] Jalali, H. and Gates, B.D., 2009. Monitoring and Mapping Imperfections in Silane-Based Self-Assembled Monolayers by Chemical Amplification. Langmuir, 25(16), pp.9078-9084.

[9] http://www.mtl.kyoto-u.ac.jp/english/laboratory/nanoscopic/nanoscopic.htm

[10] Paliwal, S., The Study of Nanomaterial and Their Application with Special Reference to Biomedical and Pharma Industry in India.

[11] Rufer, L., Mir, S., Simeu, E. and Domingues, C., 2005. On-chip pseudorandom MEMS testing. Journal of electronic testing, 21(3), pp.233-241.

[12] Madou, M.J., 2011. Manufacturing techniques for microfabrication and nanotechnology (Vol. 2). CRC press.

[13] Maluf, N. and Williams, K., 2004. Introduction to microelectromechanical systems engineering. Artech House.

[14] Judy, J.W., 2000. Biomedical applications of MEMS. In Measurement and Science Technology Conference, Anaheim, CA (pp. 403-414).

[15] Lee, Y.C., Ramadoss, R. and Hoivik, N., 2018. Introduction to MEMS Packaging. Mems Packaging, 5, p.1.

[16] Donnelly, R.F., Singh, T.R.R. and Woolfson, A.D., 2010. Microneedle-based drug delivery systems: microfabrication, drug delivery, and safety. Drug delivery, 17(4), pp.187-207.

[17] Tanwar, H. and Sachdeva, R., 2016. Transdermal drug delivery system: A review. Int. J. Pharm. Sci. Res, 7, pp.2274-2290.

[18] Mukerjee, E.V., Collins, S.D., Isseroff, R.R. and Smith, R.L., 2004. Microneedle array for transdermal biological fluid extraction and in situ analysis. Sensors and Actuators A: Physical, 114(2-3), pp.267-275.

[19] Schmidt, R.F. and Thews, G. eds., 2013. Physiologie des Menschen. Springer-Verlag.

[20] WIKIMEDIACOMMONS, "Structure of the skin," 2013. [Online].

[21] Delgado-Charro, M.B. and Guy, R.H., 2003. Iontophoresis: applications in drug delivery and noninvasive monitoring.

[22] Prausnitz, M.R. and Langer, R., 2008. Transdermal drug delivery. Nature biotechnology, 26(11), p.1261.

[23] Prausnitz, M.R., Mitragotri, S. and Langer, R., 2004. Current status and future potential of transdermal drug delivery. Nature reviews Drug discovery, 3(2), p.115.

[24] Maghraby, G.M.E., Williams, A.C. and Barry, B.W., 2006. Can drug-bearing liposomes penetrate intact skin?. Journal of Pharmacy and Pharmacology, 58(4), pp.415-429.

[25] Al-Gedadi, N.A. and Hassali, M.A., 2008. Pharmacists' views on generic medicines: A review of the literature. Journal of Generic Medicines, 5(3), pp.209-218.

[26] Bouwstra, J.A., de Graaff, A., Gooris, G.S., Nijsse, J., Wiechers, J.W. and van Aelst, A.C., 2003. Water distribution and related morphology in human stratum corneum at different hydration levels. Journal of Investigative Dermatology, 120(5), pp.750-758.

[27] Sandby-Moller, J., Poulsen, T. and Wulf, H.C., 2003. Epidermal thickness at different body sites: relationship to age, gender, pigmentation, blood content, skin type and smoking habits. Acta Dermato Venereologica, 83(6), pp.410-413.

[28] Mansoor, I., 2014. Fabrication of out-of-plane microneedles for drug delivery and biosensing (Doctoral dissertation, University of British Columbia).

[29] Noyce, R.N., Fairchild Semiconductor Corp, 1961. Semiconductor device-and-lead structure. U.S. Patent 2,981,877.

[30] Li, C.W. and Wang, G.J., 2012. MEMS manufacturing techniques for tissue scaffolding devices. In Mems for Biomedical Applications (pp. 192-217).

[31] Ziaie, B., Baldi, A. and Atashbar, M.Z., 2010. Introduction to micro-/nanofabrication. In Springer handbook of nanotechnology (pp. 231-269). Springer, Berlin, Heidelberg.

[32] https://en.wikipedia.org/wiki/Etching

[33] Wilke, N., Mulcahy, A., Ye, S.R. and Morrissey, A., 2005. Process optimization and characterization of silicon microneedles fabricated by wet etch technology. Microelectronics Journal, 36(7), pp.650-656.

[34] Schwartz, B. and Robbins, H., 1976. Chemical etching of silicon IV. Etching technology. Journal of the electrochemical society, 123(12), pp.1903-1909. Nojiri, K., 2015. Mechanism of Dry Etching. In Dry Etching Technology for Semiconductors (pp. 11-30). Springer, Cham.

[35] Bhandari, R., Negi, S., Rieth, L. and Solzbacher, F., 2010. A wafer-scale etching technique for high aspect ratio implantable MEMS structures. Sensors and Actuators A: Physical, 162(1), pp.130-136.

[36]

[37] Ziaie, B., Baldi, A. and Atashbar, M.Z., 2010. Introduction to micro-/nanofabrication. In Springer handbook of nanotechnology (pp. 231-269). Springer, Berlin, Heidelberg.

[38] Donnelly, V.M. and Kornblit, A., 2013. Plasma etching: Yesterday, today, and tomorrow. Journal of Vacuum Science & Technology A: Vacuum, Surfaces, and Films, 31(5), p.050825.

[39] Laermer, F., 1992. Method for anisotropically etching silicon. German patent DE4241045.

[40] Logeeswaran, V.J., Katzenmeyer, A.M. and Islam, M.S., 2010. Harvesting and transferring vertical pillar arrays of single-crystal semiconductor devices to arbitrary substrates. IEEE Transactions on Electron Devices, 57(8), pp.1856-1864.

[41] Langer, R., 1990. New methods of drug delivery. Science, 249(4976), pp.1527-1533. (38)

[42] R. G. Crystal, "Transfer of genes to humans: early lessons and obstacles to success,"

[43] Science (80-.)., vol. 270, pp. 404–410, 1995.

[44] R. Shahrokh, Z., Sluzky, V., Cleland, J., Shire, S. and E. T., "Therapeutic Protein and

[45] Peptide Formulation and Delivery," merican Chem. Soc. Washington, DC, 1997.

[46] M. R. Prausnitz, "Microneedles for transdermal drug delivery," Adv. Drug Deliv. Rev.,

[47] vol. 56, no. 5, pp. 581–587, 2004.

[48] S. N. Mantha, "Fabrication of PPF Based Drug Containing Microneedle Arrays by

[49] Microstereolithography," pp. 1–134, 2013

[50] Singh, T.R.R., McMillan, H., Mooney, K., Alkilani, A.Z. and Donnelly, R.F., 2017. Fabrication of Microneedles. In Percutaneous Penetration Enhancers Physical Methods in Penetration Enhancement (pp. 305-323). Springer, Berlin, Heidelberg.

[51] Boesveldt, S., Verbaan, D., Knol, D.L., Van Hilten, J.J. and Berendse, H.W., 2008. Odour identification and discrimination in Dutch adults over 45 years. Rhinology, 46(2), p.131.

[52] Kumar, V. and Banga, A.K., 2012. Modulated iontophoretic delivery of small and large molecules through microchannels. International journal of pharmaceutics, 434(1-2), pp.106-114.

[53] Littell, R.C., Henry, P.R. and Ammerman, C.B., 1998. Statistical analysis of repeated measures data using SAS procedures. Journal of animal science, 76(4), pp.1216-1231.

[54] Campbell, P.K., Jones, K.E., Huber, R.J., Horch, K.W. and Normann, R.A., 1991. A silicon-based, three-dimensional neural interface: manufacturing processes for an intracortical electrode array. IEEE Transactions on Biomedical Engineering, 38(8), pp.758-768.

[55] BeMent, S.L., Wise, K.D., Anderson, D.J., Najafi, K. and Drake, K.L., 1986. Solid-state electrodes for multichannel multiplexed intracortical neuronal recording. IEEE transactions on biomedical engineering, (2), pp.230-241.

[56] Chen, J., Wise, K.D., Hetke, J.F. and Bledsoe, S.C., 1997. A multichannel neural probe for selective chemical delivery at the cellular level. IEEE Transactions on Biomedical Engineering, 44(8), pp.760-769.

[57] Griss, P., Enoksson, P., Tolvanen-Laakso, H.K., Merilainen, P., Ollmar, S. and Stemme, G., 2001. Micromachined electrodes for biopotential measurements. Journal of Microelectromechanical Systems, 10(1), pp.10-16.

[58] P. Griss, H. Tolvanen-Laakso, P. Merilainen, and G. Stemme, "Characterization

[59] of micromachined spiked biopotential electrodes," IEEE Trans. Biomed. Eng.,

[60] vol. 49, no. 6, pp. 597–604, 2002

[61] Talbot, N.H., 1998. Polymolding. In Solid-State Sensors and Actuators Workshop Hilton Head Island, South Carolina, June 8-11, 1998.

[62] Mikszta, J.A., Alarcon, J.B., Brittingham, J.M., Sutter, D.E., Pettis, R.J. and Harvey, N.G., 2002. Improved genetic immunization via micromechanical disruption of skin-barrier function and targeted epidermal delivery. Nature medicine, 8(4), p.415.

[63] Chen, H., Shao, M. and Li, Y., 2008. The characteristics of soil water cycle and water balance on steep grassland under natural and simulated rainfall conditions in the Loess Plateau of China. Journal of hydrology, 360(1-4), pp.242-251.

[64] Roguev, A., Bandyopadhyay, S., Zofall, M., Zhang, K., Fischer, T., Collins, S.R., Qu, H., Shales, M., Park, H.O., Hayles, J. and Hoe, K.L., 2008. Conservation and rewiring of functional modules revealed by an epistasis map in fission yeast. science, 322(5900), pp.405-410.

[65] Park, J.H., Widi, G.A., Gimbel, D.A., Harel, N.Y., Lee, D.H. and Strittmatter, S.M., 2006. Subcutaneous Nogo receptor removes brain amyloid-β and improves spatial memory in Alzheimer's transgenic mice. Journal of Neuroscience, 26(51), pp.13279-13286.

[66] Taubman, M.A., Kawai, T. and Han, X., 2007. The new concept of periodontal disease pathogenesis requires new and novel therapeutic strategies. Journal of clinical periodontology, 34(5), pp.367-369.

[67] Park, J.H., Yoon, Y.K., Prausnitz, M.R. and Allen, M.G., 2004. High-aspect-ratio tapered structures using an integrated lens technique. In Micro

Electro Mechanical Systems, 2004. 17th IEEE International Conference on.(MEMS) (pp. 383-386). IEEE.

[68] J. H. Park, Y. K. Yoon, S. O. Choi, M. R. Prausnitz, and M. G. Allen, "Tapered

[69] conical polymer microneedles fabricated using an integrated lens technique for

[70] transdermal drug delivery," IEEE Trans. Biomed. Eng., vol. 54, no. 5, pp. 903–913,

[71] 2007

[72] Griffin, M.J., Abergel, A., Abreu, A., Ade, P.A., André, P., Augueres, J.L., Babbedge, T., Bae, Y., Baillie, T., Baluteau, J.P. and Barlow, M.J., 2010. The Herschel-SPIRE instrument and its in-flight performance. Astronomy & Astrophysics, 518, p.L3.

[73] Park, J.H., Allen, M.G. and Prausnitz, M.R., 2005. Biodegradable polymer microneedles: fabrication, mechanics and transdermal drug delivery. Journal of Controlled Release, 104(1), pp.51-66.

[74] Aller, S.G., Yu, J., Ward, A., Weng, Y., Chittaboina, S., Zhuo, R., Harrell, P.M., Trinh, Y.T., Zhang, Q., Urbatsch, I.L. and Chang, G., 2009. Structure of P-glycoprotein reveals a molecular basis for poly-specific drug binding. Science, 323(5922), pp.1718-1722.

[75] Rubin, A.I., Chen, E.H. and Ratner, D., 2005. Basal-cell carcinoma. New England Journal of Medicine, 353(21), pp.2262-2269.

[76] Verbaan, F.J., Bal, S.M., Van den Berg, D.J., Dijksman, J.A., Van Hecke, M., Verpoorten, H., van den Berg, A., Luttge, R. and Bouwstra, J.A., 2008. Improved piercing of microneedle arrays in dermatomed human skin by an impact insertion method. Journal of controlled release, 128(1), pp.80-88.

[77] Hubbard, T.J., Aken, B.L., Ayling, S., Ballester, B., Beal, K., Bragin, E., Brent, S., Chen, Y., Clapham, P., Clarke, L. and Coates, G., 2008. Ensembl 2009. Nucleic acids research, 37(suppl_1), pp.D690-D697.

[78] Martanto, W., Davis, S.P., Holiday, N.R., Wang, J., Gill, H.S. and Prausnitz, M.R., 2004. Transdermal delivery of insulin using microneedles in vivo. Pharmaceutical research, 21(6), pp.947-952.

[79] Zhu, X., Wang, J., Zhang, X., Chang, Y. and Chen, Y., 2010. Trophic transfer of TiO2 nanoparticles from daphnia to zebrafish in a simplified freshwater food chain. Chemosphere, 79(9), pp.928-933.

[80] McAllister, D.V., Wang, P.M., Davis, S.P., Park, J.H., Canatella, P.J., Allen, M.G. and Prausnitz, M.R., 2003. Microfabricated needles for transdermal delivery of macromolecules and nanoparticles: fabrication methods and transport studies. Proceedings of the National Academy of Sciences, 100(24), pp.13755-13760.

[81] Roxhed, N., Samel, B., Nordquist, L., Griss, P. and Stemme, G., 2008. Painless drug delivery through microneedle-based transdermal patches featuring active infusion. IEEE Transactions on Biomedical Engineering, 55(3), pp.1063-1071.

[82] Gill, H.S. and Prausnitz, M.R., 2007. Coated microneedles for transdermal delivery. Journal of controlled release, 117(2), pp.227-237.

[83] Roxhed, N., 2007. A fully integrated microneedle-based transdermal drug delivery system (Doctoral dissertation, KTH).(47)

[84] A. D. V. McAllsiter, F. Cros, S. P. Davis, L. M. Matta, M. R. Prausnitz and M. G.

[85] Allen, "Three-dimensional hollow microneedles and microtube arrays," in The 10th

[86] Int. Conf. on Solid-state Sensors and Actuators, 1999, pp. 1098–101(48)

[87] Moon, S.J. and Lee, S.S., 2005. A novel fabrication method of a microneedle array using inclined deep x-ray exposure. Journal of Micromechanics and Microengineering, 15(5), p.903.Stoeber, B. and Liepmann, D., 2000. Fluid injection through out-of-plane microneedles. In Microtechnologies in Medicine and Biology, 1st Annual International, Conference On. 2000(pp. 224-228). IEEE.

[88] https://www.ondrugdelivery.com/publications/56/Novinject.pdf

[89] Sivamani, R.K., Stoeber, B., Wu, G.C., Zhai, H., Liepmann, D. and Maibach, H., 2005. Clinical microneedle injection of methyl nicotinate: stratum corneum penetration. Skin Research and Technology, 11(2), pp.152-156.

[90] Griss, P. and Stemme, G., 2003. Side-opened out-of-plane microneedles for microfluidic transdermal liquid transfer. Journal of Microelectromechanical Systems, 12(3), pp.296-301.

[91] Gardeniers, H.J., Luttge, R., Berenschot, E.J., De Boer, M.J., Yeshurun, S.Y., Hefetz, M., van't Oever, R. and van den Berg, A., 2003. Silicon micromachined hollow microneedles for transdermal liquid transport. Journal of Microelectromechanical systems, 12(6), pp.855-862.

[92] McAllister, D.V., Wang, P.M., Davis, S.P., Park, J.H., Canatella, P.J., Allen, M.G. and Prausnitz, M.R., 2003. Microfabricated needles for transdermal delivery of macromolecules and nanoparticles: fabrication methods and transport studies. Proceedings of the National Academy of Sciences, 100(24), pp.13755-13760.

[93] Kim, K., Park, D.S., Lu, H.M., Che, W., Kim, K., Lee, J.B. and Ahn, C.H., 2004. A tapered hollow metallic microneedle array using backside exposure of SU-8. Journal of Micromechanics and Microengineering, 14(4), p.597.

[94] McAllister, D.V., 1999. Three-dimensional hollow microneedle and microtube arrays. In Proc. Transducers' 99 (pp. 1098-1101).

[95] McAllister, D.V., Kaushik, S., Patel, P.N., Mayberry, J.L., Allen, M.G. and Prausnitz, M.R., 1999. Solid and hollow microneedles for transdermal drug delivery. In Proc. Int. Symp. Control. Release Bioact. Mater., 26th, Boston (pp. 192-93).

[96] Davis, S.P., Landis, B.J., Adams, Z.H., Allen, M.G. and Prausnitz, M.R., 2004. Insertion of microneedles into skin: measurement and prediction of insertion force and needle fracture force. Journal of biomechanics, 37(8), pp.1155-1163.

[97] Moon, S.J. and Lee, S.S., 2005. A novel fabrication method of a microneedle array using inclined deep x-ray exposure. Journal of Micromechanics and Microengineering, 15(5), p.903.

[98] Yeshurun, Y., Hefetz, M., Fruchtman, G. and Levin, Y., Nano Pass Tech Ltd, 2009. Devices and methods for transporting fluid across a biological barrier. U.S. Patent 7,588,552.

[99] Perennes, F., Marmiroli, B., Matteucci, M., Tormen, M., Vaccari, L. and Di Fabrizio, E., 2006. Sharp beveled tip hollow microneedle arrays fabricated by LIGA and 3D soft lithography with polyvinyl alcohol. Journal of Micromechanics and Microengineering, 16(3), p.473.

[100] Lhernould, M.S. and Delchambre, A., 2011. Innovative design of hollow polymeric microneedles for transdermal drug delivery. Microsystem technologies, 17(10-11), p.1675.

[101] Wermeling, D.P., Banks, S.L., Hudson, D.A., Gill, H.S., Gupta, J., Prausnitz, M.R. and Stinchcomb, A.L., 2008. Microneedles permit transdermal delivery of a skin-impermeant medication to humans. Proceedings of the National Academy of Sciences, 105(6), pp.2058-2063.

[102] Xia, F. and Jiang, L., 2008. Bio-inspired, smart, multiscale interfacial materials. Advanced materials, 20(15), pp.2842-2858.

[103] Arora, A., Prausnitz, M.R. and Mitragotri, S., 2008. Micro-scale devices for transdermal drug delivery. International journal of pharmaceutics, 364(2), pp.227-236.

[104] Donnelly, R.F., Singh, T.R.R., Morrow, D.I. and Woolfson, A.D., 2012. Microneedle-mediated transdermal and intradermal drug delivery. John Wiley & Sons.

[105] Quinn, H.L., Kearney, M.C., Courtenay, A.J., McCrudden, M.T. and Donnelly, R.F., 2014. The role of microneedles for drug and vaccine delivery. Expert opinion on drug delivery, 11(11), pp.1769-1780.

[106] Ito, Y., Hirono, M., Fukushima, K., Sugioka, N. and Takada, K., 2012. Two-layered dissolving microneedles formulated with intermediate-acting insulin. International journal of pharmaceutics, 436(1-2), pp.387-393.

[107] Liu, S., Jin, M.N., Quan, Y.S., Kamiyama, F., Katsumi, H., Sakane, T. and Yamamoto, A., 2012. The development and characteristics of novel microneedle arrays fabricated from hyaluronic acid, and their application in the transdermal delivery of insulin. Journal of controlled release, 161(3), pp.933-941.

[108] El-Khordagui, L.K., 2012. Microneedles: An Emerging Approach for Active Transdermal Delivery of Insulin. J Bioequiv Availab, 4, pp.0975-0851.

[109] Naito, S., Ito, Y., Kiyohara, T., Kataoka, M., Ochiai, M. and Takada, K., 2012. Antigen-loaded dissolving microneedle array as a novel tool for percutaneous vaccination. Vaccine, 30(6), pp.1191-1197.

[110] Matsuo, K., Yokota, Y., Zhai, Y., Quan, Y.S., Kamiyama, F., Mukai, Y., Okada, N. and Nakagawa, S., 2012. A low-invasive and effective transcutaneous immunization system using a novel dissolving microneedle array for soluble and particulate antigens. Journal of controlled release, 161(1), pp.10-17.

[111]

[112] Garland, M.J., Caffarel–Salvador, E., Migalska, K., Woolfson, A.D. and Donnelly, R.F., 2012. Dissolving polymeric microneedle arrays for electrically assisted transdermal drug delivery. Journal of controlled release, 159(1), pp.52-59.

[113] Donnelly, R.F., Morrow, D.I., McCarron, P.A., Woolfson, A.D., Morrissey, A., Juzenas, P., Juzeniene, A., Iani, V., McCarthy, H.O. and Moan, J., 2008. Microneedle-mediated intradermal delivery of 5-aminolevulinic acid: potential for enhanced topical photodynamic therapy. Journal of Controlled Release, 129(3), pp.154-162.

[114] Matsuo, K., Yokota, Y., Zhai, Y., Quan, Y.S., Kamiyama, F., Mukai, Y., Okada, N. and Nakagawa, S., 2012. A low-invasive and effective transcutaneous immunization system using a novel dissolving microneedle array for soluble and particulate antigens. Journal of controlled release, 161(1), pp.10-17.

[115] Lee, K. and Lee, S.E., 2007. Saccharomyces cerevisiae Sae2-and Tel1-dependent single strand DNA formation at DNA break promotes microhomology-mediated end joining. Genetics.

[116] WIKIPEDIA, "Deep reactive-ion etching," 2018. [Online]. Available:

[117] https://en.wikipedia.org/wiki/Deep_reactive-ion_etching.

[118] Chekurov, N., Grigoras, K., Peltonen, A., Franssila, S. and Tittonen, I., 2009. The fabrication of silicon nanostructures by local gallium implantation and cryogenic deep reactive ion etching. Nanotechnology, 20(6), p.065307.

[119] Chekurov, N., Grigoras, K., Sainiemi, L., Peltonen, A., Tittonen, I. and Franssila, S., 2010. Dry fabrication of microdevices by the combination of focused ion beam and cryogenic deep reactive ion etching. Journal of Micromechanics and Microengineering, 20(8), p.085009.

[120] Parasuraman, J., Summanwar, A., Marty, F., Basset, P., Angelescu, D.E. and Bourouina, T., 2014. Deep reactive ion etching of sub-micrometer trenches with ultra high aspect ratio. Microelectronic engineering, 113, pp.35-39.

[121] Lai, S.L., Johnson, D. and Westerman, R., 2006. Aspect ratio dependent etching lag reduction in deep silicon etch processes. Journal of Vacuum Science & Technology A: Vacuum, Surfaces, and Films, 24(4), pp.1283-1288.

[122] Abdolvand, R. and Ayazi, F., 2008. An advanced reactive ion etching process for very high aspect-ratio sub-micron wide trenches in silicon. Sensors and Actuators A: Physical, 144(1), pp.109-116.

[123] Tang, Y., Sandoughsaz, A., Owen, K.J. and Najafi, K., 2018. Ultra Deep Reactive Ion Etching of High Aspect-Ratio and Thick Silicon Using a Ramped-Parameter Process. Journal of Microelectromechanical Systems, 27(4), pp.686-697.

[124] Feng, J., Fohlerová, Z., Liu, X., Chang, H. and Neužil, P., 2018. Microfluidic device based on deep reactive ion etching process and its lag effect for single cell capture and extraction. Sensors and Actuators B: Chemical, 269, pp.288-292.